# ABSORPTION AND MAGNETIC CIRCULAR DICHROISM OF TRANSITION METAL ATOMS AND SMALL CLUSTERS ISOLATED IN NOBLE GAS MATRICES

BY

JALAL SHAKHSEMAMPOUR

A DISSERTATION PRESENTED TO THE GRADUATE COUNCIL
OF THE UNIVERSITY OF FLORIDA IN PARTIAL
FULFILLMENT OF THE REQUIREMENTS FOR THE
DEGREE OF DOCTOR OF PHILOSOPHY

UNIVERSITY OF FLORIDA

1983

To my parents

and

my daughters, Rahelah and Rabeah

# ACKNOWLEDGEMENTS

I would like to express my deep appreciation, gratitude and indebtedness to my research director, Professor Martin Vala, for his encouragement, guidance, kindness, and friendship.

I would also like to thank Dr. Jean-Claude Rivoal for stimulating discussions, design and construction of the electronics. Thanks are also due to Dr. Robert Pyzalski, Dr. Joseph Baiardo, and Dr. Marek Kreglewski for many helpful and informative discussions. For assistance in running the CD spectrum of the standard solution the author thanks Mr. Marc Eyring.

The understanding, assistance, and patience of my daughters, Rahelah and Rabeah, are deeply appreciated.

The skillful typing of this dissertation by Ms. Candy Caputo is greatly appreciated.

Funding for this project has been provided by the National Science Foundation and the Graduate School.

# TABLE OF CONTENTS

Page

ACKNOWLEDGEMENTS . . . . . . . . . . . . . . . . . . . . iii

LIST OF TABLES . . . . . . . . . . . . . . . . . . . . . vi

LIST OF FIGURES . . . . . . . . . . . . . . . . . . . . vii

ABSTRACT . . . . . . . . . . . . . . . . . . . . . . . . x

CHAPTER I INTRODUCTION . . . . . . . . . . . . . . . . 1

CHAPTER II THEORY OF MAGNETIC CIRCULAR DICHROISM . .

- Basic Equations . . . . . . . . . . . . . . . . . . 11
- Selection Rules for MCD . . . . . . . . . . . . . . 28
- Spectral Moment Analysis . . . . . . . . . . . . . 32

CHAPTER III APPARATUS . . . . . . . . . . . . . . . . . 35

- Matrix Isolation Apparatus . . . . . . . . . . . . 35
- Spectroscopic Apparatus . . . . . . . . . . . . . . 48

CHAPTER IV EXPERIMENTAL TECHNIQUES . . . . . . . . . . 63

CHAPTER V IRON IN THE RARE GAS MATRICES . . . . . . . 71

- Computational Results and Spectral Predictions . . 74
- Band Moment Analysis . . . . . . . . . . . . . . . 77
- Experimental Procedure . . . . . . . . . . . . . . 89
- Results and Discussion . . . . . . . . . . . . . . 89
- Fe/Kr . . . . . . . . . . . . . . . . . . . . . . . 98
- Fe/Ar . . . . . . . . . . . . . . . . . . . . . . . 102
- $Fe_x$ Cluster Bands . . . . . . . . . . . . . . . . 108

CHAPTER VI MANGANESE IN THE RARE GAS MATRICES . . . 112

- Experimental Procedure . . . . . . . . . . . . . . 114
- Results and Discussion . . . . . . . . . . . . . . 115
- Mn/Kr . . . . . . . . . . . . . . . . . . . . . . . 116
- Spectral Moment Analysis . . . . . . . . . . . . . 126
- Mn/Xe . . . . . . . . . . . . . . . . . . . . . . . 132
- Mn/Ar . . . . . . . . . . . . . . . . . . . . . . . 140
- $Mn_2$ . . . . . . . . . . . . . . . . . . . . . . . . 147

Page

CHAPTER VII CHROMIUM IN THE RARE GAS MATRICES . . . . 163

Experimental Procedure . . . . . . . . . . . . . . . . 165
Results and Discussion . . . . . . . . . . . . . . . . 166
Cr/Kr . . . . . . . . . . . . . . . . . . . . . . . . 166
Cr/Xe . . . . . . . . . . . . . . . . . . . . . . . . 178
Spectral Moment Analysis . . . . . . . . . . . . . . 182
Cr/Ar . . . . . . . . . . . . . . . . . . . . . . . . 186

CHAPTER VIII CONCLUDING REMARKS . . . . . . . . . . . . 194

REFERENCES . . . . . . . . . . . . . . . . . . . . . . . 197

BIOGRAPHICAL SKETCH . . . . . . . . . . . . . . . . . . 203

## LIST OF TABLES

Table Page

1 Calculated MCD Parameters for Free Atomic Iron Transitions From J=4 State to J' States . . . . . 75

2 Relative Dipole Strengths for Atomic Iron Transitions From $^5D_4$ State to $^5\Gamma^{o\prime}_J$ Excited State 78

3 MCD Band Positions and Assignments for Fe Atoms Isolated in a Krypton Matrix . . . . . . . . . . 94

4 MCD Band Positions and Assignments for Fe Atoms Isolated in an Argon Matrix . . . . . . . . . . . 95

5 MCD Band Positions and Assignments for Fe Atoms Isolated in a Xenon Matrix . . . . . . . . . . . 97

6 MCD Band Positions, Matrix Shifts and Assignments for Mn Species Isolated in a Krypton Matrix . . . 119

7 MCD Band Positions, Matrix Shifts and Assignments for Mn Species Isolated in a Xenon Matrix . . . . 137

8 MCD Band Positions, Matrix Shifts and Assignments for Mn Species Isolated in an Argon Matrix . . . 143

9 MCD Band Positions, Matrix Shifts and Assignments for Chromium Species Isolated in a Krypton Matrix 171

10 MCD Band Positions, Matrix Shifts and Assignments for Chromium Species Isolated in a Xenon Matrix . 181

11 MCD Band Positions, Matrix Shifts and Assignments for Chromium Species Isolated in an Argon Matrix 191

## LIST OF FIGURES

Figure Page

1 The appearance of the experimental form of the $A_1$, $B_o$ and $C_o$ terms predicted by MCD theory . . . 24

2 Magnetic field splittings of ground and excited states illustrating the origin of $A_1$ and $C_o$ terms 27

3 Magnetic field splittings and polarized transitions to an atomic P state . . . . . . . . . . . 31

4 A diagram of the vacuum system . . . . . . . . . 38

5 Diagrams of the furnace assembly and Knudsen cell
(a) Diagram of the furance assembly . . . . . . 40
(b) Diagram of Knudsen cell used for metal vaporization . . . . . . . . . . . . . . . . 40

6 Diagram of the furnace-cryostat assembly used in matrix isolation experiments . . . . . . . . . 45

7 A diagram of the rare gas inlet system . . . . . 47

8 Optics for absorption experiments . . . . . . . . 50

9 Electronics for absorption experiments . . . . . 54

10 Optics for MCD experiments . . . . . . . . . . . 58

11 Electronics for MCD experiments . . . . . . . . . 60

12 Plot of MCD intensity vs. magnetic field strength 68

13 Absorption (top) and MCD (bottom) spectra of iron atoms in a krypton matrix at 14 K . . . . . . . 81

14 Temperature dependence of the Fe atom $C_o$ term in a krypton matrix . . . . . . . . . . . . . . . 83

15 Experimental plot of $\langle\Delta A\rangle_o/\langle A\rangle_o$ vs. reciprocal temperature for krypton matrix-isolated Fe atom band at ~355 nm . . . . . . . . . . . . . . . . 85

16 Experimental plot of $\langle\Delta A\rangle_o/\langle A\rangle_o$ vs. reciprocal temperature for krypton matrix-isolated Fe atom band at ~359 nm . . . . . . . . . . . . . . . . 88

Page

17 Absorption (top) and MCD (bottom) spectra of iron atoms in an argon matrix at 14 K . . . . . . . . 91

18 MCD spectrum of iron atoms in a xenon matrix at 18 K . . . . . . . . . . . . . . . . . . . . . 93

19 Absorption (top) and MCD (bottom) spectra of iron atoms in a krypton matrix at 14 K . . . . . . . 100

20 Temperature dependence of the Fe atom $C_o$ term in an argon matrix . . . . . . . . . . . . . . . . 105

21 Superposition of a small portion of the MCD spectra of Fe/Ar and Fe/Kr . . . . . . . . . . 107

22 MCD Spectra showing Fe atomic lines and $Fe_x$ cluster bands in an argon matrix . . . . . . . . 110

23 Absorption (top) and MCD (bottom) spectra of manganese species in a krypton matrix at 14 K . 118

24 Temperature dependence of the Mn atom bands (~387 nm) in a krypton matrix . . . . . . . . . 123

25 Temperature dependence of the Mn atom bands (~284 nm) in a krypton matrix . . . . . . . . . 125

26 Experimental plot of $\langle\Delta A\rangle_1/\langle A\rangle_o$ vs. reciprocal temperature for krypton matrix-isolated Mn atom bands at ~387 nm . . . . . . . . . . . . . 128

27 Experimental plot of $\langle\Delta A\rangle_3/\langle A\rangle_o$ vs. reciprocal temperature for krypton matrix-isolated Mn atom bands at ~387 nm . . . . . . . . . . . . . 131

28 Absorption spectrum of Mn species in a xenon matrix at 14 K . . . . . . . . . . . . . . . . . 134

29 MCD spectrum of Mn species in a xenon matrix at 14 K . . . . . . . . . . . . . . . . . . . . . 136

30 MCD temperature dependence of Mn species in a xenon matrix . . . . . . . . . . . . . . . . . . 139

31 Absorption (top) and MCD (bottom) spectra of manganese species in an argon matrix . . . . . 142

32 MCD temperature dependence of manganese species in an argon matrix at 13 K and 20 K . . . . . . 146

Page

33 Selected part of the absorption spectrum (bottom) and MCD spectrum (top) of Mn matrix-isolated in Ar . . . . . . . . . . . . . . . . . . . . . 151

34 Enlarged spectrum of transitions e and f of Figure 33 at three selected temperatures . . . . . . 155

35 Typical level scheme of the ground-state $Mn_2$ molecule in the case of isotropic exchange with and without external applied field . . . . 158

36 Semi-log plot of the zeroth-order moment of band e versus reciprocal temperature . . . . . 160

37 Absorption (top) and MCD (bottom) spectra of chromium species in a krypton matrix . . . . . 168

38 MCD temperature dependence of the chromium species in a krypton matrix . . . . . . . . . 170

39 Absorption spectrum of chromium in a krypton matrix . . . . . . . . . . . . . . . . . . . 173

40 Temperature dependence of the chromium atom $C_o$ term in a krypton matrix . . . . . . . . . . . 177

41 Absorption (top) and MCD (bottom) spectra of chromium species in a xenon matrix . . . . . . 180

42 Experimental plot of $<\Delta A>_1/<A>_o$ vs. $\frac{1}{T}$ for xenon matrix-isolated chromium atom band at 410 nm . 185

43 Experimental plot of $<\Delta A>_3/<A>_o$ vs. $\frac{1}{T}$ for xenon matrix-isolated chromium atom band at 410 nm . 188

44 Absorption (top) and MCD (bottom) spectra of chromium species in an argon matrix . . . . . 190

Abstract of Dissertation Presented to the Graduate Council
of the University of Florida in Partial Fulfillment of the
Requirements for the Degree of Doctor of Philosophy

# ABSORPTION AND MAGNETIC CIRCULAR DICHROISM OF TRANSITION METAL ATOMS AND SMALL CLUSTERS ISOLATED IN NOBLE GAS MATRICES

By

Jalal Shakhsemampour

December, 1983

Chairman: Martin Vala
Major Department: Chemistry

Iron, manganese and chromium atoms and small clusters have been isolated in argon, krypton and xenon matrices and studied by absorption and magnetic circular dichroism (MCD) spectroscopy.

A detailed analysis of the absorption and MCD results obtained for Fe, Mn, and Cr and their small clusters as well as a moment analysis for the bands originating from the $^5P_3 \leftarrow {}^5D_4$ and $^5F_5 \leftarrow {}^5D_4$ transitions for Fe/Kr, $z^6P \leftarrow {}^6S$ transition of Mn/Kr, and $z^7P \leftarrow {}^7S$ transition of Cr/Xe are presented.

For the case of matrix-isolated iron atoms, the influence of the matrix is shown to be minimal. Neither matrix-induced site splittings nor vibronic-mixing (Jahn-Teller) effects are observed. A moment analysis of the atomic iron band located at 333.5 nm with a positively-signec $C_0$ term has been carried out to extract the experimental value of the

$C_0/D_0$ term. The value obtained is 8.2 ± 0.8 which is in good agreement with the theoretical value of 7.5. Two major sites are found for iron in argon whereas only one is present in krypton and xenon matrices. From the observed MCD $C_0$ terms, it is concluded that the ground electronic state of the $Fe_x$ cluster species is both orbitally and spin degenerate.

For the case of matrix-isolated manganese species, the MCD signals corresponding to the atomic $z^6P \leftarrow {}^6S$ transition are intense, show a strong temperature dependence, and exhibit a triplet of bands with separation much larger than the spin-orbit splittings of the $z^6P$ excited state. A band moment analysis indicates that the Jahn-Teller effect is active in this system. The cubic and noncubic contributions to the bandwidth from the lattice modes are $1.2 \times 10^5$ $cm^{-2}$ and $3.6 \times 10^4$ $cm^{-2}$, respectively, in Mn/Kr. The Mn/Ar matrix bands at 347 nm and 331.5 nm are due to the $Mn_2$ antiferromagnetic molecule with a ground-state exchange energy of $-10.3 \pm 0.6$ $cm^{-1}$.

For the case of matrix-isolated chromium species, three major sites are found for $Cr_2$ in krypton whereas only one is present in argon and xenon matrices. A moment analysis of the lower triplet bands of the chromium atom in a xenon matrix indicates clearly that the Jahn-Teller effect is active in the $z^7P$ excited state. From plotted moments, the contribution of the cubic and noncubic lattice modes to the bandwidth is $8.6 \times 10^3$ $cm^{-2}$ and $7.7 \times 10^4$ $cm^{-2}$, respectively. The spin-orbit splitting in the xenon matrix compared to the gas phase is reduced by a factor of 3.2.

# CHAPTER I

# INTRODUCTION

Matrix isolation spectroscopy is now widely employed to investigate electronic and vibronic properties of reactive species such as high temperature atoms, molecules, and radical fragments. A significant body of literature has evolved recently on the spectroscopy and chemistry of metal atoms, dimers, and higher aggregates in low temperature matrices.[1-4] There are a number of reasons for this increasing attention. First, to comprehend the processes of heterogeneous catalysis,[5] nucleation,[6] chemisorption,[7] and photography,[8] one must have a knowledge of the electronic structures of metal dimers and clusters. Second, it has recently been shown that optically pumped dimers, including some metals, lase in both CW and pulsed modes.[9,10] And, finally, by codepositing a metal vapor, which was prepared in a high temperature furnace, with a reactive partner on a cryogenic surface, new chemical compounds have been synthesized.[1,4]

Matrix isolation is the technique whereby one can trap a reactive chemical species (guest) by codepositing it at cryogenic temperatures with large quantities of an inert substance (matrix or host) such as a noble gas. To do matrix isolation, two major things must be done. First, a cold surface must be created and its temperature must be measured.

Second, the chemical species of interest must be produced and deposited onto a cold surface.

The technique of matrix isolation was first introduced in 1941 by Lewis et al.[11] who studied the phosphorescence of low concentrations of various aromatic molecules which were suspended in a rigid, glassy environment at low temperatures. Norman and Porter[12] and Whittle et al.[13] independently proposed the technique of matrix isolation spectroscopy in 1954 as a means of studying stabilized free radicals which were photogenerated from the isolated molecules in argon and nitrogen matrices. In 1961, Linevsky[14] applied the technique of matrix isolation to the study of high temperature molecules and observed the infrared spectra of monomeric LiF in argon, krypton xenon and nitrogen matrices. Since that time a large number of high temperature molecules have been isolated. An excellent review of the matrix isolation of high temperature molecules was published in 1978 by Weltner.[15] The book Low Temperature Spectroscopy by Meyer[16] includes a detailed introduction to the method of matrix isolation.

It is usually assumed in such studies that the matrix host is both rigid enough to prevent the isolated guest species from diffusing and reacting, and also sufficiently chemically inert to minimize its influence on the physical and chemical properties of the guest species. However, recent experimental studies, especially with isolated metal atoms have shown that localized matrix host atoms interact with isolated guest species and markedly influence the electronic and vibronic properties of the embedded species. The matrix influence manifests itself by shifts in the energies of spectra, line broadening, and additional level splitting.[17,18]

The guest environment depends upon preparation conditions, but it seems that it is almost always oriented in a random fashion. The guest species can be trapped in different microenvironments (multiple sites) in the crystalline lattice which manifests itself by band broadening and multiplets due to differing energies of the various sites. These site effects can often be detected by warming the matrix to allow controlled diffusion and thus allow the guest species to settle in the more stable sites resulting in more simplified spectra. Lattice vibrational modes and Jahn-Teller distortions due to host-guest interactions have also been observed.[19,20]

Matrix-isolated samples are prepared by vapor codeposition of a large amount of the host gas and a small amount of the vapor of the guest gaseous species on a low temperature window. The host-guest ratios of $10^3$:1 to $10^5$:1 are commonly employed to minimize the guest-guest interactions. The apparatus system must be pumped to a pressure of less than $10^{-5}$ torr by a suitable diffusion pump. The sample thickness depends upon the oscillator strength of the optical transition that is to be observed. For example, micromolar quantities of guest species are enough for allowed electronic transitions, whereas for forbidden visible or infrared (IR), transitions millimolar quantities or more are usually necessary.

Metal atoms are most easily generated by directly heating a filament, ribbon, or rod of the metal. For this purpose, a low-voltage and high-current transformer is usually employed.

Several metals such as chromium and manganese cannot be deposited in this manner. These metals can be generated from a Knudsen cell which is a small chamber constructed from a refractory metal such as Ta, Mo or W with a small orifice in it to allow outflow of the enclosed substance in a crude molecular beam.

The typical matrix materials are the rare gases, $N_2$, $H_2$, $SF_6$, and lighter hydrocarbons (i.e., $CH_4$). More reactive materials such as CO, $CO_2$, and $O_2$ are also used as a host gas. The solid rare gases Ne, Ar, Kr, and Xe are more often used in matrix isolation spectroscopy. These solids are relatively chemically inert and optically transparent from the far infrared up to vacuum ultraviolet. In the present research Ar, Kr, and Xe have been used as a matrix gas. Neon matrices were not available since our apparatus could not attain the low temperatures required (i.e., below 10 K).

The sample window (the substrate on which the matrix is formed) must be transparent in this spectral range of interest and a good thermal conductor to allow rapid thermal quenching of the host and guest species. The matrix substrates which are commonly used are NaCl, KBr, CsI, and CsBr for the infrared region; sapphire (UV grade), LiF, and $MgF_2$ for the ultraviolet and infrared regions; $CaF_2$ and quartz for the visible and ultraviolet regions. A polished aluminum surface is usually used for matrix Raman work and a high purity sapphire rod for matrix electron spin resonance.

To achieve low temperatures, the sample window must be in contact thermally with either a mechanical closed-cycle refrigerator (which operates by Joule-Thomson expansion of helium gas) or by a physical refrigerant such as liquified helium, hydrogen or nitrogen which maintains the cryogenic window at 4.2 °K, 20.4 °K, and 77.4 °K respectively. Temperature measurements of the sample window can be done by a temperature controller. This instrument uses a diode sensor to provide it with an input which generates heater current and is proportional to the difference between the desired temperature and the measured temperature of the cryogenic sample window. To prevent the diffusion of the cold host, the temperature of the cold window is chosen below forty percent of the matrix melting point.

The matrix isolation technique has been employed successfully to carry out a variety of spectroscopic experiments.[16] The spectroscopic techniques which have been applied to matrix-isolated samples include visible and ultraviolet absorption and emission, IR, Raman, Mössbauer, nuclear magnetic resonance (NMR), and electron spin reaonance (ESR), and more recently magnetic circular dichroism (MCD). The technique of MCD has recently generated increasing interest among molecular spectroscopists since the theoretical development introduced by Buckingham and Stephens[21] in 1966. In 1973, Douglas, Grinter, and Thomson[22] applied the MCD technique to the matrix-isolated samples and they demonstrated that the two techniques could be combined and that matrix-isolated species could be studied employing magnetic circular dichroism spectroscopy.

Linearly polarized light can be considered to consist of equal magnitudes of right circularly polarized (RCP) and left circularly polarized (LCP) components. In materials that are not optically active the absorption of left and right circularly polarized (CP) light is identical. If LCP and RCP are unequal in the indices of refraction, optical rotation occurs. If the absorptoin coefficients for an electronic transition differ for LCP and RCP light, circular dichroism (CD) is created for this transition. The inequality in the indices of refraction may be proved by two different methods.

First, natural optical activity which arises in molecules or in the unit cell of crystals as a result of low symmetry and its wavelength dependence is called optical rotatory dispersion (ORD). Second, in the presence of a longitudinal magnetic field, $\vec{H}$, the optical properties of materials need no longer be symmetrical with respect to left and right circular polarization. In this case the right- and left-handed circular motions about an external magnetic field do not have equivalent interactions with the medium, resulting in different magnitude of absorption coefficients in the absorption regions for RCP and LCP light. This is the phenomenon of magnetic circular dichroism (MCD). Therefore, MCD can be defined as the difference in absorption of LCP and RCP light by a sample subjected to a magnetic field parallel to the propagation direction of the light.

Magnetic circular dichroism can provide valuable information on both the ground and excited states of atoms and molecules. The prime utilization of MCD has been in extracting excited state information, such as excited state magnetic moments, g values, spin-orbit coupling, and Jahn-Teller interactions.[23] Recently Mowery et al.[20] have observed Jahn-Teller interactions in the MCD of matrix-isolated magnesium atoms. Zeringue et al.[19] have studied the $^2P \leftarrow {}^2S$ transition of copper atoms isolated in argon matrices and observed that simultaneous spin-orbit and noncubic lattice vibrational couplings (Jahn-Teller effect) are active in the Cu excited $^2P$ state. These authors also observed a reduction of 25% in the excited state spin-orbit coupling constant which is attributed to the overlap of Cu 4p orbitals with the Ar 3p orbitals.

On a microscopic level, MCD is closely related to the Zeeman effect (i.e., perturbation of the absorbing system by the applied magnetic field) and provides similar types of information as classical Zeeman spectroscopy. However, the resolution of Zeeman components is often difficult, requiring a very high magnetic field. The advantage of MCD is that it can be measured in broad absorption bands where Zeeman splitting cannot be resolved. Another advantage of MCD is that it is a signed technique and does not require high magnetic fields. As an example, a 5500 Gauss magnetic field was employed in the present research. The electronic transitions may sometimes be resolved in MCD and not in absorption. A transition which overlaps a stronger transition can be resolved if the transitions have different MCD signs (i.e., positive and negative bands) or if the MCD is much larger for one of the overlapping components. For example, despite the fact that the absorption bands of tryptophan and tyrosine overlap, they can be distinguished from each other.[24,25] Sometimes an electronic transition can be observed in MCD even though the absorption band for the same transition is too weak to be observed. Typical values for the minimum detectability of absorbance and MCD are $10^{-3}$ OD and $10^{-5}$ΔOD respectively. This situation has been observed in spin-forbidden transitions of octahedral and tetrahedral Co (II) species.[26,27]

Early MCD studies were concentrated on room temperature solutions and on species in single crystals.[21.28,29] Low temperature experiments on polymer films, glasses and uniaxial crystals have since demonstrated that temperature dependence studies of MCD for a species with a degenerate ground state can provide valuable additional information.

The optical spectra of matrix-isolated samples which are studied by absorption and MCD spectroscopy are greatly simplified because rotational motions are quenched and thermal population of low lying levels above the ground state is eliminated. As a result of these eliminations, absorption in the matrix-isolated molecular species occurs only from the lowest vibrational level of the ground electronic state.

Matrix-isolated samples studied by MCD to date have included atomic species Hg,[30] Mg,[20], Ta,[31] Pb;[32] group Ib atoms (Cu, Ag, Au);[33] diatomic $Cl_2$,[34], $O_2$,[35] xenon halides;[36] diatomic oxides of group IVb (Ti, Zr, Hf),[37] and Vb (V, Nb, Ta);[38] $OsO_4$,[39] benzene,[40] and acrolein.[41]

The study reported here involves matrix-isolated samples of atoms and/or clusters of Cr, Mn, and Fe. Primary reasons for studying these systems are the important roles of the small clusters in the processes of heterogeneous catalysis,[5] nucleation,[6] chemisorption,[7] and photography.[8] The study of electronic spectra of these systems can play an important role in the development of optically pumped lasers which lase in both CW and pulsed modes.

The principal goal is the assignment of the observed bands and a determination of the gas-to-matrix spectral shift(s). In the assignment of the spectral bands, it is assumed that the intensity pattern of the gas phase spectra is transferable to the matrix spectra. So, the intense bands in the gas phase spectra are expected to display strong matrix bands. It is also assumed that the gas-to-matrix band shifts are similar for transitions to the same energy term. The correlation method, which has been applied to matrix assignments of excited electronic states of the atoms or molecules, relies on the signs of MCD bands for allowed transitions.

The remainder of this thesis will cover the theory of MCD, the details of absorption and MCD apparatus, the experimental procedure employed in this research, and a detailed description of the experimental results for Cr, Mn,[42] and Fe[43] atoms and/or clusters. A moment analysis of the MCD spectra for Fe and Mn, atoms in krypton matrices and Cr atoms in a xenon matrix is also included (vide infra).

# CHAPTER II

## THEORY OF MAGNETIC CIRCULAR DICHROISM

An introduction to the theory of magnetic circular dichroism (MCD) as well as its pertinent equations will be presented in this chapter. The theoretical treatment by Stephens[21,44,45,46] has received wide acceptance and will be used in this study.

The electromagnetic nature of light was proposed by Maxwell in the 1860's and confirmed by the experiments of Heinrich Hertz in 1887 and 1888. As the term electromagnetic radiation implies, both an electric field and magnetic field are associated with all light waves. These fields are at right angles to each other and vary sinusoidally with the propagation direction of light. In unpolarized light both the electric field vector, $\vec{E}$, and the magnetic field vector, $\vec{H}$, are random in direction whereas in plane polarized light they are constant in direction but vary in magnitude. In a transparent birefringent medium, the speed of light depends upon the direction of polarization of the light.

If the plane polarized beam is passed through this medium, part of the beam will be delayed with respect to the other. The difference in refractive indices and the thickness of the medium are factors that influence the magnitude of this delay. If the plane polarized beam enters the birefringent medium oriented at 45° relative to two perpendicular axes of different refractive index, compounds of the projection of the $\vec{E}$ and $\vec{H}$ vectors of equal magnitude will be phase shifted relative to each other. If this phase shift is equal to the wavelength, λ, the emergent beam will remain plane polarized. If, however, the phase shift is not equal to λ, the resultant electromagnetic vectors $\vec{E}$ and $\vec{H}$ will trace helical paths upon emergence. If the helix is traced clockwise to an observer looking toward the light source, the beam is called right polarized and vice versa for left polarized. If the phase shift is equal to λ/4 or an integral multiple of λ/4, the cross section of the helix will be a circle and the light is said to be circularly polarized (CP). If, however, the phase shift differs from an integral multiple of λ/4, the cross section of the helix will be an ellipse and the light is said to be elliptically polarized (EP). The electromagnetic vectors $\vec{E}$ and $\vec{H}$ in CP light are constant in magnitude but vary in direction, while in EP light they vary both in magnitude and direction.

If in a medium right and left CP are propagated with unequal amount of absorbance, the medium will exhibit circular dichroism (CD). Natural CD is a relatively rare phenomenon, whereas magnetic circular dichroism (MCD) is a property of all matter. MCD is the differential absorbance of left and right CP light by a sample subjected to a magnetic field parallel to the propagation direction of the incident CP light.

## Basic Equations

For circularly polarized light of energy $\varepsilon_0$ travelling in the positive Z direction of a Cartesian coordinate system, the solution of Maxwell's equations yield for the electric field vector

$$E_{\pm}\ (Z,t) = \overset{\circ}{E}_{o} \exp\left[\frac{i\varepsilon(t-\hat{n}_{\pm}z/c)}{\hbar}\right](\vec{i} \pm i\vec{j}) \tag{1}$$

and for the magnetic field vector

$$H_{1}\ (Z,t) = (n_{\pm}/\mu)\ \overset{\circ}{E}_{o} \exp\left[\frac{i\varepsilon(t-\hat{n}_{\pm}z/c)}{\hbar}\right](\mp i\vec{i} + \vec{j}) \tag{2}$$

where + and - refer to right and left CP light respectively, $\varepsilon = h\nu$ is the photon energy, $\overset{\circ}{E}_{o}$ is the electric field at Z=0, $i = \sqrt{-1}$, t is the time, c is the speed of light, $\hat{\mu}$ is the complex magnetic permeability in the xy-plane, and $\hbar$ is Planck's constant divided by $2\pi$. Note that the medium is isotropic in the xy-plane. The vectors $\vec{i}$ and $\vec{j}$ are the unit vectors in the x and y directions, respectively. The complex refractive index is represented by $\hat{n}_{\pm}$ and equals $n_{\pm} - ik_{\pm}$ where $n_{\pm}$ is the real part of the refractive index and $k_{\pm}$ is the absorption coefficient for right (+) and left (-) CP light. $n_{\pm}$ is a function of the external magnetic field via the effect of the field upon $k_{\pm}$. The MCD spectrum of a sample is directly related to the difference in absorption coefficient $k_{\pm}$, but is usually measured as differential absorbance of right and left CP light ($A_{\pm}$).

Consider a light beam passing through a sample with ground state A and excited states J and K in the presence of an external magnetic field, $\vec{H}$, parallel to the propagation direction of the light. The intensity of the light I(Z), at a point Z (the energy passing through a unit area in unit time), is given by the time average of the Poynting vector $(c/4\pi)(\vec{E}\times\vec{H})$.

$$I_\circ \, (Z) = (\frac{c}{4\pi})(\hat{n}_\pm / \hat{\mu}) \, E_\circ^{\circ 2} \, \exp \, (\frac{-2\varepsilon k_\pm Z}{\hbar c}) \qquad (3)$$

making the approximation that $\hat{\mu} = 1$, yields

$$I_\pm \, (Z) = (\frac{c}{4\pi}) \, n_\pm \, E_\circ^{\circ 2} \, \exp \, (\frac{-2\varepsilon k_\pm Z}{\hbar c})$$

$$= I_\pm(o) \, \exp \, (\frac{-2\varepsilon k_\pm Z}{\hbar c}) \qquad (4)$$

where $I_\circ$ (o) is the intensity of the incident light. Setting $\hat{\mu} = 1$ excludes magnetic materials from consideration. Solving for $k_\pm$ by differentiation yields

$$k_\pm = [\frac{h}{n_\pm \varepsilon |E_\pm(Z)|^2}][- \frac{\delta I_\pm(Z)}{\delta Z}] \qquad (5)$$

where $|E_\pm(Z)|^2$ is the magnitude of the electric field at Z

$$E_\pm(Z)^2 = E_\circ^{\circ 2} \, \exp \, (\frac{-2\varepsilon k_\pm Z}{\hbar c}) \qquad (6)$$

The quantity $[- \frac{\delta I_\pm(Z)}{\delta Z}]$ is the energy absorbed per unit time per unit volume at Z and can be related to the probability of the transition $P_{a\rightarrow j}$,

$$- \frac{\delta I}{\delta Z}(Z) = {}_{a,j}\Sigma \, N_a \, P_{a \;\, j} \, (Z)\varepsilon \qquad (7)$$

where ε is the photon energy, $N_a$ is the number of absorption centers of state a per unit volume.

If we limit our treatment to the electric dipole transitions and ignore electric quadrupole and magnetic dipole interactions, we can relate the probability of absorption ($P_{a\rightarrow j}$) to the electric dipole transition matrix elements via time-dependent perturbation theory. The effective Hamiltonian, $H_\circ$, is assumed to be a sum of independent components (i.e., the Hamiltonian of the center plus radiation),

$$H_o = \overset{o}{H}_o + H_o' \qquad (8)$$

where $\overset{o}{H}_o$ is the unperturbed Hamiltonian for the system in the absence of light and $H_o'$ is the perturbed Hamiltonian due to the interaction with the radiation field. The superscript zero indicates the absence of the radiation field and the subscript zero indicates the absence of an external magnetic field. The resulting equation for the probability of the transition $P_{a \to j}$ is

$$P_{a \to j}\ (Z) - \frac{\alpha^2 \pi}{\hbar}\ |E_\pm(Z)|^2\ |\langle a|m_\pm|j\rangle|^2\ \delta\ (\varepsilon_{ja} - \varepsilon) \qquad (9)$$

where $|a\rangle$ and $|j\rangle$ are the eigenstates of $\overset{o}{H}_o$ of energy $\varepsilon_a$ and $\varepsilon_j$, respectively, and $\varepsilon_{ja} = \varepsilon_j - \varepsilon_a$. $\alpha$ is the Lorentz effective field correction factor which relates the electric field due to the light wave at the center of absorption to the macroscopic E field, and $m_\pm$ is the transition dipole moment operator for right CP and left CP transitions and equals $(1/\sqrt{2})\ (m_x \pm im_y)$. $\delta$ is the Kronecker delta operator and arises from the neglect of transition lifetimes.

The equation for the absorption coefficients, $k_\pm$, can now be expressed as

$$k_\pm = \frac{2\pi^2\alpha^2}{n_\pm}\ \sum_{a,j} N_a\,|\langle a|m_\pm|j\rangle|^2\ \delta\,(\varepsilon_{ja} - \varepsilon) \qquad (10)$$

By transforming the equation (10) into more practical spectroscopic notation (i.e., in terms of absorbance) we can them write

$$\frac{I(Z)}{I(o)} = \exp\ \left(\frac{-2\varepsilon kZ}{\hbar c}\right) = 10^{-A} = 10^{-\varepsilon cZ} \qquad (11)$$

where A is absorbance (=optical density), I(Z) is the intensity at point Z, I(o) is the intensity at Z=o, c is the concentration in moles per liter of absorbing centers, and $\varepsilon$ is molar extinction coefficient. This expression leads to an equation for the absorbance,

$$\frac{A_\pm}{\varepsilon} = \left(\frac{\varepsilon_\pm}{\varepsilon}\right) cZ = \gamma_\pm \left\{ \Sigma_{a,j} \left(\frac{N_a}{N}\right) |\langle a|m_\pm|j\rangle|^2 \, \delta(\varepsilon_{ja} - \varepsilon)\right\} cz \quad (12)$$

where

$$\gamma\pm = \frac{N_o \pi^2 \alpha^2 \log_{10} e}{250\, \hbar c n_\pm}$$

and $N_o$ is Avogadro's number and $N_a/N$ is the relative population of absorbers in the ground state a. The terms $\langle a|m_\pm|j\rangle$ are electric dipole transition moments. Equation (12) assumes that the interaction between absorbing centers is negligible (i.e., the concentration of the species is sufficiently low and Beer's law is obeyed). Further it does not allow for nonlinear phenomena that would occur at high light intensities. This equation also does not allow for magnetic dipole or electric quadrupole transitions. Note that the neglect of radiation lifetimes produces infinitely sharp transitions.

Equation (12) leads further to the basic formula for the circular dichroism of a system which is the difference in absorption between left CP and right CP light (i.e., the definition of CD can be expressed as $\Delta A = A_- - A_+$).

$$\frac{\Delta A}{\varepsilon} = \gamma_a \Sigma_{a,j} \left(\frac{N_a}{N}\right) [\,|\langle a|m_-|j\rangle|^2 - |\langle a|m_+|j\rangle|^2]\, \delta \left\{(\varepsilon_{ja} - \varepsilon)\right\} cZ \quad (13)$$

where $\gamma = \gamma_+ = \gamma_-$ and $n_+ = n_- = n$. Equation (13) is general and can be applied to natural circular dichroism which is the property of optically active molecules. MCD is not a perturbation of natural optical activity but arises from different polarizabilities which are zero when an external magnetic field is absent.

Consider now a system which has no natural circular dichroism and no magnetic field is present. For this system $|\langle a|m_+|j\rangle|^2 = |\langle a|m_-|j\rangle|^2$ and $A_+ = A_-$ then $A = A_- - A_+ = 0$. In the electric dipole approximation natural CD does not exist and only MCD is observed. Therefore, we can define the zero-field absorption (ZFA) as

$$A = A_+ - A_- = \tfrac{1}{2}\,(A_+ + A_-) \qquad (14)$$

We can apply the Born-Oppenheimer approximation (BO) and the Franck-Coudon approximation (FC) to a description of the ZFA. Within the BO approximation, electronic wavefunctions are separable into nuclear and electronic terms. The zero-field eigenstates can be written as a product of wavefunctions.

$$|A_\alpha\ a\rangle = \Psi_{A_\alpha}(r,R)\chi_a\ (R) \qquad (\alpha = 1 \text{ to } d_A) \qquad (15)$$

$$|J_\lambda\ j\rangle = \Psi_{J_\lambda}(r,R)\chi_j\ (R) \qquad (\lambda = 1 \text{ to } d_J) \qquad (16)$$

where R is the nuclear coordinate, r is the electronic coordinate, $d_A$ and $d_J$ are the degeneracies of the two states a and j, respectively, and $\chi_a$ (R) and $\chi_j$ (R) are vibrational wavefunctions, and $\Psi$ is the electronic wavefunction. $\Psi$ is dependent upon the instaneous nuclear configuration whereas $\chi_a$ (R) and $\chi_j$ (R) are dependent upon the nuclear coordinate R in the region of the equilibrium configuration $R_\circ$ if nuclear motion is small. The zero-field eigenfunction equations within the BO approximation can be written

$$\begin{aligned} \overset{\circ}{H}_{\circ}\ A_\alpha\ a > &= \varepsilon_a |A_\alpha\ a > \\ \overset{\circ}{H}_{\circ}\ J_\lambda\ j > &= \varepsilon_j |J_\lambda\ j > \end{aligned} \tag{17}$$

In order to simpli$\overset{f}{g}$y the transition matrix elements, we can employ the FC approximation

$$\begin{aligned} <A_\alpha\ a|m_\pm|J_\lambda\ j > &= <A_\alpha\ a|m_\pm{}^e + m_\pm{}^n|J_\lambda\ j > \\ &= <a|<A_\alpha\ m_\pm{}^e|J_\lambda> + m_\pm{}^n<A_\alpha|J_\lambda>|j > \\ &= <a|j><A_\alpha|m_\pm{}^e|J_\lambda>^\circ \end{aligned} \tag{18}$$

where e and n refer to the electronic and nuclear terms, respectively, and the superscript zero indicates that the electronic matrix element is evaluated at equilibrium configuration ($R = R_\circ$). The Zeeman splittings of the ground and excited states will be equal to the pure electronic splittings of $R_\circ$ and are independent of the vibrational levels. The FC approximation is inadequate for the transition which is only weakly allowed, and in such cases further account must be taken of the R dependence of the electronic wavefunction. Equation (13) now becomes:

$$\frac{A_\pm}{\varepsilon} = \gamma\left\{\frac{1}{d_A}\ {}_{\alpha,\lambda}\Sigma\,|<A_\alpha|m_\pm{}^e|J_\lambda>^\circ|^2\right\}\left\{{}_{a,j}\Sigma\ \frac{N_a}{N}|<a|j>|^2\,\delta\,(\varepsilon_{ja} - \varepsilon)\right\}\ cz \tag{19}$$

where $N_a$ is the total occupancy of vibrational level a. Integrating the absorption over the whole band of vibronic transitions and assuming that $\gamma$ is constant over this interval yield

$$\int \frac{A_\pm}{\varepsilon}\, d\varepsilon = \gamma_{\alpha,\lambda}^{\Sigma} \frac{1}{d_A} \left|\langle A_\alpha | m_\pm{}^{e} | J_\lambda \rangle^{\circ}\right|^2 cZ \tag{20}$$

If we let

$$D_\circ = \frac{1}{d_A}\; {}_{\alpha,\lambda}^{\;\Sigma} \left|\langle A_\alpha | m_+{}^{e} | J_\lambda \rangle^{\circ}\right|^2 \tag{21}$$

$$= \frac{1}{2d_A}\; {}_{\alpha,\lambda}^{\;\Sigma} \left[\left|\langle A_\alpha | m_+{}^{e} | J_\lambda \rangle^{\circ}\right|^2 + \left|\langle A_\alpha | m_-{}^{e} | J_\lambda \rangle^{\circ}\right|^2\right]$$

and

$$f(\varepsilon) = {}_{a,j}^{\;\Sigma} \left(\frac{N_a}{N}\right) |\langle a | j \rangle|^2\, \delta\,(\varepsilon_{ja} - \varepsilon) \tag{22}$$

where $\int_\circ^\infty f(\varepsilon)\, d\varepsilon = 1$, $\alpha$ and $\lambda$ are electronic sublevels, and $d_A$ is the degeneracy of the ground state. The factor of 2 enters in equation (21) because in the absence of field perturbation, absorbance is equal for light of either polarization. This can be expressed as

$$\langle A_\alpha | m_\pm{}^{e} | J_\lambda \rangle = \langle A_\alpha | m_-{}^{e} | J_\lambda \rangle = \langle A_\alpha | m_+{}^{e} | J_\lambda \rangle \tag{23}$$

The zero-field absorbance within the BO and FC approximations is given by

$$\frac{A_\pm}{\varepsilon} = \gamma D_\circ f(\varepsilon) cZ \tag{24}$$

where c is the concentration, Z is the pathlength, and the superscript zero indicates evaluation at the equilibrium position, $R_o$, by the FC approximation. Note that the zero field absorbance dispersion depends only upon the ground and excited state vibrational functions, and the total integrated intensity is temperature independent whereas the line shape factor f(ε) is temperature dependent via the Boltzmann term ($N_a/N$ is equation (22)).

It is now possible to apply the BO and FC approximations to the molecules in the presence of a magnetic field. The applied field introduces a perturbation term in the Hamiltonian of the system since the absorption coefficients, $k_{\pm}$, exhibit field dependence. In order to obtain the Hamiltonian of the system, the perturbation Hamiltonian, H', due to the external magnetic field must be added to the Hamiltonian, $H_o$, of equation (8). The Hamiltonian for the system can be expressed as

$$H = H_o + H' \tag{25}$$

Interaction with the nuclei can be ignored since nuclear magnetons (gyromagnetic factors) are at least three orders of magnitude smaller than the electronic magneton. If we only consider electronic contributions to the first order magnetic field perturbation, we can write the perturbation Hamiltonian of the form

$$H' = - \sum_i \frac{e}{2mc} (l_{z_i} + 2 s_{z_i}) H \tag{26}$$

where e and m are the electron charge and mass, and i sums over all electrons, $l_{z_i}$ is the z component of the orbital angular momentum of the ith electron and $s_{z_i}$ is the Z component of the spin angular momentum of the ith electron. H is the magnitude of the magnetic field directed along the Z axis; summing over all electrons yields

$$H' = -\mu_Z H = \beta(L_Z + 2 S_Z) H \tag{27}$$

where $\mu_Z$ is the Z component of the electronic magnetic moment operator, $\beta$ is the electronic Bohr magneton ($\beta = |e|\hbar/2mc = 4.6681 \times 10^{-5}$ cm$^{-1}$/gauss), and $L_Z$ and $S_Z$ are the Z components of the total orbital and spin angular momentum operators. The Zeeman splittings induced by the magnetic field lead to population changes in the ground state. The Boltzmann term in equation (22) can be written in terms of the magnetic moments and the external magnetic field:

$$\frac{N_\alpha}{N} = \frac{d_\alpha \exp\left\{-<A_\alpha|L_Z + 2 S_Z|A_\alpha>\beta H/kT\right\}}{\sum_\alpha d_\alpha \exp\left\{-<A_\alpha|L_Z + 2 S_Z|A_\alpha>\beta H/kT\right\}} \tag{28}$$

where $\alpha$ sums over the Zeeman states of A. At high temperatures where Zeeman energies are small compared to kT, and/or low field strengths, the exponential can be expanded via

$$e^{-x} = 1-x + \frac{x^2}{2!} - . . . \tag{29}$$

whereby

$$\frac{N_\alpha}{N} = \frac{1}{d_A} \left\{1 - <A_\alpha|L_Z + 2 S_Z|A_\alpha>\beta H/kT\right\}. \tag{30}$$

If the Zeeman shift does not change the shape of the absorption band and merely changes the position of the band along the energy axis, the shifted lineshape function can be expressed in terms of the unshifted function by a Taylor's series expansion. This approach is called the rigid shift approximation and is especially valid for broad bands where the Zeeman shift is small compared with the bandwidth.

Having evaluated the effects of the magnetic field on transition energies and moments and on ground state populations, the definition of CD (i.e., $\Delta A = A_- - A_+$) with equations (19) and (28) gives a parametric equation for the

$$\frac{\Delta A}{\varepsilon} = \gamma\left\{A_1 \left(-\frac{\delta f}{\delta \varepsilon}\right) + \left(B_0 + \frac{C_0}{kT}\right)f\right\}\beta H c Z \qquad (31)$$

where all symbols are as previously defined except for the parameters $A_1$, $B_0$ and $C_0$ which are given by

$$\begin{aligned} A_1 = &+ \frac{1}{d_A} \sum_{\alpha,\lambda} \left[ |\langle A_\alpha|m_-^e|J_\lambda\rangle^\circ|^2 - |\langle A_\alpha|m_+^e|J_\lambda\rangle^\circ|^2 \right] \\ &\times \left[\langle J_\lambda|L_Z + 2\,S_Z|J_\lambda\rangle^\circ - \langle A_\alpha|L_Z + 2\,S_Z|A_\alpha\rangle^\circ\right] \end{aligned} \qquad (32)$$

$$\begin{aligned} B_0 = &- \frac{2}{d_A} \sum_{\alpha,\lambda} \mathrm{Re} \left\{ \sum_{K\neq J} [A_\alpha|m_-^e|J_\lambda\rangle^\circ \langle K_K|m_+^e|A_\alpha\rangle^\circ \right. \\ &- \langle A_\alpha|m_+^e|J_\lambda\rangle^\circ \langle K_K|m_-^e|A_\alpha\rangle^\circ] \times \frac{\langle J_\lambda|L_Z + 2\,S_Z|K_K\rangle^\circ}{\overset{\circ}{W}_K - \overset{\circ}{W}_J} \\ &+ \sum_{K\neq A} [\langle A_\alpha|m_-^e|J_\lambda\rangle^\circ \langle J_\lambda|m_+^e|K_K\rangle^\circ - \langle A_\alpha|m_+^e|J_\lambda\rangle^\circ \\ &\langle J_\lambda|m_-^e|K_K\rangle^\circ] \times \frac{\langle K_K|L_Z + 2\,S_Z|A_\alpha\rangle^\circ}{\overset{\circ}{W}_K - \overset{\circ}{W}_A} \end{aligned} \qquad (33)$$

$$C_\circ = -\frac{1}{d_A} \sum_{\alpha,\lambda} [\,|\langle A_\alpha|m_-^{\,e}|J_\lambda\rangle^\circ|^2 - |\langle A_\alpha|m_+^{\,e}|J_\lambda\rangle^\circ{}^2] \times \langle A_\alpha|L_Z + 2\,S_Z|A_\alpha\rangle^\circ \tag{34}$$

The shape of the MCD spectrum can be deconvolved into the $A_1$, $B_\circ$ and $C_\circ$ terms or conversely, by calculating these terms the sign and shape of the MCD spectrum can be predicted. The magnitudes of the three terms to the MCD can be estimated by the relations

$$A_1 : B_\circ : C_\circ \sim \frac{Z}{\Gamma} : \frac{Z}{\Delta W} : \frac{Z}{kT} \tag{35}$$

where Z is the Zeeman energy, $\Gamma$ is the bandwidth (i.e., full width at half maximum) of the ZFA band, $\Delta W$ is the electronic energy gap, k is the Boltzmann constant, and T is the absolute temperature. The experimental form of the $A_1$, $B_\circ$ and $C_\circ$ terms is illustrated in Figure 1.

The existence of an $A_1$ term indicates that either ground or excited state is degenerate. The $A_1$ term depends upon the bandwidth of the transition since it is multiplied by the derivative of the lineshape function, $\frac{\delta f}{\delta \varepsilon}$. (see Equation 31). The $A_1$ term also depends upon magnetic moments and CP transition moments which in turn relate both to the symmetries and to the specific natures of the electronic states. If the magnetic moments for the ground and excited states are equal, no $A_1$ term will be observed.

$B_\circ$ terms are a general property of all MCD spectra and depend upon mixing of the electronic wavefunctions by the magnetic field perturbation. The $B_\circ$ term has the same shape as the absorption band and may be positively or negatively signed.

FIGURE 1. The appearance of the experimental form of the $A_1$, $B_o$ and $C_o$ terms predicted by MCD theory.

(a) The zero field absorption (below) and MCD (above) for a transition with a positive $A_1$ term. The positive lobe lies at higher energy.

(b) A $B_o$ term may be either positive or negative, the maximum coincides in energy with that of the absorption maximum.

(c) A negative $C_o$ term at two temperatures, $T_{high}$ and $T_{low}$. The sign of $C_o$ terms may be either positive or negative, and the maximum coincides with that of the absorption maximum.

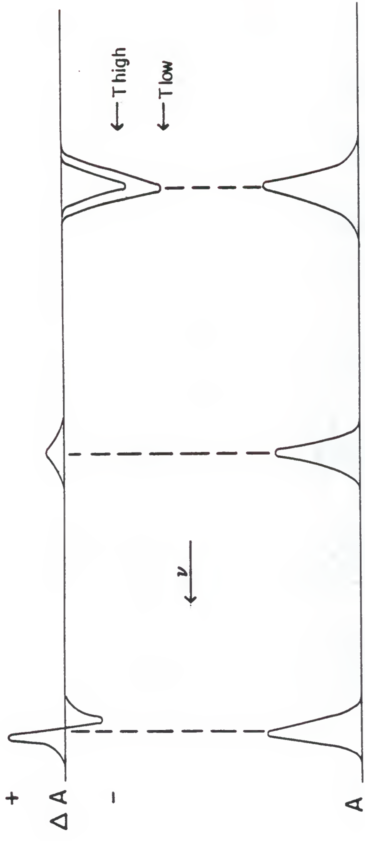
+
Δ A
−
A
(a)
(b)
(c)
ν
T high
T low

The presence of a $C_o$ term demonstrates that the ground state is degenerate. Like $A_1$ terms, $C_o$ terms depend upon the magnetic moment of the ground state and the CP transition moments. The $C_o$ term may be positively or negatively signed and will follow the shape of the absorption band.

In order to illustrate the origin of $A_1$ and $C_o$ terms in the MCD, magnetic field splittings of the ground state and excited state for the simplest atomic transitions $^1P \leftarrow {}^1S$ and $^1S \leftarrow {}^1P$ are shown in Figure 2. As mentioned before, the $A_1$ term arises when either the excited state or the ground state is split by the applied magnetic field while the $C_o$ term arises only if the ground state is split. A positive $A_1$ term is shown (see Figure 1) where the positive lobe appears at higher energy which in turn indicates that the absorption of left CP light is more energetic than right CP light. Note that in $A_1$ term the two lobes are always oppositely signed but of equal magnitude. The magnetic field splitting of the ground state can occur for the different cases (i.e. low and high temperature). If the temperature is high, the population of all magnetic sublevels within the ground state will be equal and the $C_o$ term curve of the MCD dispersion will be as illustrated in the middle spectrum (see Figure 2). If, however, the temperature is lowered, the population of the lowest sublevels within the ground state will increase (due to Boltzmann distribution statistics). This will result in an increase in the intensity of the lobe for the lower sublevels, and a decrease in the intensity of the lobe for the higher sublevels (see the dashed curve in the spectrum on the right in Figure 2).

FIGURE 2. Magnetic field splittings of ground and excited states illustrating the origin of $A_1$ and $C_0$ terms.

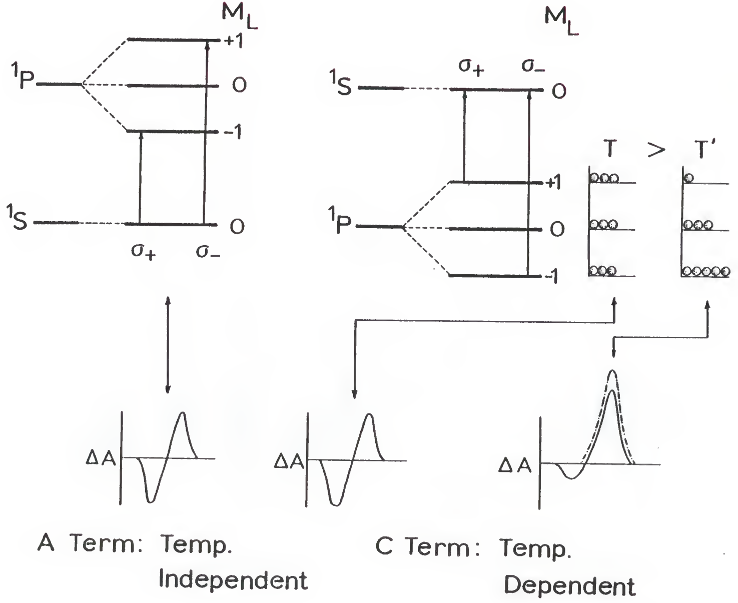
$M_L$
$^1P$
+1
0
-1
$^1S$
0
$\sigma_+$
$\sigma_-$
$M_L$
$^1S$
$\sigma_+$
$\sigma_-$
0
$^1P$
+1
0
-1
T > T'
ΔA
ΔA
ΔA
A Term: Temp. Independent
C Term: Temp. Dependent

The following characteristics summarize the basis for detecting and qualitatively interpreting the MCD spectra:

(1) An $A_1$ term spectrum changes sign at the absorption maximum, while $B_o$ and $C_o$ spectra maximize or minimize at the maximum of the electronic absorption band.

(2) A $C_o$ term spectral intensity is inversely proportional to the absolute temperature (see Equation 31), while a $B_o$ term is independent of temperature.

(3) An $A_1$ term spectrum is possible only if the ground or excited state involved in the electronic transition is degenerate and has angular momentum.

(4) A $C_o$ term spectrum is possible only if the ground state is degenerate and has angular momentum.

## Selection Rules for MCD

Photons possess well-defined values of angular momentum and can be absorbed or emitted by systems which are characterized by well-defined values of their angular momenta.[47] The conservation of angular momentum must be taken into account when the selection rules are derived from the transitions which involve photons. Any isolated atom may contain spin angular momentum (S) as well as orbital angular momentum (L) which may interact to some extent. If the interaction of S and L is so strong, these quantum numbers will not be valid to derive the selection rules and in such cases (called Hund's case C) the total angular momentum (J) must be taken into consideration. This strong coupling often occurs in species containing nuclei with high atomic number and J is the only valid quantum number for these species.

Consider the transition which may occur in an isolated atom with total angular momentum J. In the absence of a magnetic field the state is 2J+1-fold degenerate which corresponds to the number of distinct eigenvalues $m_J$. If an external magnetic field is applied, this degeneracy will be lifted by the space quantization imposed by the direction of the field. The Zeeman splittings of the eigenstates of atoms with total angular momentum J = 0 and J = 1 in the presence of a magnetic field along with possible transitions is shown in Figure 3.

The absorption probability of a photon of electric dipole radiation for a transition from state a to j is proportional to the square of the transition dipole moment matrix element along the direction of the photon polarization.

$$(\vec{u} \cdot \vec{m}_{ja}) \quad (\vec{u} \cdot \langle a|m|j\rangle) \tag{36}$$

where $\vec{u}$ is a unit vector which determines the polarization of the light, and $\vec{m}_{ja}$ is the transition electric dipole moment. Note that there are three possible polarizations of light along the X, Y and Z direction in a Cartesian coordinate system (i.e., $\vec{u}_X$, $\vec{u}_Y$ and $\vec{u}_Z$). By considering these possible polarizations and also the properties of the wavefunctions as described by the spherical harmonics,[47] the selection rules for the three transitions a, b and c in Figure 3 can be derived.

Let us first begin by considering the $\vec{u}_Z$ (polarization parallel to the field), Equation (36) vanished for all cases except where $\Delta J = \pm 1$ and $\Delta M_J = 0$. Since the Z polarization

FIGURE 3. Magnetic field splittings and polarized transitions to an atomic P state. Transition a is right circularly polarized, transition c is left circularly polarized, and transition b is polarized parallel to the magnetic field.

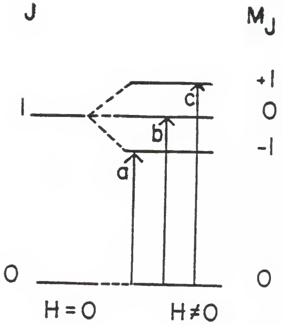
J
M_J
+1
1
0
-1
c
b
a
0
0
H = 0
H ≠ 0

is the propagation direction of light in MCD and is unavailable, there is no MCD in this case. Linear combinations of the other two possible polarizations of the light ($\vec{u}_X$ and $\vec{u}_Y$) can be written as $\vec{u}_X \pm i\ \vec{u}_Y$ and compared to the two possible circular polarizations (the + contribution for right CP, and the - contribution for left CP). For right CP light, equation (36) vanishes except for $\Delta M_J = M_{J'} - M_{J''} = -1$, and $\Delta J = \pm 1$ while for left CP light this equation vanishes except for $\Delta M_J = +1$, and $\Delta J = \pm 1$. We can conclude that transition a in Figure 3 will correspond to right CP and transition c will correspond to left CP, where transition b will not be observed. The CP light corresponds to electric dipole photons having J = 1 and $M_J = +1$ for left CP and $M_J = -1$ for right CP.

If, however, the interaction of the S and L is weak, these quantum numbers can be used to derive the selection rules and such cases (called Hund's case a) often occur in species containing light nuclei. The MCD selection rules for this situation are $\Delta M_L = \pm 1$ and $\Delta M_S = 0$. It is worthwhile to note that the Hund's case c and a are the extreme situations, and often atoms display properties intermediate between these two cases.

## Spectral Moment Analysis

In 1965, Henry, Schnatterly, and Slichter (HSS)[48] introduced the method of moments to extract valuable information from broad, generally featureless bands. They formulated the theoretical framework for the relationship between the moments of the F center bands and the changes in these moments with applied perturbations to the interactions (spin-orbit, vibronic) within an excited ${}^2T_1$ state. Osborne and Stephens (OS)[49] modified the theory and applied it to an MCD study of the F centers in LiF.

The moments of a spectrum are averaged properties where the nth moments of the ZFA and MCD are defined by

$$\langle A\rangle_n^{\varepsilon^\circ} = \int \frac{A}{\varepsilon} (\varepsilon - \varepsilon^\circ)^n \, d\varepsilon \tag{37}$$

and

$$\langle A\rangle_n^{\varepsilon^\circ} = \int \frac{\Delta A}{\varepsilon} (\varepsilon - \varepsilon^\circ)^n \, d\varepsilon \tag{38}$$

where A and ΔA are the optical absorbance and differential absorbance $A_L - A_R$, respectively, and $\varepsilon^\circ$ the average energy of the ZFA (i.e., the energy of the center of the band about which the moment is taken), is defined by

$$\varepsilon^\circ = \frac{\int A d\varepsilon}{\int \frac{A}{\varepsilon} d\varepsilon} \tag{39}$$

The method of moments can be employed to derive the experimental values for $A_1$, $B_0$ and $C_0$ terms from the MCD spectra.[46] Note that the subscripts of $A_1$, $B_0$ and $C_0$ terms are related to the moment integrated for ΔA. The zeroth moments of A and ΔA are simply the integrated areas of $\frac{A}{\varepsilon}$ and $\frac{\Delta A}{\varepsilon}$ while the higher moments emphasize different aspects of the band shapes. For example, $\langle A\rangle_2^{\varepsilon^\circ} / \langle A\rangle_0$ is a measure of the ZFA width, and $\langle A\rangle_3^{\varepsilon^\circ}$ is sensitive to its skewness. The ratio of the nth MCD moments to the zeroth absorption moment is given by

$$\frac{\langle\Delta A\rangle_n}{\langle A\rangle_\circ} = \left(A_n + B_n + \frac{C_n}{kT}\right)\frac{\mu_B B}{D_\circ} \qquad (40)$$

where $\mu_B$ is the Bohr magneton, B is the magnetic field strength, and the MCD parameters $A_n$, $B_n$, $C_n$ and $D_\circ$ are defined in HSS[48] and OS.[49]

In order to evaluate the moments properly, the band must be completely resolved from neighboring bands at all fields (i.e., the absorption of the band is zero on either side of it). The moments must be taken over the entire set of vibronic transitions allowed in conjunction with the electric excitation. As n in equations (37) and (38) increases the contribution of outer wings of the band will increase heavily.

For some of the transitions in this study, the use of the method of moments has been limited by the incomplete resolution of the band from the neighboring bands. However, a moment analysis for the $^5P \leftarrow {}^5D$ and $^5F \leftarrow {}^5D$ transitions of iron atom, the $^6P \leftarrow {}^6S$ transition of manganese atom in a Kr matrix, and the $^7P \leftarrow {}^7S$ transition of chromium atom isolated in Xe matrices, is presented in the following chapters.

# CHAPTER III

# APPARATUS

In this chapter a detailed description of the matrix isolation apparatus employed in preparation of a matrix sample as well as the spectroscopic apparatus used in the absorption and MCD experiments will be presented.

## Matrix Isolation Apparatus

In order to prepare a matrix-isolated sample of high temperature atoms or molecules, one must utilize a high vacuum system including a furnace assembly for vaporization of the sample and a cold surface for codeposition of the sample with a large amount of host atoms or molecules. Deposition of a matrix sample required low enough pressure that the effusing metal gas atoms had a mean free path greater than the distance between the furnace and cold window; otherwise, they would be scattered out of the beam.

The entire system was rough pumped to a pressure of less than 200 microns by bypassing the diffusion pump with a 0.25 inch copper line to a Welsh Scientific Company Duo Seal Model 1400 mechanical fore pump. Rough pumping of the system was monitored via a thermocouple gauge which was mounted on the same copper line. The diffusion pumping system was a 2 inch Consolidated Vacuum Company diffusion pump charged with Dow Corning 704 silicone oil. When the pressure of the entire assembly was below 200 microns, the diffusion pump was opened to the system via a 2 inch diameter Consolidated Vacuum Company (CVC) gate valve. A diagram of the vacuum components is shown in Figure 4. A stainless steel liquid nitrogen trap, between the gate valve and the diffusion pump, maintained the pressure of the system below $1 \times 10^{-6}$ torr. An ionization gauge, mounted between the furnace and the gate valve, monitored the system pressure when the diffusion pump was turned on. Both the thermocouple and ionization gauges were connected to a Granville-Phillips Series 270 Gauge Controller.

Figure 5a shows the furnace assembly used in the absorption and MCD experiments. In order to generate metal beams, the Knudsen cell was heated resistively by passing an alternating current up to 300 amp, 60 Hz through the copper electrodes. The high current was achieved by a Variac$^{R}$ variable transformer and a step-down transformer.

The Knudsen cell assembly was made from either 0.015 inch wall thickness, 0.250 inch outer diameter or 0.017 inch wall thickness, 0.500 inch outer diameter tantalum tubing and closed on either end by a tantalum end cap. A small hole (~ 0.05 inch) was put in the cell to allow outflow of the enclosed metal powder. The cell was mounted by tantalum straps and copper screws to two water cooled copper electrodes. One of these electrodes was electrically isolated from the furnace while the other was electrically in contact with the furnace flange. Therefore, when using the magnetic shutter, one had to use a teflon isolator to prevent the magnet arcing across the electrodes. The Knudsen cell is illustrated in Figure 5b.

FIGURE 4. A diagram of the vacuum system.

A. Inlet to furnace
B. Ionization gauge
C. Gate valve
D. Liquid nitrogen trap
E. Baffle
F. Diffusion pump
G. High pressure port valve
H. Thermocouple gauge
I. Bypass valve
J. To rough pump

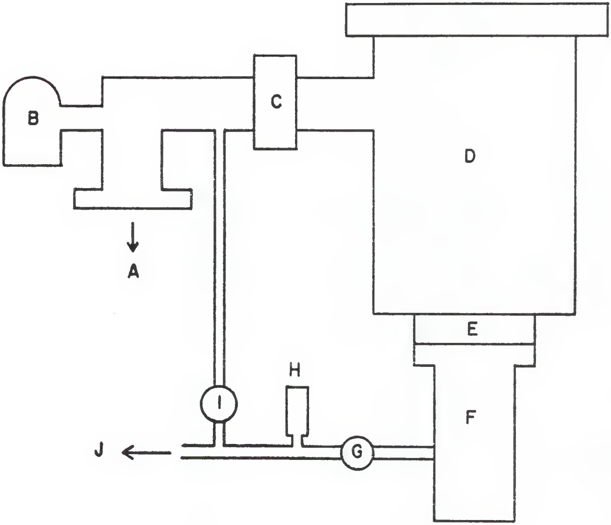
B
C
D
A
E
H
I
F
J
G

FIGURE 5. Diagrams of the furnace assembly and Knudsen cell.

(a) Diagram of the furnace assembly.

(b) Diagram of Knudsen cell used for metal vaporization.

(a)

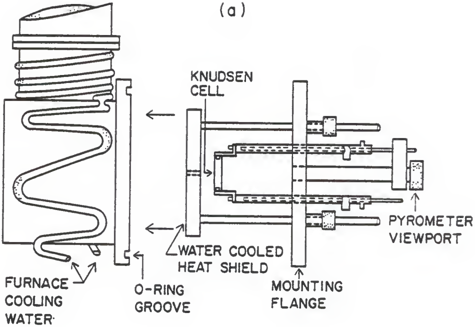
KNUDSEN CELL
WATER COOLED HEAT SHIELD
MOUNTING FLANGE
PYROMETER VIEWPORT
FURNACE COOLING WATER
O-RING GROOVE

(b)

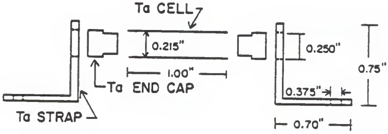
Ta CELL
0.215"
1.00"
Ta END CAP
Ta STRAP
0.250"
0.75"
0.375"
0.70"

The furnace was cooled by the flowing of water through 0.25 inch diameter copper tubing soldered to the outer surface of the furnace. To maintain the integrity of the furnace "O" ring seals during deposition at temperatures above 1800 °C, it was necessary to cool the furnace by wrapping it with wet cotton strips and pouring liquid nitrogen on the furnace.

A Leeds and Northrup optical pyrometer was employed to measure the surface temperature of the cell by raising the magnetic shutter. Except during temperature measurements, the magnetic shutter remained closed to avoid metallic depositions on the viewport of the window, because the resulting metallic film caused inaccuracies in temperature readings.

A water-cooled heat shield was placed in the furnace to prevent heating of the cold window by radiant flux from the Knudsen cell. The heat shield was made from two 0.125 inch copper plates which were soldered to either side of a 0.25 inch diameter copper tube spiral. The sample species effusing from the Knudsen cell passed through a 0.125 inch diameter hole, which was drilled at the center of the heat shield, and impinged on the cold window. It is worth noting that this heat shield also improved the collimation of the metal beam, thus increasing the thermal load of hot atoms or molecules striking the cold window rather than the other parts of the cryostat. To ensure that the metal beam impinged properly toward the cold window, care had to be taken when aligning the Knudsen cell effusion hole and the heat shield hole.

The metal beam effusing from the cell was codeposited with an inert gas on the surface of the sample window. The temperature of the sample window was maintained at ~11 °K using an Air Product Displex$^R$ Model CS 202 closed cycle helium refrigerator. This window was a 1 inch diameter, 4 mm thick, and UV grade $CaF_2$ plate. The window frame was made from high purity, oxygen-free copper and was mounted by a ¼"-28 threaded stud and an indium gasket to the second stage of the refrigerator. Indium gaskets were also used to improve thermal conduction between the sample window and its holder and between the radiation shield and the first stage of the cryostat.

The cold window temperature was set by use of an Air Product APD-B temperature controller and monitored by using a Chromel-Au, 0.07% Fe thermocouple which was mounted near the middle of the copper window assembly, and referenced to liquid nitrogen. The temperature of the cold window was controlled by a 10 watt variable duty cycle heater attached to the cold tip. The sensitivity of the Air Products temperature controller was in the range of ±2 °K. In later experiments a Lake Shore Cryotronics, Inc. Model DRC-80C temperature controller was employed. This controller utilized silicon diode detectors with a temperature sensitivity in the range of ±0.1 °K. The silicon detector was mounted in a hole which was drilled into the upper part of the copper window assembly.

The cryostat was a two stage, closed cycle helium refrigerator which made use of the Joule-Thompson effect by expanding compressed helium gas. The cold window assembly was surrounded by a nickel-plated copper radiation shield attached to the first stage of the Displex while the copper cold tip was attached to the second stage of the cryostat. The radiation shield maintained at 40-60 °K acted as a thermal barrier for heat transfer to the lower stage and copper window frame. The closed cycle cryostat could rotate ninety degrees in either direction inside its permanently-positioned outer vacuum shroud and the two holes 180° apart in the heat shield allowed sample deposition and optical alignment for the absorption and MCD experiments.

A diagram of the furnace-cryostat assembly is shown in Figure 6. The 2 inch diameter suprasil-1 quartz windows were attached to three sides of the cryostat shroud by O-ring seals. The remaining side of the cryostat assembly was connected to a gate valve which in turn was connected to a second gate valve attached to the furnace assembly by a short brass tube (Figure 6). To perform the MCD experiments, the two gate valves should be separated and the cryostat assembly rolled along the rails into a compact electromagnet.

The inlet nozzle for the matrix gas was constructed from a 16 gauge Yale stainless steel needle silver-soldered to a 0.25 inch diameter stainless steel tube. This tube was silver-soldered via a hole in the wall of a short brass tube. The brass tube connected the furnace assembly to the second gate valve. The inlet nozzle assembly was joined via a 0.25 inch vacuum quick connect to a 0.25 inch stainless steel tube which was in turn joined to a glass inert gas manifold. The rare gas inlet system is diagrammed in Figure 7. The inert gas flow into the vacuum system was controlled by a Nupro

FIGURE 6. Diagram of the furnace-cryostat assembly used in matrix isolation experiments.

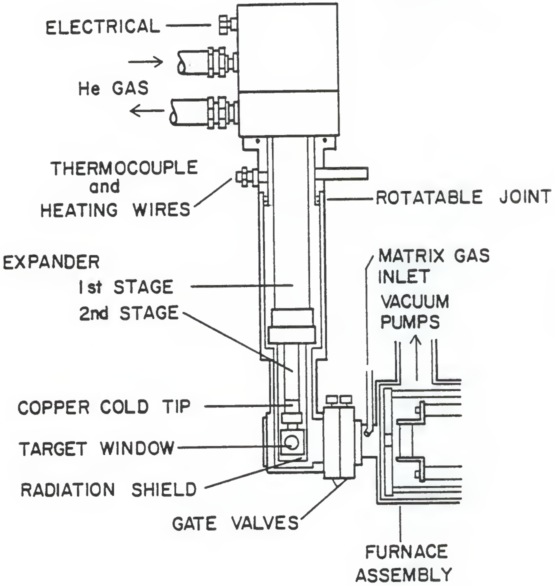
ELECTRICAL
He GAS
THERMOCOUPLE
and
HEATING WIRES
ROTATABLE JOINT
EXPANDER
1st STAGE
2nd STAGE
MATRIX GAS
INLET
VACUUM
PUMPS
COPPER COLD TIP
TARGET WINDOW
RADIATION SHIELD
GATE VALVES
FURNACE
ASSEMBLY

FIGURE 7. A diagram of the rare gas inlet system.

A. To diffusion pump
B. Liquid nitrogen trap
C. Three-liter gas storage bulbs
D. Ionization gauge
E. Mercury manometer
F. Isolant gas cylinder
G. Liquid nitrogen trap
H. To inlet nozzle
I. Extra-fine metering valve

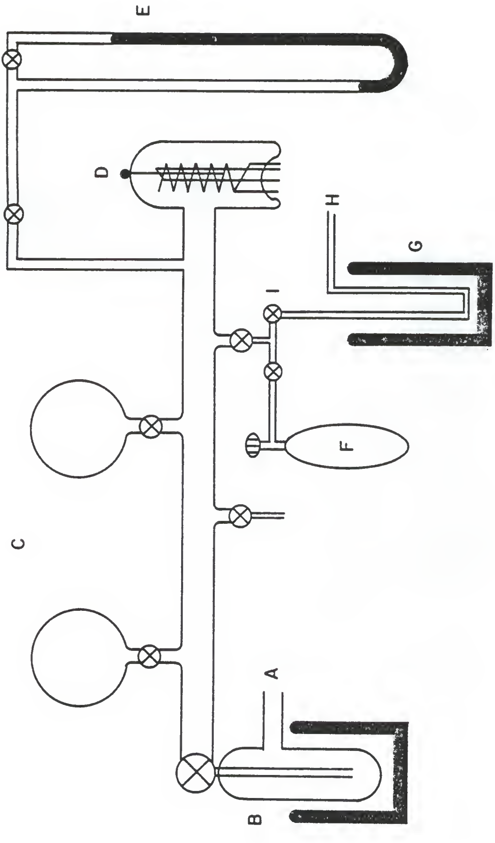
A
B
C
D
E
F
G
H
I

¼" extra fine metering valve. A 0.25 inch stainless steel needle valve was employed to control the rare gas loading into the glass line. Ace Glass Company Teflon$^R$ valves with o-ring seals were used for other connections in the gas manifold. Two reservoir bulbs were attached to the gas manifold to increase the efficiency of gas-loading and also to allow rapid change between different matrix gases. Before loading the matrix gas, the entire gas manifold was pumped by a 3 inch Varian M2 diffusion pump charged with 100 ml of Dow Corning 704 silicone oil. The flow rate of the inert gases was monitored via a standard mercury manometer.

## Spectroscopic Apparatus

During sample deposition the cold window was faced toward the evaporation furnace and matrix gas nozzle. After deposition was complete, the cryostat was rotated ninety degrees such that the sample window was intercepted by the light beam and ready to run the absorption experiment. Both the absorption and MCD optical components (source, monochromator, photomultiplier tube, etc.) were mounted on a pair of 3' x 4' aluminum tables.

The absorption optics are diagrammed in Figure 8. A pseudo-double-beam apparatus was used for the absorption measurements. The reference beam was not passed through the sample window but reflected by a set of mirrors around the cryostat and impinged on the detector. The light source used in absorption and MCD measurements was a 300-watt Eimac$^R$ high-pressure xenon lamp made by Varian Associates. The lamp operated at a pressure of 115 atmospheres and had a high

FIGURE 8. Optics for absorption experiments.

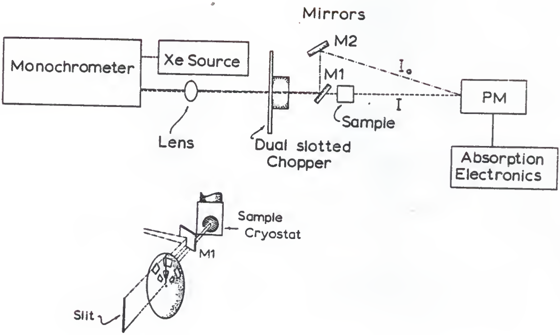
Mirrors
M2
M1
I₀
I
Monochrometer
Xe Source
PM
Lens
Dual slotted Chopper
Sample
Absorption Electronics
Sample Cryostat
M1
Slit

radiant flux, well-collimated beam provided by a built-in parabolic reflector and a sapphire window.

In order to remove ozone gas generated by the xenon lamp, a fan and duct system was mounted above the small hood in which the Xe lamp was enclosed. The output of this lamp was adequate to obtain spectra over the range of 8500 to 2200 Å. At shorter wavelengths, scattering of light from the matrices caused some drift in the baseline of the spectra. The xenon lamp emission spectrum was effectively nulled over most of the spectral range except around 4600 Å which gave poor nulling of the background during absorption experiments. This problem was solved by using an Osram 55 watt tungsten lamp. The small hood was attached to a Spex 0.75 m Czerny-Turner spectrometer with a 1200 line/mm grating blazed at 3000 Å and an aperture of f/6.8. The output of the Xe lamp passed through the spectrometer with the slits generally set for a spectral band pass of less than 6 Å.

The output from the monochromator was collimated by a 3 inch quartz lens (f/3) and then passed through a dual-slotted chopping wheel. The wheel was driven by a hysteresis-synchronous motor at 1800 rpm. Five outer slots chopped the excitation beam at 150 Hz while nine slots chopped the beam at 270 Hz. These frequencies were selected to minimize 60 Hz ac powerline pickup, since neither was an integral multiple of the ac line frequency. The light beam chopped at 270 Hz (sample beam) passed through the sample/matrix and fell on the detector. The light beam chopped at 150 Hz (reference beam) was reflected around the sample/matrix cryostat by two Edmund

Scientific aluminized front-surface mirrors ($M_1$, $M_2$, cf. Figure 8) and also impinged on the same detector. An iris was used for attenuation of the reference beam.

The chopping wheel assembly was furnished with two light emitting diodes (LEDs) and two phototransistors located on the opposite sides of the chopping wheel from the LEDs. The signals from the phototransistors were used as reference signals for both 270 Hz and 150 Hz chopping frequences. Both signals were amplified by two RCA 3140 operational amplifiers.

The detector was an EMI 9683 QB photomultiplier tube. Since the spectral response curve of the photomultiplier tube followed the extended S-20 range, adequate detection of signals over a spectral range of 2200-8500 Å was available. The signal from photomultiplier tube was preamplified to provide a voltage output for the sample and reference signals in the absorption measurements.

A diagram of the electronics for the absorption experiments is given in Figure 9. The output current from the photomultiplier tube ($\sim 10^{-7}$ amp) was converted to a voltage by using a 15 KΩ resistor which was connected to the ground. Part of the signal from the photomultiplier tube was amplified by a factor of 100 by using an Analog Devices 52 K low drift operational amplifier and sent to an oscilloscope for monitoring the wave form during the experiment. The rest of the signal was fed in parallel to the inputs of two phase-sensitive detectors. An Ithaco Dynatrac Model 391A lock-in amplifier was referenced to 270 Hz and used as the reference signal detector. Note that the output of the Model

FIGURE 9. Electronics for absorption experiments.

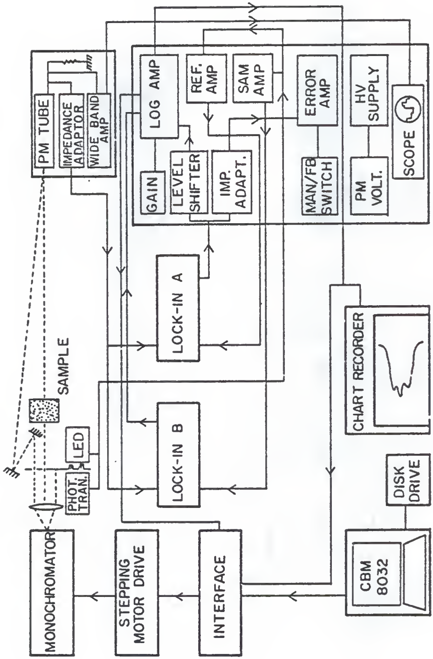
PM TUBE
IMPEDANCE ADAPTOR
WIDE BAND AMP
LOG AMP
REF. AMP
SAM AMP
ERROR AMP
HV SUPPLY
GAIN
LEVEL SHIFTER
IMP. ADAPT.
MAN/FB SWITCH
PM VOLT.
SCOPE
SAMPLE
LOCK-IN A
CHART RECORDER
LED
PHOT. TRAN.
LOCK-IN B
DISK DRIVE
MONOCHROMATOR
STEPPING MOTOR DRIVE
INTERFACE
CBM 8032

353 amplifier was proportional to the lamp emission spectrum, monochromator dispersion-characteristics, and the photomultiplier spectral response while the output of Model 391A amplifier was proportional to the absorption spectrum of the matrix in addition to the factors mentioned above.

The output voltages from the lock-ins were connected to an Analog Devices 757N Log Amplifier/Ratiometer. The Log Amplifier took the logarithm of both signals and performed an analog subtraction to give an absorbance output in the range 0.0 to 1.0 (i.e., log of the ratio of sample to reference intensities = log $I_o/I$ = absorbance). The absorbance output from Log Amplifier was connected in parallel to a Soltec Corporation Model 1242 two channel strip chart recorder and the computer interface.

The computer was a Commodore CMB Model 8032 which was furnished with an interface containing a Datal Systems, Inc., ADC-EK8B analog-to-digital (A/D) converter of 8 bit resolution. The absorbance signal was digitized by the computer interface and stored on a floppy disc by loading into a Commodore CBM Model 8050 dual disc drive. The same interface also allowed computer control of the monochromator wavelength scan such that the sample spectrum was obtainable under program control. The monochromator was driven by pulses sent from the computer to a SLO-SYN$^R$ Model MOGI-FD-301 stepping motor attached to the wavelength scan control. This motor was stepped 200 times per revolution allowing 0.25 Å per step of the monochromator.

The same light source and monochromator were used in the MCD experiments. The light source and monochromator were rolled on case-hardened steel rails and set for the MCD run without removing the chopping wheel assembly. The two gate valves connecting the furnace and cryostat assembly were separated, and the sample closed-cycle cryostat was removed and rolled along rails into a small electromagnet for MCD experiments. The optics for MCD experiments are shown in Figure 10. The light beam from the monochromator was collimated by the same lens and passed through a Glan-Thomson prism oriented at 45° to the optic axis of a Morvue Electronic Systems PEM-3$^{R}$ photoelastic modulator.

The polarized light beam from the modulator was a 50 KHz signal alternating between right and left circularly polarized light. With the sample window positioned in the field of an Alpha Model 4600 electromagnet and aligned in the optical path, a single beam MCD experiment was performed. This compact magnet had a maximum field of 5500 Gauss, a 4 inch adjustable pole face gap, and a 0.75 inch diameter hole colinear with the magnetic field in either end of the pole face.

The MCD electronics are diagrammed in Figure 11. The voltage output of the photomultiplier tube consisted of a relatively small 50 KHz ac component riding on a large dc component proportional to both emission spectrum of the xenon lamp and the sample absorbance. The ac component of the photomultiplier tube which contained the MCD information was fed to an Ithaco Model 353 Lock-in Amplifier, which was

FIGURE 10. Optics for MCD experiments.

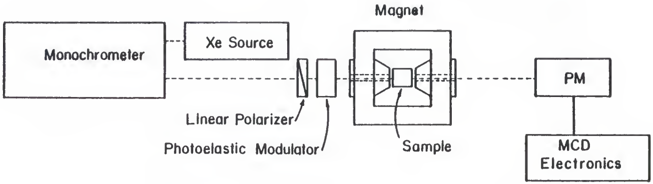
Magnet
Monochrometer
Xe Source
PM
Linear Polarizer
Photoelastic Modulator
Sample
MCD
Electronics

FIGURE 11. Electronics for MCD experiments.

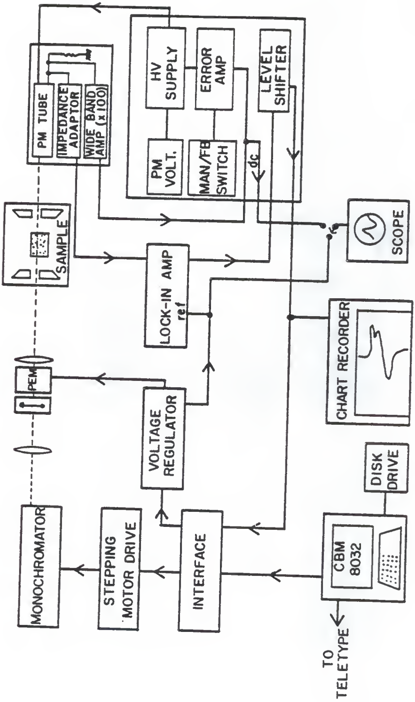
MONOCHROMATOR
PEM
SAMPLE
PM TUBE
IMPEDANCE ADAPTOR
WIDE BAND AMP (x100)
HV SUPPLY
ERROR AMP
LEVEL SHIFTER
PM VOLT.
MAN/FB SWITCH
dc
SCOPE
LOCK-IN AMP
ref
CHART RECORDER
VOLTAGE REGULATOR
STEPPING MOTOR DRIVE
INTERFACE
CBM 8032
DISK DRIVE
TO TELETYPE

locked to a reference frequency (50 KHz) that originated in the photoelastic modulator. Since the output of this lock-in amplifier (i.e., MCD signal) was bipolar, and the A/D interface converter would not accept negative signals, it was necessary to use a dc level shifter to ensure that all analog signals converted by the A/D interface were positive. These positive voltages were suitable inputs for the chart recorder and the computer interface to digitize the sample/ matrix spectra. In later experiments the Ithaco Model 353 was replaced by an EG&G Princeton Applied Research Model 5105 Lock-in Amplifier.

The output from the Analog Devices 52 K operational amplifier was fed to an error amplifier-feedback circuit. The error amplifier read the difference voltage between the actual dc output of the photomultiplier tube and the desired dc level set by the operator. A Bertan PMT-20, option 3 programmable high voltage power supply was employed in construction of the feedback circuit. The output from the Bertan PMT-20 to the photomultiplier tube was controlled by using this difference voltage.

To automatically correct the background effects in the MCD sample spectrum, the dc component of the photomultiplier tube signal was maintained constant. This was accomplished via the feedback circuit which controlled the gain (applied high voltage) of the photomultiplier tube in an inverse relation to the dc output of the photomultiplier tube. The feedback circuit was also used for the later absorption experiments. This was accomplished by passing the output of the lock-in amplifier through another operational amplifier which acted as an impedance adaptor and then into the feedback circuit.

As in the absorption experiment the computer controlled the monochromator and collected the data. The A/D converter with 8 bit resolution was responsible for digitizing the data. The program was allowed to collect the data at 1, 0.5, or 0.25 Å intervals. In the MCD experiments, the computer also controlled the voltage applied to the photoelastic modulator such that the quarter-wave retardation ($\lambda/4$) was constant over the entire wavelength range scanned. The $\lambda/4$ retardation by the modulator depended on the amplitude of the stress applied to the quartz crystal which was linearly dependent on the modulators' input voltage.

The computer program calculated the required voltage level for $\lambda/4$ retardation at each wavelength, and this output was sent to the modulator via a Datel System, Inc., DAC-IC8BC digital-to-analog (D/A) converter. This device was also employed when another program read data from the floppy disc for transferring the output to the chart recorder. For a detailed treatment of the computer programs, the reader is referred to the Ph.D. dissertation of Powell.[37]

# CHAPTER IV

## EXPERIMENTAL TECHNIQUES

In this chapter the general experimental techniques employed in preparation of a matrix isolated sample of the high temperature atoms as well as the various calibration procedures followed in performing the absorption and MCD experiments will be presented. Except for the furnace temperature, the general procedure for matrix preparation was very similar for all the atoms studied.

A tantalum Knudsen cell was loaded with metal powder as fully as possible since some of the fine powder invariably escaped from the cell effusion orifice into the vacuum chamber during rough pumping and outgassing of the furnace.

During cell loading, any dust and films remaining from previous experiments were removed from metal surfaces in the vacuum system by washing with Kimwipes soaked in acetone. All windows in the vacuum system including the $CaF_2$ window were cleaned with acetone between subsequent experiments. Simply warming the $CaF_2$ window for removal of the matrix without washing with acetone, and recooling the window for another deposition, resulted invariably in a cloudy matrix. The cryostat shroud O-rings were cleaned and regreased with Apiezon-$N^R$ vacuum grease.

The tantalum cell was then mounted by tantalum straps and copper screws to the water-cooled copper electrodes in the furnace ensuring that the cell orifice was aligned with the collimating hole in the water-cooled heat shield and the $CaF_2$ window. This alignment was checked by sighting the tantalum cell through the $CaF_2$ window into the furnace.

Rough pumping of the furnace was carried out for a number of minutes by opening the bypass line valve to isolate the diffusion pump and liquid nitrogen trap. Rough pumping was continued until the system pressure dropped below 200 microns as shown on the thermocouple gauge. The high pressure port valve of the diffusion pump was then opened, the bypass line valve was closed, and the CVC gate valve was gradually opened, making certain that the thermocouple gauge pressure on the high pressure side of the diffusion pump did not exceed 200 microns. With the diffusion pump turned on and the gate valve fully open, the system was pumped to below $2 \times 10^{-5}$ torr as monitored by the ionization gauge controller.

After ensuring that the $CaF_2$ window was shielded from the tantalum cell to prevent the formation of mirror-like films on the window and that the water was flowing in all system cooling lines to maintain the integrity of the furnace "O" ring seals, the Knudsen cell was gradually heated to about the deposition temperature making sure that the system pressure was below $2\text{-}4 \times 10^{-5}$ torr. The gradual preheating of the tantalum cell prevented blow-out of the sample material enclosed in the cell, eliminated adsorbed species in the sample, and avoided weakly absorbing matrices. To accomplish this preheating, it took as long as two hours in some cases.

After the preheating was complete, the liquid nitrogen trap was filled and the Displex$^R$ compressor was then turned on. It usually took a period of one hour to cool the $CaF_2$ window to the deposition temperature. To achieve transparent matrices, the sample window was kept at 14 K for the argon matrix and 20 K for the krypton and xenon matrices. After cooling the sample window to the proper temperature, the cryostat was rotated to the deposition position and the matrix gas was deposited for a period of 10 minutes. The flow rates of the matrix gas were about 1-3 mmole/hr. As an initial estimate, the temperature of the Knudsen cell was set at a temperature which was required to produce a vapor pressure of $\sim 1 \times 10^{-3}$ torr for the sample. However, for cluster formation, it was necessary to set the Knudsen cell temperature higher than the deposition temperature. Deposition temperature for each metal is mentioned in the respective sections of the results.

The sample deposition was carried out anywhere from 5 to 120 minutes. The cryostat was then rotated ninety degrees so that a preliminary absorption spectrum could be taken. If necessary, the deposition was continued until the bands of interest showed an absorbance in the range of 0.50 to 0.95 OD.

Both the absorption and MCD spectra were taken at 11 and 20 k. For those spectra which exhibited temperature dependence, they were recorded at 1 °K intervals between 11 °K and the highest temperature allowed by the matrix gas.

After deposition was complete and the sample window positioned in the optical path, alignment of the sample and reference beams was accomplished and the absorption experiment performed. With completion of the absorption studies the spectroscopic apparatus was modified so that the MCD spectrum could be taken. To complete the MCD analysis, the zero-field circular dichroism spectra (i.e., with the electromagnet power supply turned off) and calibration factors had to be obtained. All absorption and MCD spectra were taken with the aid of the computer.

The monochromator was calibrated with a Spectra Physics 4 W argon ion and He-Ne lasers. Scans were always run from high to low wavelength to avoid stepping gear assembly backlash and to ensure maximum photomultiplier tube sensitivity. All MCD spectra were recorded at 0.55 Tesla (1 Tesla = $10^4$ Gauss) as determined by an F. W. Bell Model 640 Gaussmeter. Note that a residual field of ~60 Gauss was measured with the magnet power supply turned off. A plot of MCD intensity vs. the magnetic field is shown in Figure 12. As expected, the MCD intensity is linearly dependent on the magnetic field.

An aqueous solution of $[Co(en)_3]cl$ (d-tartrate), whose absorbance at 4960 Å was near 1 OD as measured by a Cary 17 spectrometer, was used as a standard to calibrate the intensity of absorption and MCD transitions. The procedure was similar to that of Tacon,[50] and the CD spectrum of this solution was measured at 4930 Å under the same conditions in which the MCD spectrum was taken. This complex salt was synthesized according to Broomhead's procedure.[51] McCaffery

FIGURE 12. Plot of MCD intensity vs. magnetic field strength.

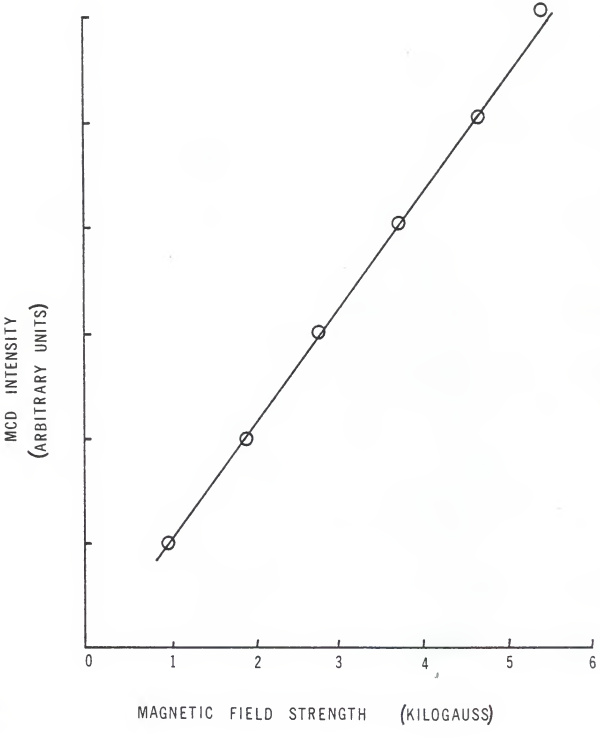
MCD INTENSITY
(ARBITRARY UNITS)
0
1
2
3
4
5
6
MAGNETIC FIELD STRENGTH (KILOGAUSS)

and Mason[52] measured the absorption and CD spectra of this compound and they found the ratio of $\Delta A_{max}/A_{max}$ to be 0.0225. The following equation was used to calibrate the digitized absorption data in optical density units:

$$K_{abs} = \frac{C}{I_{abs}} \tag{41}$$

where

$K_{abs}$ = number of optical density units per digital data unit

$C$ = concentration of the standard solution in optical density

$I_{abs}$ = absorption band intensity of the sample in arbitrary units as stored on the floppy disc

To calibrate the digitized MCD data in optical density units, the following equation was employed:

$$K_{MCD} = 0.0225 \left(\frac{C}{I_{MCD}}\right)\left(\frac{f_{sam}}{f_{std}}\right) \tag{42}$$

where

$K_{MCD}$ = number of optical density units per digitized data unit

$C$ = concentration of the standard solution in optical density

$I_{MCD}$ = MCD band intensity of the sample in arbitrary units as stored on the floppy disc

$f_{sam}$ = lock-in amplifier sensitivity for the sample

$f_{std}$ = lock-in amplifier sensitivity for the standard solution.

An aqueous solution of $K_3$ [Fe(CN)$_6$], whose MCD sign for the band centered at 4250 Å was positive,[33] was used to cross check the sign of the MCD spectra.

# CHAPTER V

# IRON IN THE RARE GAS MATRICES

This chapter is concerned with the absorption and MCD spectra of iron atoms and/or clusters isolated in argon, krypton and xenon matrices. Assignments for all optical transitions of iron atoms in each of these matrices as well as the important calculated MCD parameters for the iron atom are presented.

As mentioned in Chapter I, an assumption of the early studies was that the matrix host was "inert" and with the exception of inducing a matrix shift, it was thought to have only a minimal influence on the spectral results. However, recently it has been shown[19,20,53-55] that localized host cage vibrations can play a significant role in the spectroscopy of some embedded species. Furthermore, other studies[4,56-58] have indicated that low temperature chemical or photochemical activity involving the guest and the matrix host may occur. Several interesting studies on the photolytically-assisted insertion of iron atoms into the C—H bond of methane and other hydrocarbons have been published.[56-58] To the present, there have been no systematic studies on products, yields, etc., as a function of excitation energy. The spectra of iron atoms isolated in rare gas matrices have been studied by a number of workers.[59-63] However, no agreement presently exists for the assignments of the optical bands of matrix-isolated iron atoms.[60,61,63-65]

Keune and Lüescher[59] observed three broad absorption bands for iron atoms isolated in a neon matrix. These bands, whose half-widths were of the order of 500 $cm^{-1}$, were centered at 377, 363, and 335 nm and were attributed to certain $4s4p \leftarrow 4s^2$ transitions. The same transitions for gas phase iron atoms[66] occur at 386.1, 372.1, and 344.2 nm.

Mann and Broida[60] carried out extensive absorption measurements on iron atoms isolated in Ar, Kr, Xe, and $N_2$ matrices. In the case of argon matrices, these authors reported 25 bands within the range 26,448-42,290 $cm^{-1}$. They interpreted these bands as components of transitions from the ground state $^5D_4$ to eleven different excited states. In the case of gaseous iron, these excited states lie 25,900-40,257 $cm^{-1}$ above the ground state. These authors also observed that oscillator strengths for the electronic transitions of iron atoms in the matrix were ten to one hundred times weaker than in the gas phase. Although the spectral intensities observed by Mann and Broida were rather weak, they observed the usual matrix splittings to increase from xenon to krypton, with the iron transitions in argon being quite complex and difficult to correlate with the gas phase results. Their spectral assignments required blue shifts of 314 to 1783 $cm^{-1}$ in going from gas phase to argon.

The temperature dependence of two absorption transitions of iron atoms in a krypton matrix was studied by Micklitz and Barrett.[61] The gas-to-matrix shifts for the two absorption lines at 300.4 nm and 296.9 nm amounted to +175 and +165 $cm^{-1}$. By comparing the relative intensities of the fine structure split components within a multiplet to the theoretically predicted values, these authors concluded that the orbital angular momentum L of the iron atom was unquenched. By employing the moment analysis of the absorption band, these authors also showed that the observed band widths were due to interaction with lattice vibrations and that any line broadening which originated from the splittings of the unresolved crystal field was negligible.

Carstens et al.[63] used a hollow cathode sputtering device and cocondensed iron atoms in an argon matrix. Their spectral assignment was made by a correlation of band frequencies and intensities observed in the matrix with those reported for the gas phase.[67] However, due to the spectral complexity, many bands were left unassigned.

By u.v. photolysis of $Fe(CO)_5$, Poliakoff and Turner[65] isolated iron atoms in $N_2$, Ar, and Kr matrices at 20 K. By means of first derivative absorption spectroscopy, these authors showed that it was possible to reduce the effects of light scattering by the matrix. McNab et al.[68] and Barrett and McNab[69] studied Mössbauer effects of $^{57}Fe$ atoms in matrices. Their studies revealed a line which has been attributed to isolated iron atoms. These authors examined the temperature dependence of the line and showed that the spin-lattice relaxation was dominated by the direct phonon process.

More recently, McKenzie et al.[64] and McKenzie and Nixon[70] studied the laser-induced visible and near-infrared fluorescence of iron atoms in argon matrices. Remarkably sharp (half-width: 3-10 $cm^{-1}$) line widths and small gas-to-matrix shifts (maximum: 99 $cm^{-1}$) were observed. It is important to notice that some of the band assignments which were made by these authors violate the usual $\Delta L = 0, \pm 1$ and $\Delta J = 0, \pm 1$ selection rules. This implies that the matrix environment is responsible for a relaxation of these rules.

## Computational Results and Spectral Predictions

The ground term of gaseous Fe atom is $^5D$ (corresponding to the configuration $3d^6\ 4s^2$). The spin-orbit coupling splits this term into five multiplets (quintet). The J=4 multiplet ($^5D_4$) lies lowest with the other members of the quintet, $^5D_3$, $^5D_2$, $^5D_1$, $^5D_o$, lying respectively, 416, 704, 888 and 978 $cm^{-1}$ above it.[66] The value of the spin-orbit constant, $\lambda$, is approximately 100 $cm^{-1}$.

In order to assign the matrix spectrum of iron, it is necessary to address the following question. To what extent does the matrix environment (crystal field, matrix-induced Jahn-Teller effects, etc.) perturb the free atom states? Regardless of the site symmetry, it is expected that the matrix field is small within a given electronic configuration. This is because the rare gas atoms are neutral. However, the matrix field can induce the displacement of the electronic configurations since the symmetry around the atom is no longer spherical.

Using the $|J, M_J>$ basis, a series of calculations of the important absorption and MCD parameters have been carried out by Dr. Robert Pyzalski of our laboratory and the results for $C_o$ and $D_o$ parameters are given in Table 1.

TABLE 1. Calculated MCD Parameters for Atomic Fe Transitions from J = 4 State to J' States.

| J' | 3 | 4 | 5 |
|---|---|---|---|
| $C_0$[a] | 15/54 | 3/54 | -12/54 |
| $D_0$[b] | 1/27 | 1/27 | 1/27 |
| $C_0/D_0$[c] | 15/2 | 3/2 | -6 |

[a]The $C_0$ values are given in units of $|\langle {}^5\Gamma J' \| m \| {}^5D_4 \rangle|^2$.

[b]The $D_0$ values are given in units of $|\langle {}^5\Gamma J' \| m \| {}^5D_4 \rangle|^2$.

[c]Free atom $C_0/D_0$ values have been calculated assuming a ground state g = 1.5 (J=4).

The assumption used in the calculation of the absorption and MCD parameters of interest was that both crystal field and the Jahn-Teller effects are smaller than the spin-orbit coupling by an order of magnitude. This assumption is supported by the studies on matrix-isolated iron by Micklitz and Barrett[61] and McKenzie et al.[64]

The calculated results for $C_0$ and $D_0$ parameters in the $|J, M_J>$ basis show that the positive $C_0$ terms are predicted for transitions to J' = 3 and 4 excited states and negative $C_0$ terms for transitions to J' = 5 excited states (see Table 1). It is worth pointing out that in the $|J, M_J>$ basis the spin-orbit coupling is dominant and the selection rules are $\Delta J = 0, \pm1$, and $\Delta M_J = \pm1$. Therefore, in the $|J, M_J>$ basis, transitions are expected from J" = 4 ground state to any J' = 3, 4 or 5 excited state multiplets.

Although the octahedral matrix field will split the $^5D_4$ ground state into $A_1$, E, $T_1$, and $T_2$ states, the experimental value of the splitting is found to be smaller than the emission linewidth (i.e., the total splitting should be lower than 10 $cm^{-1}$).[64] If the Jahn-Teller effect is active in the ground state, the symmetry around the iron atom will remain the same but the value of the angular momentum will be reduced. Since the g factor which reflects the value of the angular momentum is directly proportional to $C_0/D_0$, the experimental values of $C_0/D_0$ terms will be lower than those listed in Table 1. However, such a modification can only occur if the Jahn-Teller Hamiltonian, $H_{J.T.}$, connects different J levels of the ground state. In the case of iron, the spin-orbit coupling is large, thus the matrix elements of $H_{J.T.}$ with the higher spin-orbit level are small as demonstrated by van Vleck,[71] and consequently the Jahn-Teller interaction in the J=4 ground state can be ignored.

Table 2 shows the relative dipole strengths ($D_o$) for atomic iron transitions from $^5D_4$ state to $^5\Gamma^o_{J'}$ excited state. These dipole strengths for transitions to components within an excited multiplet are consistent with the values given previously by Condon and Shortley.[72] They are expressed as functions of the reduced elements $<^5\Gamma'_{J'}||m||^5D>$. Important information on the relative transition probabilities to the J' components of a given Γ' state can be obtained by further reduction of these matrix elements. It is worth noting that the dipole moment operator acts only on the orbital part of the system, thus during the reduction of the matrix elements, the selection rule for the spin part can be held. The preducted dipole strengths to the $^5F_4$ and $^5F_3$ states are one and two orders of magnitude smaller, respectively, than to the $^5F_5$ state. Note that the dipole strength to the $^5D_3$ state is five times smaller than the one to the $^5D_4$ state.

In summary, it is expected that in the absorption spectra transitions between the "even" ground state $^5D_4$ and "odd" excited states with the same spin multiplicity ($^5\Gamma^o_{J'}$, with J' = 3, 4 or 5) are observed.

## Band Moment Analysis

It has been shown that the method of moments is very effective in the evaluation of MCD data.[46] As mentioned in Chapter II, the method of moments was first introduced by

Table 2. Relative Dipole Strengths for Atomic Fe Transitions from $^5D_4$ State to $^5\Gamma^\circ_J$, Excited State.

| Excited State | $^5P_3$ | $^5D_3$ | $^5D_4$ | $^5F_3$ | $^5F_4$ | $^5F_5$ |
|---|---|---|---|---|---|---|
| $D_\circ^a$ | $\frac{1}{5}$ | $\frac{1}{30}$ | $\frac{1}{6}$ | $\frac{1}{10\text{x}63}$ | $\frac{3}{2\text{x}63}$ | $\frac{11}{63}$ |

[a] The $D_\circ$ values are given in units of $g \times | < {}^5\Gamma \, || m || \, {}^5D > |^2$.

Henry, Schnatterly, and Slichter (HSS).[48] They developed the procedure for extracting valuable information from broad, featureless bands. Osborne and Stephens (OS)[49] applied this method to the F centers in alkali halides and they derived the moment expressions of interest for the $^2P \leftarrow {}^2S$ transition. These expressions have been used to extract the Cu excited state spin-orbit coupling constant and the contribution to the bandwidth from totally symmetric and nontotally symmetric vibrations of the Ar lattice cage.[19]

The ratio of the zeroth MCD moment to the zeroth absorption moment for iron atoms is given by[46]

$$\frac{<\Delta A>_\circ}{<A>_\circ} = \left(\frac{B_\circ}{D_\circ} + \frac{C_\circ/D_\circ}{kT}\right) \beta H_z$$

where $\beta$ is the Bohr magneton and $H_z$ is the magnetic field strength along the z axis (5500 Gauss).

Figure 13 shows the absorption and MCD spectra of Fe/Kr from which the parameter $C_\circ/D_\circ$ may be obtained. Temperature dependence of the Fe atom $C_\circ$ term in a Kr matrix is shown in Figure 14 (the intensity decreases with increasing temperature). By carrying out a moment analysis on the entire band, useful MCD parameters as well as information on the dipole strengths can be obtained. The Fe/Kr band at 333.5 nm is well isolated, has a positively-signed $C_\circ$ term and correlates well with $z^5P_3°$ state in the gas phase. In order to extract the experimental value of the $C_\circ/D_\circ$ term, a moment analysis of the band located at 333.5 nm was carried out.

Figure 15 shows a plot of the $\frac{<\Delta A>_\circ}{<A>_\circ}$ versus reciprocal temperature for the $^5P_3 \leftarrow {}^5D_4$ transition of krypton matrix-

FIGURE 13. Absorption (top) and MCD (bottom) spectra of iron atoms in a krypton matrix at 14 K (after photolysis at 320 nm for about twelve hours).

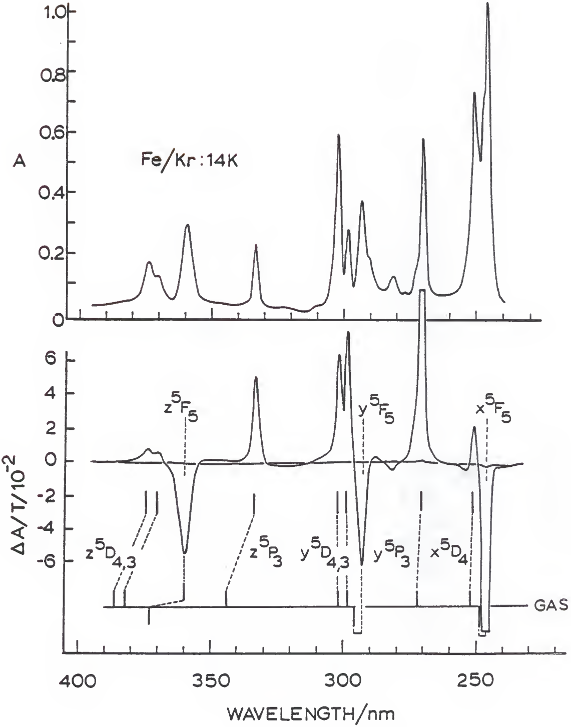
1.0
0.8
0.6
A
0.4
0.2
0
Fe/Kr:14K
6
4
2
0
-2
-4
-6
ΔA/T/10^-2
z^5F_5
y^5F_5
x^5F_5
z^5D_4,3
z^5P_3
y^5D_4,3
y^5P_3
x^5D_4
GAS
400
350
300
250
WAVELENGTH/nm

FIGURE 14. Temperature dependence of the Fe atom $C_0$ term in a krypton matrix. The intensity decreases with increased temperature.

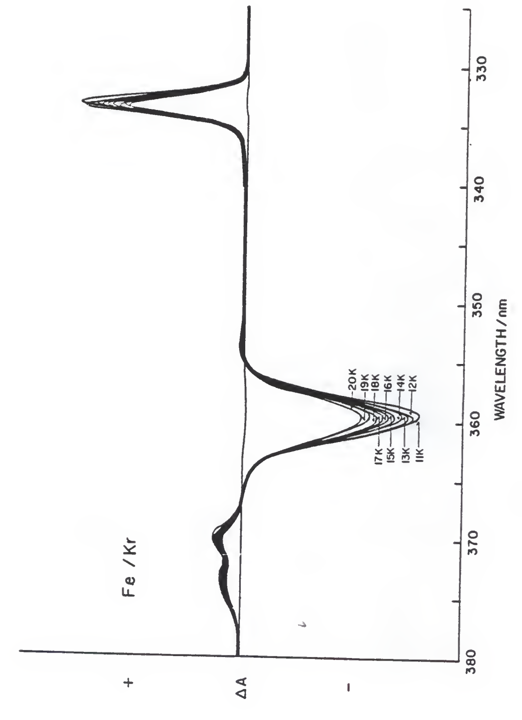
Fe / Kr
+
ΔA
-
380
370
360
350
340
330
WAVELENGTH / nm
20K
19K
18K
16K
14K
12K
17K
15K
13K
11K

FIGURE 15. Experimental plot of $\langle \Delta A \rangle_o / \langle A \rangle_o$ vs. reciprocal temperature for hrypton matrix-isolated Fe atom band at ~335 nm.

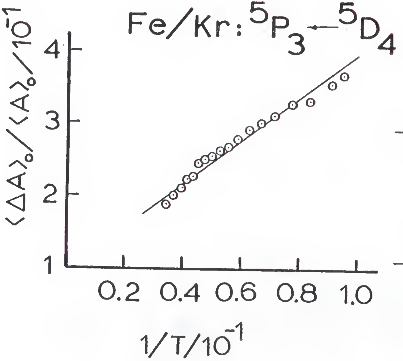

| | $\mathcal{C}_0/\mathcal{D}_0$ |
|---|---|
| expt. | 8.2 ±0.8 |
| theory | 7.5 |

isolated iron atoms. The plot is a straight line and the parameter $C_o/D_o$ is obtained from the slope of this line to be 8.2 ± 0.8 which is within experimental error in good agreement with the theoretically predicted value of 7.5 (see Table 1). The error is mainly due to the uncertainties in the baseline of the absorption spectra. The result confirms the assumption used in the theoretical calculations that both crystal field and the Jahn-Teller effects have small influences on the spectral results. The agreement between the theoretical and the experimental results indicates that there is no reduction of the angular momentum value in the ground state showing that the Jahn-Teller effect, if present, can be ignored. Although the zeroth order moment gives no information on the excited state, however, no splitting is observed leading to the conclusion that the Jahn-Teller effect is small if at all present in this state also.

The experimental plot of the $\frac{\langle \Delta A \rangle_o}{\langle A \rangle_o}$ versus $\frac{1}{T}$ for the $^5F_5 \leftarrow {}^5D_4$ transition of iron atom in a krypton matrix is shown in Figure 16. The value of $C_o/D_o$ obtained from the slope of this line is -8.1. This value is probably too large compared to the theoretically predicted value of -6.0. The difference between the experimental and theoretical values of $C_o/D_o$ can be rationalized as follows: since the baseline in absorption is not as straight in the $^5F_5 \leftarrow {}^5D_4$ band as in the more well-resolved $^5P_3$ band, $\langle A \rangle_o$ was probably estimated too small. As a result, the ratio, $\frac{\langle \Delta A \rangle_o}{\langle A \rangle_o}$, and consequently the slope of the line would be too large. Thus, the increased slope would increase the value of $C_o/D_o$.

FIGURE 16. Experimental plot of $<\Delta A>_o/<A>_o$ vs. reciprocal temperature for krypton matrix-isolated Fe atom band at ~359 nm.

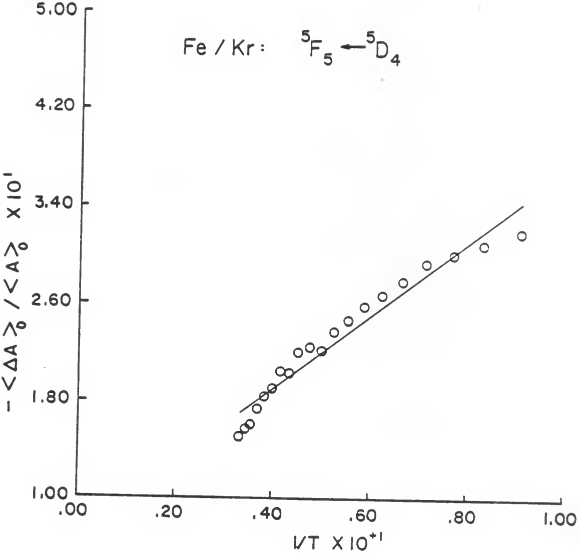
Fe / Kr: $^5F_5 \leftarrow {}^5D_4$
5.00
4.20
3.40
2.60
1.80
1.00
$-\langle\Delta A\rangle_0 / \langle A\rangle_0 \times 10^1$
.00
.20
.40
.60
.80
1.00
$1/T \times 10^{+1}$

## Experimental Procedure

The experimental procedure essentially followed that outlined in Chapter IV. The Knudsen cells employed were tantalum cylinders (wall thickness = 0.017") with tantalum end caps. Aluminum oxide cells were used as liners to prevent any chemical reactions between iron and tantalum at high temperatures. The Fe atom sample was produced by resistance heating iron powder (Spex) contained in a tantalum cell to a temperature of ~1400 C. The effusive iron beam was cocondensed with the isolant noble gas (Matheson, research grade) on a $CaF_2$ window held at 14 K by a closed cycle helium cryostat (Displex). Deposition times of 45 minutes were generally sufficient to produce good matrices.

Calibration for the moment results was done using both the standard, (+) camphorsulfonic acid, whose molecular ellipticity, $[\theta] = 0.201$ at 290 nm,[73] and the standard, $[Co(en)_3]Cl$. (d-tartrate), for which $\varepsilon_{max}$ (469 nm) = 84 $l\ cm^{-1}\ mole^{-1}$ and $\Delta\varepsilon$ (428 nm) = +0.166 $l\ cm^{-1}\ mole^{-1}$.[52] Since a temperature-dependence of the MCD bands was observed, spectra were taken at intervals of 1 K between 12-30 K.

## Results and Discussion

Figures 13, 17 and 18 show the absorption and MCD spectra of iron atoms isolated in krypton, argon and xenon matrices, respectively. The assignments of the observed bands are given in Tables 3, 4 and 5, where comparison to gas-phase results are made. The spin and orbitally allowed transition

FIGURE 17. Absorption (top) and MCD (bottom) spectra of iron atoms in an argon matrix at 14 K.

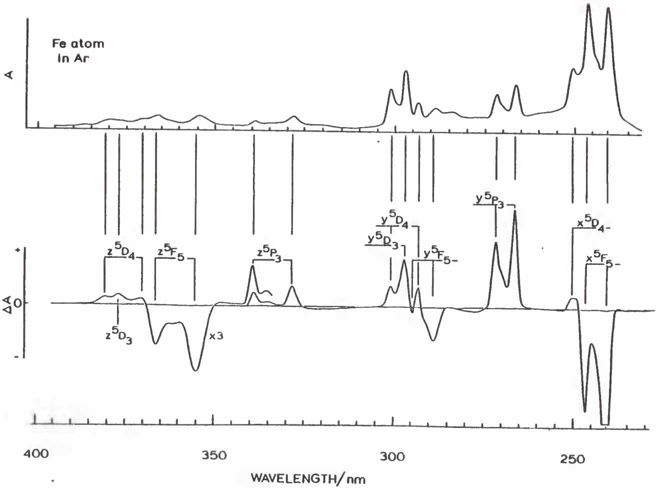
Fe atom
In Ar
A
ΔA
+
0
-
$z^5D_4$
$z^5D_3$
$z^5F_5$
x3
$z^5P_3$
$y^5D_4$
$y^5D_3$
$y^5F_5$-
$y^5P_3$
$x^5D_4$-
$x^5F_5$-
400
350
300
250
WAVELENGTH/nm

FIGURE 18. MCD spectrum of iron atoms in a xenon matrix at 18 K.

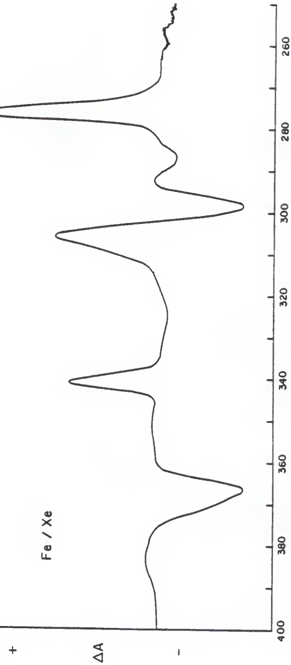
Fe / Xe
ΔA
+
-
400
380
360
340
320
300
280
260
WAVELENGTH / nm

TABLE 3. MCD Band Positions and Assignments for Fe Atoms Isolated in a Krypton Matrix

| Assignment | MCD sign | $\lambda^{Kr}$/nm | $\bar{\nu}^{Kr}$/cm$^{-1}$ | $\bar{\nu}^{GAS}$/cm$^{-1}$ | $\Delta\bar{\nu}$/cm$^{-1}$ |
|---|---|---|---|---|---|
| $z^5D_4$ | + | 374.0 | 26730 | 25900 | 830 |
| $z^5D_3$ | + | 370.0 | 27019 | 26140 | 879 |
| $z^5F_5$ | − | 359.6 | 27801 | 26875 | 926 |
| $z^5F_4$ | + | 353.5 | 28280 | 27167 | 1113 |
| $Fe_x$ | + | ~350.0 | 28560 | | |
| $z^5P_3$ | + | 335.5 | 29976 | 29056 | 920 |
| $Fe_x$ | − | 322.0 | 31028 | | |
| $y^5D_4$ | + | 302.0 | 33103 | 33096 | 7 |
| $y^5D_3$ | + | 298.3 | 33514 | 33507 | 7 |
| $y^5F_5$ | − | 293.8 | 34027 | 33695 | 332 |
| $y^5F_4$ | + | 290.5 | 34413 | 34040 | 373 |
| $y^5F_3$ | + | 288.0 | 34712 | 34329 | 383 |
| $y^5G_5$ or $Fe_x$ | − | 281.5 | 35514 | | |
| $y^5P_3$ | + | 270.5 | 36958 | 36767 | 191 |
| $x^5D_4$ | + | 251.0 | 39829 | 39626 | 203 |
| $x^5F_5$ | − | 246. | 40638 | 40257 | 381 |
| ? | + | 225.6 | 44313 | | |
| ? | − | 218.6 | 45731 | | |

TABLE 4. MCD Band Positions and Assignments for Fe Atoms Isolated in an Argon Matrix

| Assignment[a] | MCD sign | $\lambda^{Ar}$/nm | $\bar{\nu}^{Ar}$/cm$^{-1}$ | $\bar{\nu}^{GAS}$/cm$^{-1}$ | $\Delta\bar{\nu}$/cm$^{-1}$ |
|---|---|---|---|---|---|
| $z^5D_4$ | + | 380.0 | 26308 | 25900 | 408 |
| $z^5D_3$ | + | 376.0 | 26588 | 26140 | 448 |
| $z'^5D_4$ | + | 369.7 | 27041 | 25900 | 1141 |
| $z^5D_5$ | − | 365.5 | 27352 | 26875 | 447 |
| * | − | 360.5 | 27731 | | |
| $z'^5F_5$ | − | 354.0 | 28241 | 26875 | 1366 |
| * | | 347.5 | 28769 | | |
| $z^5P_3$ | + | 338.5 | 29534 | 29056 | 478 |
| * | | 334.5 | 29887 | | |
| $z'^5P_3$ | + | 327.8 | 30498 | 29056 | 1442 |
| * | | 319.0 | 31339 | | |
| $y^5D_4$ | + | 300.5 | 33268 | 33096 | 172 |
| $y^5D_3$ | + | 296.7 | 33694 | 33507 | 187 |
| $y^5F_5$ | − | 294.2 | 33981 | 33695 | 286 |
| $y'^5D_4$ | + | 292.6 | 34166 | 33096 | 1070 |
| $y'^5F_5$ | − | 288.3 | 34676 | 33695 | 981 |
| * | | 276.0 | 36221 | | |
| $y^5P_3$ | + | 271.2 | 36862 | 36767 | 95 |
| * | | 269.2 | 37136 | | |
| $y'^5P_3$ | + | 265.9 | 37597 | 36767 | 830 |
| $x^5D_4$ | + | 250.0 | 39988 | 39626 | 362 |

TABLE 4-continued.

| Assignment[a] | MCD sign | $\lambda^{Ar}$/nm | $\bar{\nu}^{Ar}$/cm$^{-1}$ | $\bar{\nu}^{GAS}$/cm$^{-1}$ | $\Delta\bar{\nu}$/cm$^{-1}$ |
|---|---|---|---|---|---|
| * | | 248.5 | 40229 | | |
| $x^5F_5$ | - | 246.0 | 40639 | 40257 | 381 |
| * | | 242.5 | 41225 | | |
| $x'^5F_5$ | - | 240.5 | 41567 | 40257 | 1310 |

[a] Bands marked *, assigned to a 3rd site, may be deleted by annealing or photolysis (see text).

TABLE 5. MCD Band Positions and Assignments for Fe Atoms Isolated in a Xenon Matrix

| Assignment | MCD sign | $\lambda^{Xe}$/nm | $\bar{\nu}^{Xe}$/cm$^{-1}$ | $\bar{\nu}^{GAS}$/cm$^{-1}$ | $\bar{\nu}$/cm$^{-1}$ |
|---|---|---|---|---|---|
| $z^5D_4$ | + | 383.0 | 26103 | 25900 | 203 |
| $z^5D_3$ | + | 378.0 (sh) | 26448 | 26140 | 308 |
| $z^5F_5$ | − | 366.1 | 27315 | 26875 | 440 |
| $Fe_x$ | + | ~351 | 28482 | -- | -- |
| $z^5P_3$ | + | 340.5 | 29360 | 29056 | 304 |
| $Fe_x$ | − | 325.0 | 30760 | -- | -- |
| $y^5D_4$ | + | 310.0 | 32249 | 33096 | -847 |
| $y^5D_3$ | + | 305.6 | 32713 | 33507 | -794 |
| $y^5F_5$ | − | 298.3 | 33514 | 33695 | -181 |
| ? | + | 292.0 | 34237 | -- | -- |
| $Fe_x$ | − | 286.7 | 34869 | -- | -- |
| $y^5P_3$ | + | 276.1 | 36208 | 36767 | -559 |

a $^5P_3 \leftarrow {}^5D_4$ is seen neither in Ar, Kr nor in Xe matrices. Although the bandwidths of the Fe/Xe spectra are considerably broader and less well resolved than the bandwidths of Fe/Kr, their appearances are similar.

Photolysis of the matrix-isolated iron in krypton matrix at $\lambda = 320$ nm with the matrix temperature set at 22 K for a period of about 12 hours caused removal of the $Fe_x$ cluster bands (see Figures 19 and 13). These two broad bands are located in the spectral range of 330-310 nm and 355-340 nm. Removal of these cluster bands did not change the intensity of the atomic bands. At present, the mechanism of this photolysis is not clear and additional studies need to be done in the future.

### Fe/Kr

The MCD spectrum of iron in krypton matrix shows both positively- and negatively-signed bands. These bands have been shown by their temperature dependence to be C terms (i.e. their intensities decrease with increased temperature). Using the predictions described in the previous section and the assignments of gaseous iron bands tabulated by Moore,[66] the assignments of the observed bands are straightforward. The positions of the gas phase transitions have been shown by vertical markers and each marker multiplied by the sign of the predicted C term (see Figure 13). Those transitions which are above the line are predicted to be positive and those which are below the line negative. It can be seen that a good correlation between the predicted and observed MCD bands exists.

FIGURE 19. Absorption (top) and MCD (bottom) spectra of iron atoms in a krypton matrix at 14 K (before photolysis at 320 nm for about twelve hours).

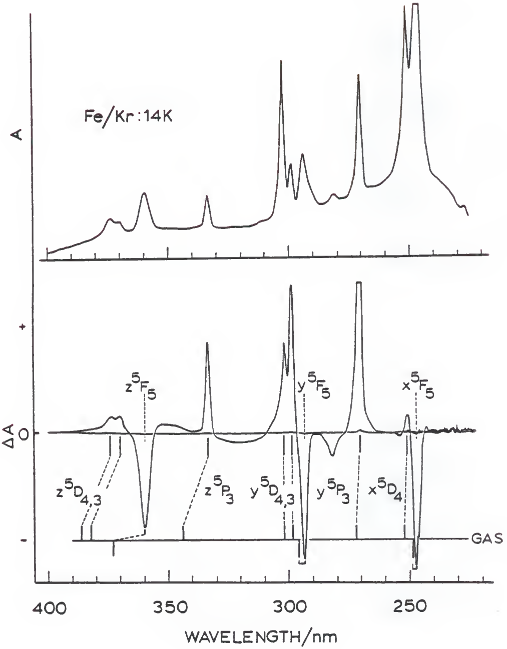
Fe/Kr:14K
A
ΔA
+
0
-
$z^5F_5$
$y^5F_5$
$x^5F_5$
$z^5D_{4,3}$
$z^5P_3$
$y^5D_{4,3}$
$y^5P_3$
$x^5D_4$
GAS
400
350
300
250
WAVELENGTH/nm

The band at 333.5 nm (positively-signed $C_0$ term) is well isolated in the spectra and is well correlated with the $^5P^\circ_3$ state in the gas phase. The relative amplitude of $^5D^\circ_4$ and $^5D^\circ_3$ transitions in absorption together with the $C_0/D_0$ values (see Table 1), confirm the assignments without ambiguity. The $^5F^\circ_{4,3} \leftarrow {}^5D_4$ transitions are not seen in the absorption spectra. The relative dipole strengths for these transitions are, respectively, one or two orders of magnitude smaller than $^5F^\circ_5 \leftarrow {}^5D_4$ transition. However, their positively-signed MCD term can be seen on the high energy side of $z^5F^\circ_5$ and $y^5F^\circ_5$ negative bands.

Only one band (at 282 nm) cannot be assigned to an allowed Fe atom transition. Its absorption intensity is small and the corresponding MCD is negative with a value of $C_0/D_0 \cong -2.5$. There are two possibilities to assign this band. First, it can be assigned to the $z^5G^\circ_5 \leftarrow {}^5D_4$ transition which is spin allowed but orbitally forbidden. Spin-orbit coupling to the $y^5F^\circ_5$ state may make the transition allowed thus giving rise to a weak absorption band with a strong negative MCD signal. Second, it can be assigned to an $Fe_x$ cluster (vide-infra).

The gas-to-matrix shifts for the low energy bands (all due to transitions to states which correspond to the configuration $3d^6$ 4s 4p) are practically constant (~880 $cm^{-1}$) whereas for the upper bands the shifts are considerably less (these bands are due to transitions from configurations differing by more than one electron jump).

From the assignments of the Fe atoms isolated in Kr matrices, three major conclusions can be drawn. First, the matrices are best described using free atom terminology. Second, the spin-orbit coupling is the dominant perturbation on the LS terms and it governs the selection rules. And, third, in the case of iron atoms, the influence of the matrix environment is minimal. As a matter of fact, there is no evidence from the MCD spectrum that the free atom terms are significantly split (i.e., greater than the optical bandwidths). This implies that neither crystal field effects nor matrix-induced Jahn-Teller effects are important in the iron atom system.

### Fe/Ar

The spectrum of iron atoms in argon matrices (cf. Figure 17) is substantially more complex than in krypton. However, using the MCD spectrum of iron atoms in krypton matrices (see Figure 13) makes the assignment of the iron bands relatively simple. Having the assignments for the observed bands of iron atoms in Kr matrices, it is not difficult to see that the results of iron atoms in Ar matrices arise from a doubling of all lines. Although this doubling has been noticed previously,[60,61,63] an exact band assignment has been difficult because of the overlapping of the absorption bands. Note that in some cases ($z^5D_3$, $y^5D_3$, $x^5D_4$) only one partner of a weak, positive band pair has been assigned. In such cases, a strong negative band ($^5F_5$) to higher energy overlaps the second partner and causes its disappearance.

Several of the stronger pairs have another component (usually a shoulder) between them (i.e., at 360.5 nm, 347.5 nm, 334.5 nm and others marked in Table 4). By annealing the matrix at 25 K and/or photolyzing it at 320 nm for twelve hours, these bands can be deleted. Two major (and one minor) sets of bands are associated with different sites in the latice. Annealing and different deposition conditions have given rise to different relative intensities among the bands of the two (three) sets which clearly indicate that different sites are present. Therefore, there are two major, stable sites in the argon matrix while there is only one in krypton and xenon matrices. Temperature dependence of the MCD bands of Fe/Ar is shown in Figure 20. The intensities of the bands decrease with increased temperature (i.e., C term).

Figure 21 shows the two MCD spectra of Fe/Ar and Fe/Kr which are superimposed. It is clear that the two major sets of bands in Ar are almost symmetrically displaced with respect to their positions in Kr. The minor set for both matrices is almost identical. Comparing these spectra provides clear evidence that the symmetry of the wavefunctions deduced from LS coupling is not changed by the nonspherical environment about the atom. Although the MCD is the same for the three sites, the configurations can be displaced by this effect. For the same reason, it is understandable that all terms of a given excited configuration are shifted by the same quantity with respect to their energy in the gas phase.

FIGURE 20. Temperature dependence of the Fe atom $C_0$ term in an argon matrix. The intensity decreases with increased temperature.

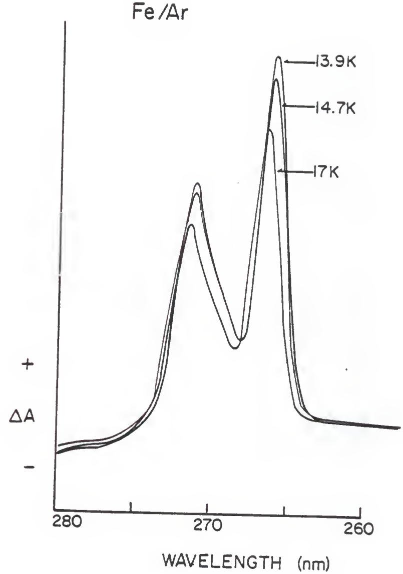
Fe /Ar
13.9K
14.7K
17K
+
ΔA
−
280
270
260
WAVELENGTH (nm)

FIGURE 21. Superposition of a small portion of the MCD spectra of Fe/Ar and Fe/Kr. The energy separations are (in order of decreasing wavelength) 420 $cm^{-1}$, 472 $cm^{-1}$, 488 $cm^{-1}$, and 481 $cm^{-1}$.

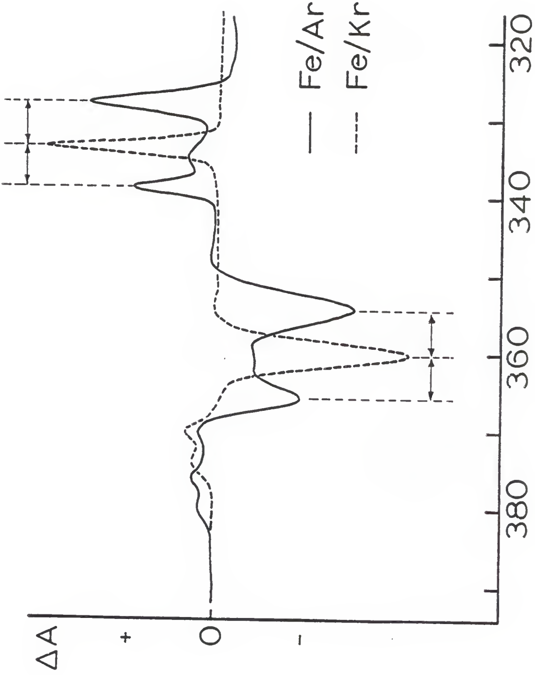
ΔA
+
0
-
380
360
340
320
WAVELENGTH/nm
Fe/Ar
Fe/Kr

## $Fe_x$ Cluster Bands

Figure 22 shows the MCD spectrum of three different Fe/Ar matrices formed under different deposition conditions. Although their appearance is quite different, there are many common features. These atomic features which are due to Fe atoms in the two stable Ar sites are sharper in the top spectrum while they are less pronounced in the middle and bottom spectra (see Figure 22). The middle and bottom spectra are due to the superposition of atomic iron bands and iron cluster bands (called $Fe_x$ clusters). In examining Figure 22, it is obvious that the relative proportion of $Fe_x$ to Fe species decreases from the top to the bottom panels. Several pieces of (negative) evidence, lead us to conclude that the broader bands in this spectral range are due to a $Fe_x$ species. First, it is unlikely that the observed intensity was altered by an impurity absorption. The iron powder (Spex) used contains only 10 ppm total metal impurities (i.e., 99.999% pure). Second, absorption due to an iron oxide (e.g., FeO or $FeO_2$) is also considered unlikely. Contamination from air leaks is improbable since the vacuum in the system during degassing and deposition was usually $10^{-5}$ - $10^{-6}$ torr. And, third, condensing ozone with the iron and argon and photolyzing gives rise to bands similar to those in Figure 22, implying that either no iron oxides were formed or, if formed, do not absorb in the spectral region of interest (400 - 220 nm).

In the above experiments neither absorption bands nor MCD bands are detected in the 600 - 400 nm range where $Fe_2$

FIGURE 22. MCD Spectra showing Fe atomic lines and $Fe_x$ cluster bands in an argon matrix.

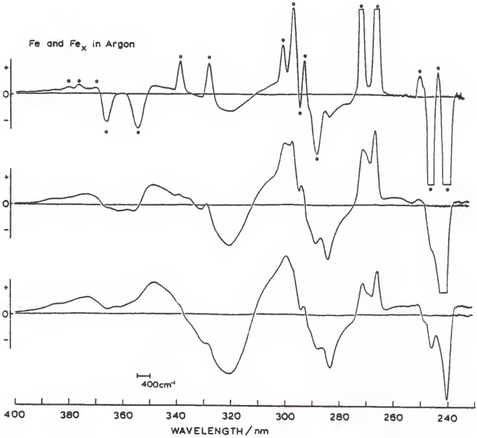
Fe and Fe$_x$ in Argon
ΔA
+
0
-
400cm⁻¹
400
380
360
340
320
300
280
260
240
WAVELENGTH / nm

is reported[74-76] to absorb. Thus, it is concluded from this that the observed species is composed solely of Fe and the value of X is $\geq 3$.

With the present data it is not possible to specify the size of the $Fe_x$ cluster. However, from the temperature dependence of the cluster MCD bands, it is clear that the absorbing species is paramagnetic. Furthermore, it can be deduced that the ground state of the cluster is spin and orbitally degenerate. In order to reach to this conclusion, the following arguments are used.

It is known that MCD transitions between a spin-degenerate, orbitally-nondegenerate ground state and a spin- and orbitally-degenerate excited state will give rise to C terms of alternating sign (i.e., the C terms to the different spin-orbit multiplets of an excited electronic state alternate in sign). Assuming that the spin-orbit components of the excited state of a cluster will be split by the same order of magnitude as the spin-orbit multiplet separations of atomic iron (~400 $cm^{-1}$, see Figure 22), then the bandwidths of the observed cluster bands in Figure 22 are greater than their multiplet splitting. In fact, no alternation in sign is observed for these bands (i.e., 400 $cm^{-1}$). Therefore, the positively- and negatively-signed bands observed in this study are due to transitions to different electronic states, not transitions to different spin-orbit components of one electronic state. It is also concluded that the ground electronic state of the $Fe_x$ species which is responsible for these bands, is both orbitally and spin degenerate.

# CHAPTER VI

# MANGANESE IN THE RARE GAS MATRICES

The absorption and MCD spectra obtained for manganese atoms and/or clusters isolated in argon, krypton, and xenon matrices are presented in this chapter. Assignments for the optical transitions of manganese species in each of these matrices as well as moment analysis for one of the $^6P \leftarrow {}^6S$ transitions of manganese atoms isolated in a krypton matrix are discussed. The existence of the $Mn_2$ molecule which is confirmed by an unusual transition in argon matrices is also discussed. The temperature variation of the absorption and MCD intensity in the range 13-27K demonstrate that the $Mn_2$ molecule is antiferromagnetic and allows a precise determination of its ground-state exchange energy: $J = -10.3 \pm 0.6$ cm$^{-1}$ (*vide infra*).

Manganese was one of the first metals to be studied employing matrix-isolation techniques. The optical absorption spectra of manganese atoms in rare gas matrices have been previously observed by Schnepp,[77] Lee and Gutmacher,[78] and Mann and Broida.[60]

The initial matrix work by Schnepp resulted in the identification of the two main absorption bands around 400 nm and 280 nm to transitions between the atomic ground $^6S$ state and two $^6P$ excited states, whose configurations are $3d^5\ 4s\ (^7S)\ 4p$ and $3d^5\ 4s\ (^5S)\ 4p$. In the gas phase, these transitions consist of two groups of triplets. Schnepp's matrix spectrum showed two groups of five lines each, which he attributed to manganese atoms in different lattice sites. He proposed that the subcomponents were due to the removal of degeneracy in the asymmetric environment of the lattice site. A comparison between the atomic and matrix intensities of transition metal atoms was first made by Schnepp and applied to Mn.[77] Schnepp estimated the ratio of the intensities of these two absorption bands in the matrix and compared the value he found, 4.0 ± 0.3, to the ratio of the intensities of the gaseous atomic lines, 3.7. He deduced from the matrix shift and the line width that the crystal field is weaker than in typical ionic crystals by two orders of magnitude. The splitting energy observed was of the order of 300 $cm^{-1}$.

Lee and Gutmacher[78] investigated the effects of annealing on the absorption spectrum of manganese atoms in solid argon. By comparing the spectra before and after annealing, these authors observed some interesting differences, primarily in the absorption spectrum near 400 nm. After annealing the matrix, all components of the $z^6P° \leftarrow {}^6S$ transition were appreciably sharpened. In addition, a broad component (near 280 nm) and a weak single line (near 310 nm) corresponding to the $z^4P° \leftarrow {}^6S$ transition appeared in the absorption spectrum. Because of the large number of components in each group, these authors invoked multiple trapping sites. However, they did not attempt a further analysis of the lines.

Mann and Broida[60] studied the absorption spectra of manganese atoms in argon matrices at 4.2K. These authors reported the values of average width and matrix shift in argon as 300 and 490 cm$^{-1}$, respectively, for the lower triplet ($z^6P°_{3/2,\ 5/2,\ 7/2} \leftarrow {}^6S_{5/2}$) and 200 and 300 cm$^{-1}$ for the upper triplet ($y^6P°_{3/2,\ 5/2,\ 7/2} \leftarrow {}^6S_{5/2}$).

In more concentrated matrices, Klotzbücher and Ozin[79] observed numerous bands in the ultraviolet region and tentatively assigned them to "$Mn_x$" and "$Mn_y$" cluster species, with x and y unspecified. Kant et al.[80] observed the $Mn_2$ molecule mass spectrometrically in the vapor in equilibrium with Mn metal at 1500K. Using high atom concentrations, Devore et al.[74] located a band at 650 nm and assigned it to a transition of the $Mn_2$ molecule.

It is perhaps worth noting that for the more intense bands of the manganese spectrum, the agreement between the various authors is quite good but all reported some weak bands not observed by the others. For the stronger bands, the average differences between reported band maxima is of the order of 50 cm$^{-1}$ whereas for the weaker bands, the differences are larger.

## Experimental Procedure

The Knudsen cells employed in these experiments were tantalum cylinders (wall thickness - 0.015") with tantalum end caps. Following the standard procedure, the cell was loaded with manganese powder (Spex) and was preheated before the deposition. The temperature of the Knudsen cell during preheating was about 900° C. Preheating was continued until the pressure of the system was below 2 x 10$^{-5}$ torr. The crude metal beam was cocondensed with the isolant noble gas

(Matheson, research grade) on a $CaF_2$ window cooled by a close cycle helium cryostat (Displex). Depositions were performed at a Knudsen cell temperature of 950 °C for argon, 1020 °C for krypton, and 980 °C for xenon matrices for a period of one hour. The $CaF_2$ sample window was held at 13 K for Ar deposits, 16 K for Kr deposits and 20 K for Xe deposits (the higher temperatures were used for Kr and Xe depositions reduced scattering of light by the matrix during spectral runs).

Absorption and MCD spectra were run sequentially on the same sample-matrix with the results presented in analog and digital form. A microcomputer (CMD 8032) and dual floppy disc drive were employed to control the experiments (λ drive, sample temperature, photoelastic modulator drive voltage) and manipulate the data (data storage, moment calculations).

Since temperature-dependent MCD spectra were observed, runs were made at several temperatures for Ar, Kr, and Xe matrices. Calibration of the MCD spectra was done using the standard, (+) camphorsulfonic acid (molecular ellipticity $[\theta] = 0.201$ at 290 nm)[73] and a solution of the complex salt $[Co(en)_3]Cl$. (d-tartrate); for which $\varepsilon_{max}$ (489 nm) = 84 $l\ cm^{-1}\ mole^{-1}$ and $\Delta\varepsilon$ (428 nm) = +0.166 $l\ cm^{-1}\ mole^{-1}$.[52]

## Results and Discussion

The ground state of gaseous manganese atom is $^6S_{5/2}$ ($3d^5\ 4s^2$ configuration).[66] The excited configurations $3d^5$ 4s ($a^7S$) 4p and $3d^5$ 4s ($a^5S$) 4p give rise, respectively, to $z^6P$ and $y^6P$ terms, to which transitions from the $^6S$ ground state are allowed. These transitions consist of triplets whose components obey the selection rules $\Delta J = 0, \pm 1$.

The MCD signals corresponding to these two transitions are intense, show a strong temperature dependence, and exhibit a triplet of bands with separations much larger than the gaseous spin-orbit splittings of the $^6P$ states. The value of the gas phase spin-orbit splittings for the $z^6P$ and $y^6P$ are 23 $cm^{-1}$ and 80 $cm^{-1}$, respectively. Spectral changes due to imbedding an atom in a matrix are usually ascribed to "matrix perturbations," which can affect band positions, widths, and intensities. Changes in bandwidth and band splittings, caused by the crystal field,[81] multiple site effects, spin-orbit coupling interactions,[82,83] and Jahn-Teller cage distortions are quite commonly observed but have not yet been completely understood. For the case of manganese atoms isolated in a Kr matrix, an analysis of band moments indicates that an excited state Jahn-Teller interaction is active (vide infra).

After a detailed treatment of Mn/Kr (including a spectral moment analysis for the $z^6P \leftarrow {}^6S$ transition), the results obtained for Mn/Xe and Mn/Ar will be presented. This is followed by the results obtained for $Mn_2$ molecule.

## Mn/Kr

Figure 23 shows the absorption and MCD spectra of manganese species isolated in a krypton matrix. The band assignments are given in Table 6 where comparison to the gas phase results are made. The MCD spectrum shows both positively- and negatively-signed bands which have been shown by their temperature dependence to be C terms.

FIGURE 23. Absorption (top) and MCD (bottom) spectra of manganese species in a krypton matrix at 14 K.

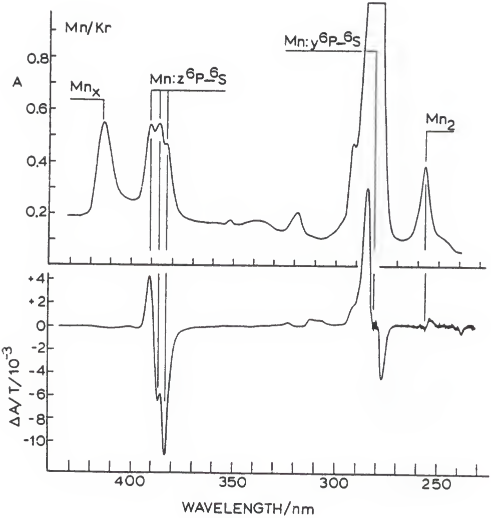
Mn/Kr
A
0.8
0.6
0.4
0.2
$Mn_x$
$Mn: z^6P - ^6S$
$Mn: y^6P - ^6S$
$Mn_2$
+4
+2
0
-2
-4
-6
-8
-10
$\Delta A/T/10^{-3}$
400
350
300
250
WAVELENGTH/nm

TABLE 6. MCD Band Positions, Matrix Shifts and Assignments for Mn Species Isolated in a Krypton Matrix

| Transition | | Gaseous | | Kr Matrix[a] | | | Shift | MCD signs | | Species |
|---|---|---|---|---|---|---|---|---|---|---|
| | J | $\nu$/cm$^{-1}$ | $\Delta\nu$/cm$^{-1}$ | $\lambda$/nm | $\nu$/cm$^{-1}$ | $\Delta\nu$/cm$^{-1}$ | $\Delta\nu = \nu Kr - \nu gas$ | Predicted | Observed | |
| ? | | | | 414.0 | 24148 | | | | N | $Mn_x$ (X=5 ?) |
| | 3/2 | 24779 | | 391.2 | 25555 | | 776 | + | + | |
| $z^6P_J \leftarrow {}^6S$ | 5/2 | 24788 | 9 | 387.0 | 25832 | 277 | 1044 | + | - | Mn |
| | 7/2 | 24802 | 14 | 383.2 | 26089 | 257 | 1287 | - | - | |
| ? | | -- | | 324.0 | 30855 | | -- | ? | + | $Mn_x$ |
| $z^4P_J \leftarrow {}^6S$ | 3/2 | 31076 | | 310.0 | 32249 | | 1173 | + | + | Mn |
| | 3/2 | 35690 | | 292.0 | 34237 | | -1453 | + | + | |
| $y^6P_J \leftarrow {}^6S$ | 5/2 | 35726 | 36 | 284.5 | 35139 | 902 | -587 | + | + | Mn |
| | 7/2 | 35770 | 44 | 278.5 | 35896 | 757 | 126 | - | - | |
| ? | | | | 256.5* | 38975 | | | ? | + | $Mn_x$<br>($Mn_2$ ?) |
| $z^6D \leftarrow {}^6S$<br>or $Mn_x$ | 7/2 | 41933 | | 239.0 | 41828 | | -105 | - | - | Mn or<br>$Mn_x$ |

[a] wavelength marked *, taken from the absorption spectrum. N = no MCD signal.

For one absorption band located at 414 nm no MCD signal has been observed. Since this band does not correlate with the gas phase data it can be assigned to an $Mn_x$ species with the value of x unspecified. It is interesting to speculate that this band belongs to the $Mn_5$ molecule. Baumann et al.[84] have observed such a species in matrix-isolation ESR experiments and have shown that its ground state is spin degenerate (S = 25/2) and orbitally nondegenerate. These authors deduce that the structure is probably a planar five-membered ring ($D_{5h}$). Interestingly, they do not observe any ESR lines attributable to species other than Mn, $Mn_2$ and $Mn_5$ (i.e., no $Mn_3$ or $Mn_4$). If the 414 nm band is attributable to the $Mn_5$ species, the transition takes place between the ground state (probably $^{26}A_1{}'$) and an excited $^{26}A_2{}''$ state. This transition is spin- and orbitally-allowed and therefore would be seen in the absorption spectrum but because of only the spin-degeneracy in the two states is predicted to exhibit a zero MCD signal, as observed.

The band centered at 310 nm (with a positively-signed MCD) is assigned to the resonance transition ($z^4P_{3/2} \leftarrow {}^6S$) at 321.7 nm in the gas phase for a matrix shift of 1173 $cm^{-1}$. This transition is orbitally allowed but spin forbidden. The forbiddenness may be removed via spin-orbit coupling to the $y^6P_{3/2}$ state thus giving rise to the observed small positive MCD signal.

The two groups of triplets $z^6P$ and $y^6P$ are strongly temperature dependent. The lower energy triplet ($z^6P_{3/2,\ 5/2,\ 7/2}$) exhibits positive, negative, and negative MCD bands whereas the higher energy one ($y^6P_{3/2,\ 5/2,\ 7/2}$) shows positive, positive (only observed in Mn/Kr), and negative MCD signals. Schnepp[77] has pointed out that the observation of the triplet is understandable in terms of an asymmetric crystal field perturbation on the trapped atom in the excited $^6P$ state, but we will show that the spin-orbit interaction and the Jahn-Teller effect is responsible for the triplet of bands. It is important to note that the observed MCD band for the J = 5/2 component of the lower energy triplet has a negative sign whereas the predicted sign for the same component is positive. The same combination is also seen in the MCD spectra of manganese in argon and xenon matrices. The experimental evidence indicates that the multiple site effects are not present in the case of Mn/Kr matrices. Since the band splittings (534 $cm^{-1}$) are much larger than the spin-orbit splittings (23 $cm^{-1}$) of the $z^6P$ state, an excited state dynamical distortion resulting from nontotally symmetric matrix cage vibrations (i.e., Jahn-Teller effects) are indicated (see later for discussion).

Figure 24 and 25 show the temperature dependence of the manganese atom C term in a krypton matrix for the transitions $z^6P \leftarrow {}^6S$ and $y^6P \leftarrow {}^6S$, respectively. The intensity of the bands decreases with increasing temperature. In the following section an analysis of the band moments for the $z^6P \leftarrow {}^6S$ atomic transition of manganese in a krypton matrix is presented. The theoretical equations used in elucidating the moment results were derived by Dr. Robert Pyzalski of our laboratory.

FIGURE 24. Temperature dependence of the Mn atom bands (~387 nm) in a krypton matrix. The intensity decreases with increased temperature.

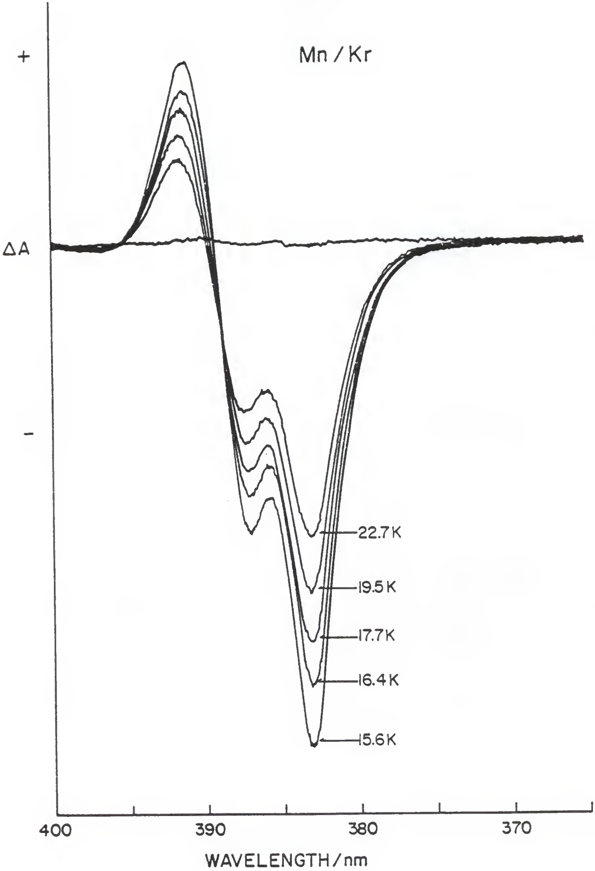
Mn / Kr
+
ΔA
-
22.7 K
19.5 K
17.7 K
16.4 K
15.6 K
400
390
380
370
WAVELENGTH / nm

FIGURE 25. Temperature dependence of the Mn atom bands (~284 nm) in a krypton matrix. The intensity decreases with increased temperature. Note the saturation of the pm tube in the 279.5-282.5 nm range.

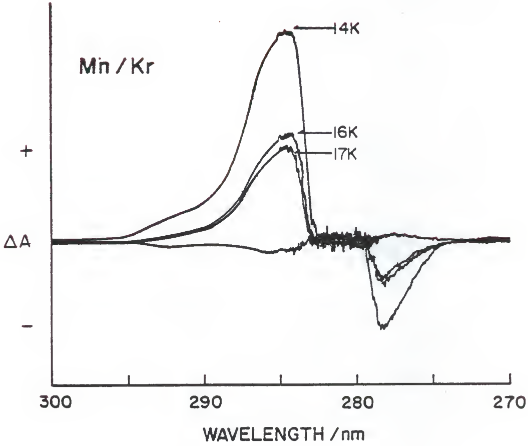
Mn / Kr
14K
16K
17K
+
ΔA
−
300
290
280
270
WAVELENGTH / nm

## Spectral Moment Analysis

The first MCD moment to the zeroth absorption moment for the transition $^6P \leftarrow {^6S}$ of manganese atoms is given by

$$\frac{\langle \Delta A \rangle_1}{\langle A \rangle_0} = -\left(\frac{35}{3}\frac{\Delta}{kT} - 2g_{orb}\right)\beta H \qquad (44)$$

where $\beta$ is the Bohr magneton, H is the magnetic field strength, k is Boltzmann constant, T is the absolute temperature, and $g_{orb}$ is the orbital g factor. $\Delta$ is a parameter which is connected to the spin-orbit splitting by the following equations:

$$\Delta_{7/2,\ 5/2} = 7/2\ \Delta \qquad (45)$$

and

$$\Delta_{5/2,\ 3/2} = 5/2\ \Delta \qquad (46)$$

Figure 26 gives a plot of $\langle \Delta A \rangle_1 / \langle A \rangle_0$ vs. $\frac{1}{T}$ from which the parameters $\Delta$ and $g_{orb}$ may be obtained. The excited state spin-orbit splitting ($6\Delta$) is obtained from the slope:

$$\text{slope} = -\frac{35}{3}\beta H\frac{\Delta}{k} \qquad (47)$$

and the $g_{orb}$ is obtained from the intercept:

$$\text{intercept} = 2g_{orb}\beta H \qquad (48)$$

The $g_{orb}$ quantity is very sensitive to any random or systematic error in the plotted moment or temperature values since it comes from the extrapolation to infinite temperature ($T^{-1} \rightarrow 0$) of data gathered over a relatively small temperature range (15.6 - 25 K). Theoretically $g_{orb} = 1$, but because of the large uncertainty in the experimental result, it is not possible to decide the influence of the matrix environment on this quantity.

FIGURE 26. Experimental plot of $\langle \Delta A \rangle_1 / \langle A \rangle_0$ vs. reciprocal temperature for krypton matrix-isolated Mn atom bands at ~387 nm.

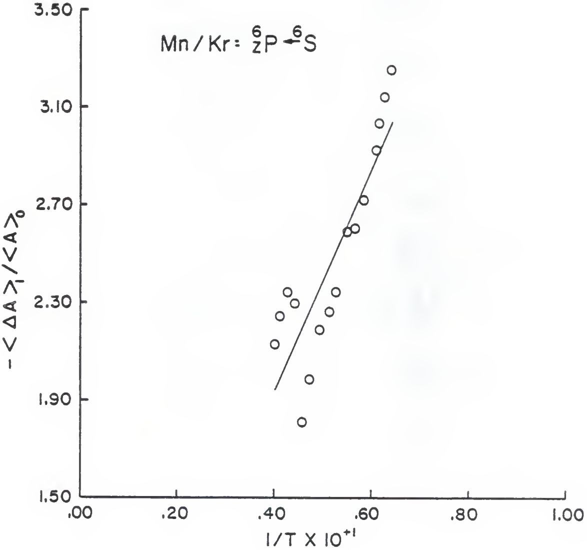
Mn / Kr: $^6_zP \leftarrow {}^6S$
3.50
3.10
2.70
2.30
1.90
1.50
$-\langle \Delta A \rangle_1 / \langle A \rangle_0$
.00
.20
.40
.60
.80
1.00
$1/T \times 10^{+1}$

Alternatively the spin-orbit splitting, $6\Delta$, is obtained from the slope of the linear plot and is therefore relatively insensitive to the errors arising from the small temperature range sampled. Manganese atoms in the gas phase exhibit a 23 $cm^{-1}$ splitting between the $^6P_{3/2}$ and $^6P_{7/2}$ components of the excited state. The matrix value obtained from the experimental plot is 62.7 $cm^{-1}$ for Mn in Kr. The experimental value for $g_{orb}$ is 2.8.

The ratio of the third MCD moment and the second absorption moment to the zeroth absorption moment are given, respectively, by:

$$\frac{\langle\Delta A\rangle_3}{\langle A\rangle_0} = 3\,\frac{\langle\Delta A\rangle_1}{\langle A\rangle_0}\,(\langle E^2\rangle_C + \tfrac{1}{2}\,\langle E^2\rangle_{NC} + \tfrac{35}{12}\,\Delta^2) \tag{49}$$

and

$$\frac{\langle A\rangle_2}{\langle A\rangle_0} = \langle E^2\rangle_C + \langle E^2\rangle_{NC} + \frac{35}{6}\,\Delta^2 \tag{50}$$

where $\langle E^2\rangle_C$ and $\langle E^2\rangle_{NC}$ represent the contributions to the bandwidth (second moment of the absorption) from the cubic and noncubic lattice modes, respectively.

Figure 27 shows a plot of $\langle\Delta A\rangle_3/\langle A\rangle_0$ vs. $\frac{1}{T}$. From the slope of this plot together with equations (49) and (50), the cubic and noncubic contributions can be obtained. The calculated values of the cubic and noncubic contributions are $1.2 \times 10^5$ $cm^{-2}$ and $3.7 \times 10^4$ $cm^{-2}$, respectively. Although the noncubic contribution is smaller by a factor of 10, its contribution to the bandwidth is still considerable. Moreover, it provides unequivocal proof that the nontotally

FIGURE 27. Experimental plot of $<\Delta A>_3/<A>_o$ vs. reciprocal temperature for krypton matrix-isolated Mn atom bands at ~387 nm.

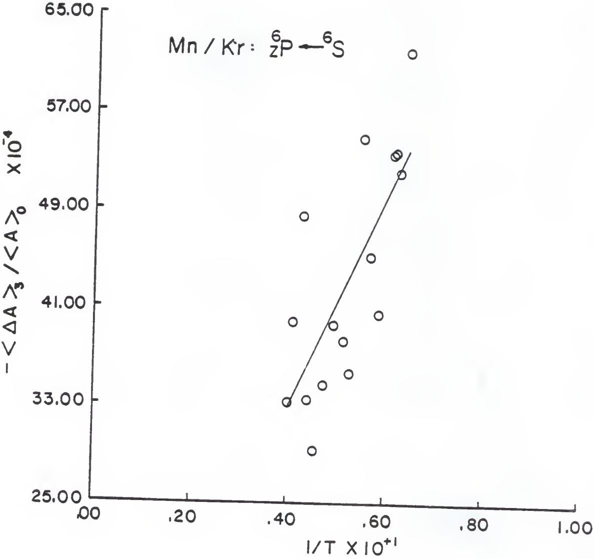
Mn / Kr : $^6_zP \leftarrow {}^6S$
65.00
57.00
49.00
41.00
33.00
25.00
$-\langle \Delta A \rangle_3 / \langle A \rangle_0 \times 10^{-4}$
.00
.20
.40
.60
.80
1.00
$1/T \times 10^{+1}$

symmetric lattice modes required for the Jahn-Teller effect are indeed present and active. Because the third moments do not allow for a separation of the noncubic contributions into $e_g$ or $t_{2g}$ type modes we cannot specify the exact contribution of each symmetry mode to the total bandwidth.

### Mn/Ke

In Figures 28 and 29 the absorption and MCD spectra of manganese species isolated in a xenon matrix are presented. The absorption spectrum of Mn/Xe is similar in appearance to the Mn/Kr spectrum since there is only one type of site present in both matrices. Positively- and negatively-signed MCD bands which are temperature dependent appear in the MCD spectrum. Band assignments and MCD band positions are given in Table 7.

For the $z^6P_{3/2,\ 5/2,\ 7/2}$ triplet centered at 400.2, 396.7 and 393.0 nm, respectively, the predicted MCD signs are positive, positive, and negative whereas the observed MCD signs are positive, negative, and negative. As mentioned before, the sign reversal for the J = 5/2 component is due to the excited state Jahn-Teller interaction.

A very interesting observation was noted in the MCD temperature dependent studies of the $y^6P \leftarrow {}^6S$ transition (see Figure 30). We interpret this observation as arising from the overlap of two Mn bands and one $Mn_2$ band. The two lower energy bands located at 291 nm and 289 nm correspond to the $y^6P_{3/2}$ and $y^6P_{7/2}$ components, respectively ($y^6P_{5/2}$ is not resolved). With increasing temperature (to 30 K) the sign of the lower energy band appears to change from positive to negative.

FIGURE 28. Absorption spectrum of Mn species in a xenon matrix at 14 K.

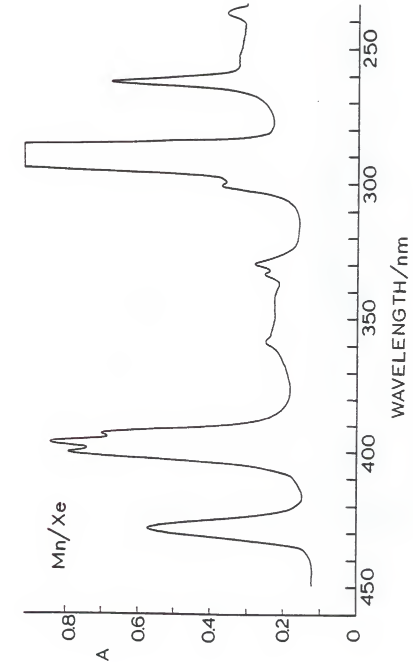
Mn/Xe
A
0
0.2
0.4
0.6
0.8
450
400
350
300
250
WAVELENGTH/nm

FIGURE 29. MCD spectrum of Mn species in a xenon matrix at 14 K.

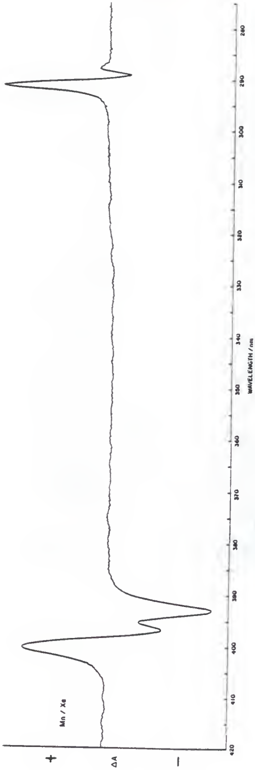
Mn / Xe
+
ΔA
−
420
410
400
390
380
370
360
350
340
330
320
310
300
290
280
WAVELENGTH / nm

TABLE 7. MCD Band Positions, Matrix Shifts and Assignments for Mn Species Isolated in a Xenon Matrix

| Transition | | Gaseous | | Xe Matrix[a] | | | Shift | MCD signs | | Species |
|---|---|---|---|---|---|---|---|---|---|---|
| | J | ν/cm$^{-1}$ | Δν/cm$^{-1}$ | λ/nm | ν/cm$^{-1}$ | Δν/cm$^{-1}$ | Δν = νXe − νgas | Predicted | Observed | |
| ? | | | | 428.0* | 23358 | | | | N | Mn$_x$ (X=5?) |
| $z^6P_J \leftarrow {}^6S$ | 3/2 | 24779 | 9 | 400.2 | 24980 | 277 | 201 | + | + | Mn |
| | 5/2 | 24788 | 14 | 396.7 | 25201 | 257 | 413 | + | − | |
| | 7/2 | 24802 | | 393.0 | 25438 | | 636 | − | − | |
| $y^6P_J \leftarrow {}^6S$ | 3/2 | 35690 | | 291.0 | 34354 | | −1336 | + | + | |
| | 5/2 | -- | | -- | -- | 238 | | + | ? | Mn |
| | 7/2 | 35726 | | 289.0 | 34592 | | −1134 | − | − | Mn |
| S' = 1 ← S = 0 | | 35770 | | 287.6 | 34760 | | −1010 | +(A Term) | + | Mn$_2$ |

[a] wavelength marked *, taken from the absorption spectrum. N = no MCD signal.

FIGURE 30. MCD temperature dependence of Mn species in a xenon matrix.

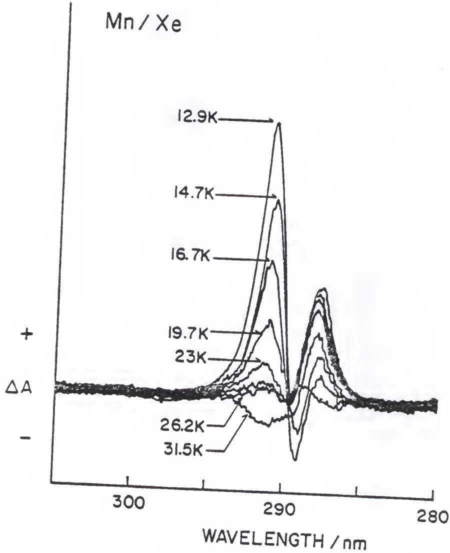
Mn / Xe
12.9K
14.7K
16.7K
19.7K
23K
26.2K
31.5K
+
ΔA
−
300
290
280
WAVELENGTH / nm

We attribute the 287.6 nm band to the S' = 1 ← S = 0 transition of the $Mn_2$ molecule (vide infra) for which a positive A term is expected. The 291 nm band is assigned to the atomic Mn $y^6P \leftarrow {}^6S$ transition which should (and does) show two oppositely-signed C terms (the positive one to lower energy). At low temperatures we expect that the atomic C terms will dominate the spectrum but become less intense with increasing temperature. At the highest temperatures employed (30 K) the major contribution should be from the $Mn_2$ A terms. Thus as temperature rises the lower energy positive C terms decreases in intensity and "permits" the appearance of the negative lobe of the $Mn_2$ A term. Thus the sign of this composite band appears to change.

## Mn/Ar

In Figure 31 is shown the absorption and MCD spectra of manganese species isolated in an argon matrix. The MCD band positions and the assignments of the observed bands are given in Table 8. The MCD spectrum around 400 nm consists mainly of one group of three lines on the long wavelength side and a second group of two lines on the short wavelength side. All of these lines are temperature dependent (C terms). The first group of three lines located at 398, 393.5 and 391 nm comes from the $z^6P \leftarrow {}^6S$ transition within the same matrix site whereas the second group (observed three lines in the absorption but two lines in the MCD) originates from the same transition but a different matrix site. Upon warming the matrix (temperature-dependent MCD), the intensity of the group of two lines decreased markedly whereas the intensity of the

FIGURE 31. Absorption (top) and MCD (bottom) spectra of manganese species in an argon matrix. Full line T = 12.9 K; dotted line T = 29.7 K.

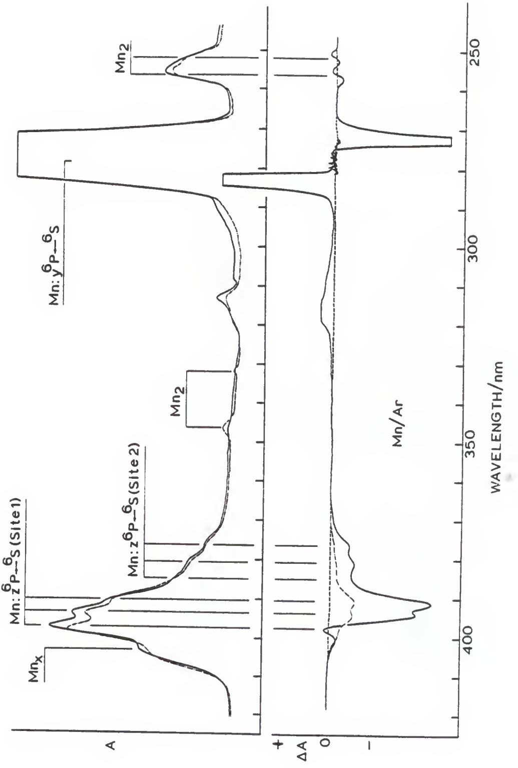
A
+
ΔA
0
−
Mnx
Mn: z6P←6S (Site1)
Mn: z6P←6S (Site 2)
Mn2
Mn: y6P←6S
Mn2
Mn/Ar
400
350
300
250
WAVELENGTH/nm

TABLE 8. MCD Band Positions, Matrix Shifts and Assignments for Mn Species Isolated in an Argon Matrix

| Transition | | Gaseous | | Ar Matrix[a] | | | Shift | MCD signs | | Species | Site |
|---|---|---|---|---|---|---|---|---|---|---|---|
| | J | ν/cm$^{-1}$ | Δν/cm$^{-1}$ | λ/nm | ν/cm$^{-1}$ | Δν/cm$^{-1}$ | Δν = νAr − νgas | Predicted | Observed | | |
| ? | | | | 400.5 | 24962 | | | | N | $Mn_x$ (X=5 ?) | ? |
| $z^6P_J \leftarrow {}^6S$ | 3/2 | 24779 | 9 | 398.0 | 25119 | 287 | 340 | + | + | Mn | 1 |
| | 5/2 | 24788 | 14 | 393.5 | 25406 | 162 | 618 | + | − | | |
| | 7/2 | 24802 | | 391.0 | 25568 | | 766 | − | − | | |
| $z^6P_J \leftarrow {}^6S$ | 3/2 | 24779 | 9 | 385.0 | 25967 | 272 | 1188 | + | +(?) | Mn | 2 |
| | 5/2 | 24788 | 14 | 381.0 | 26239 | 314 | 1451 | + | − | | |
| | 7/2 | 24802 | | 376.5 | 26553 | | 1751 | − | − | | |
| ? ← S=2 | | | | 347.0<br>331.5 | 28810<br>30157 | | | ?<br>? | N<br>N | $Mn_2$ | 1 |
| $z^4P_J \leftarrow {}^6S$ | 5/2 | 31001 | 75 | 319.0 | 31339 | 247 | 338 | + | + | Mn | 1 |
| | 3/2 | 31076 | 49 | 316.5 | 31586 | 252 | 510 | + | + | | |
| | 1/2 | 31125 | | 314.0 | 31838 | | 713 | F | ? | | |
| $y^6P_J \leftarrow {}^6S$ | 3/2 | 35690 | 36 | 282.0 | 35451 | | −239 | + | + | Mn | 1 |
| | 5/2 | 35726 | 44 | -- | -- | 639 | -- | + | ? | | |
| | 7/2 | 35770 | | 277.0 | 36090 | | 320 | − | − | | |
| $y^6P_J \leftarrow {}^6S$ | 3/2 | 35690 | 36 | 276.5 | 36156 | | 466 | + | + | Mn | 2 |
| | 5/2 | 35726 | 44 | -- | -- | 330 | -- | + | ? | | |
| | 7/2 | 35770 | | 274.0 | 36486 | | 716 | − | − | | |
| S'=1 ← S=0 | | | | 256.0<br>252.5 | 39051<br>39592 | | | +<br>+ | +<br>+ | $Mn_2$ | 1<br>2 |

N = no MCD signal. F = Forbidden.

group of three lines decreased slowly. This indicates that these two groups are independent of one another and are characteristic of different sites in the matrix.

For the absorption band located at 400.5 nm no MCD signal was detected. However, irradiation of this band at ~400 nm in argon and xenon matrices produced a weak MCD signal which likely comes from a transition of $Mn_x$ molecule with the value of x as unspecified.

The two bands located at 347 nm and 331.5 nm are assigned to a $Mn_2$ transition. A detailed discussion of these two bands is provided in the next section. A group of triplet bands centered at 319, 316.5 and 314 nm can be assigned to the $z^4P \leftarrow {}^6S$ transition. Although this transition is spin forbidden (but orbitally allowed), the spin-orbit coupling with $y^6P$ state will make the transition possible.

The triplet originating from the $y^6P \leftarrow {}^6S$ transition appears to result from two different matrix sites (called site 1 and 2). The matrix shift for site 2 is larger by a factor of 2. Figure 32 shows the MCD temperature dependence of Mn/Ar in the 300-250 nm range at two selected temperatures (13 K and 20 K).

The two weak MCD bands centered at 256 nm and 252.2 nm are assigned to $Mn_2$ molecule within different sites. The predicted and observed MCD signs for these two bands are the same (both positive). Since the MCD spectrum of these bands is temperature independent (A terms) these transitions must arise from an S = 0 level within the ground state of the $Mn_2$

FIGURE 32. MCD temperature dependence of manganese species in an argon matrix at 13 K and 20 K.

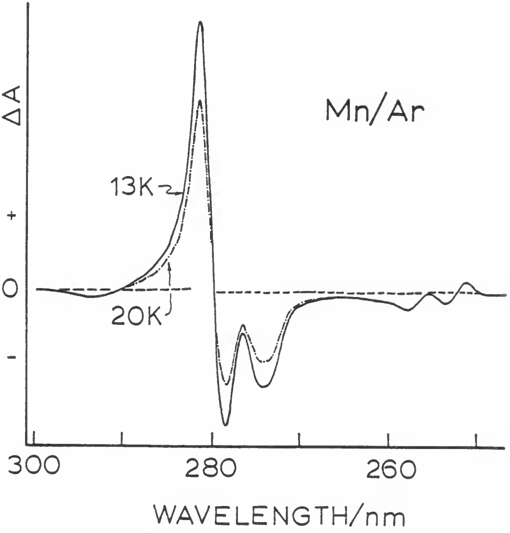
ΔA
+
0
-
Mn/Ar
13K
20K
300
280
260
WAVELENGTH/nm

molecule. Although the MCD intensity of these bands are relatively low, the lower energy band (256 nm) has a very intense absorption band compared to the higher energy one (252.5), which only appears as a shoulder (see Figure 31).

### $Mn_2$

There has been increasing interest in the bonding properties of small metal clusters in recent years. The homonuclear diatomic molecules of the first transition period have potential theoretical, astronomical, and high temperature importance. Investigations of the $Mn_2$ molecule have provided a number of interesting though still controversial conclusions.

In 1964 Nesbet[85] performed a complete ab initio approximate Hartree-Fock calculation at three internuclear separations. He predicted that the molecule should be weakly bound (0.79 eV), antiferromagnetic, and the Mn atoms in the $Mn_2$ molecular were exchange coupled with an exchange energy of $-4.13\ cm^{-1}$ so that it should have a $^1\Sigma_g$ ground state.

Kant et al.[80,86] observed the $Mn_2$ molecule via mass spectrometry and measured its dissociation energy ($D_0^o$) as 3±3 Kcal $mol^{-1}$ (0.13 eV). From this small value, these authors concluded that $Mn_2$ was a van der Waals-type molecule. Cooper et al.[87] performed an extended Hückel calculations on a number of first-row transition-metal dimers, including $Mn_2$. Their calculations showed a strong bond (1.22 eV), but the calculations were deemed by the authors to be unreliable since they did not predict the weak van der

Waals-type band observed by Kant et al.[86] Recently, using a density functional method, Harris and Jones[88] found essentially identical binding energies (1.25 eV) for two of the possible ground states ($^{11}\Sigma_g$ and $^{11}\pi_u$). The latter approach has, however, been called into question.[89] Goodgame and Goddard[89] believe that local density or local spin density calculations on the molecules of transition metals containing multiple unpaired d electrons are suspect because of their inability to account for the high spin coupling in the separated atoms and for the weakly overlapping orbitals on different centers. However, to overcome these problems, these authors proposed a generalized valence bond-van der Waals method. Although the application to $Mn_2$ molecule has not yet been made, however, for $Cr_2$ molecule (compare Mn atom configuration, $4s^2\ 3d^5$, to Cr atom, $4s^1\ 3d^5$) they predict a $^1\Sigma_g^+$ ground state with a 0.35 eV binding energy and an exchange energy of $-93\ cm^{-1}$.

The only experimental work reported on the $Mn_2$ molecule is the visible absorption spectrum,[74] mass spectrometry,[80] and recently ESR.[84,90] Because of the presence of the variety of different species (e.g., atoms, dimer, etc.) in the matrix, the interpretation of optical matrix bands has proven very difficult. Using ESR spectroscopy, Baumann et al.[84] recently observed $Mn_2$ molecule in several matrices and showed that it is antiferromagnetic. These authors determined an exchange energy of $-8 \pm 4\ cm^{-1}$.

In spite of these and other reports[77,78] on manganese species isolated in rare gas matrices, the identity of the different species present remains unsettled. Moreover, the large discrepancy between theoretical results call for clear and precise experimental data. Indeed, it was in part the aim of this study to employ optical absorption and MCD techniques for the following purposes: (1) to confirm the existence of the matrix-isolated $Mn_2$ molecule and to identify several of its optical absorption bands, and (2) to demonstrate that the $Mn_2$ molecule is antiferromagnetic and to give a precise value for its ground-state exchange energy.

In Figure 33 is shown a selected portion of the absorption and MCD spectra of Mn matrix-isolated in argon. Several depositions were performed keeping constant the flow rate of the argon isolant gas but increasing the temperature of the Knudsen cell. The resulting absorption spectra are quite different: the relative intensities of the "a" band to the "b, c, d" bands varied with the temperature of the cell (the former band increasing with increasing cell temperature). In all cases, the width and intensity of the bands varied only slightly with the temperature of the matrix (13-27 K). The MCD temperature variation of these bands shows that the "a" band (403 nm) is temperature-independent, whereas the "b, c, d" bands (and the shoulders to higher energy) are temperature-dependent. That difference in the MCD variation is amplified in xenon matrices when the "a" band is well separated from the "b, c, d" bands (see Figure 28). It can further be deduced from the MCD that the ground state of the species giving rise to the "a" band is orbitally non-degenerate.

FIGURE 33. Selected part of the absorption spectrum (bottom) and MCD spectrum (top) of Mn matrix-isolated in Ar. Full line T = 12.5 K; dotted line T = 28 K.

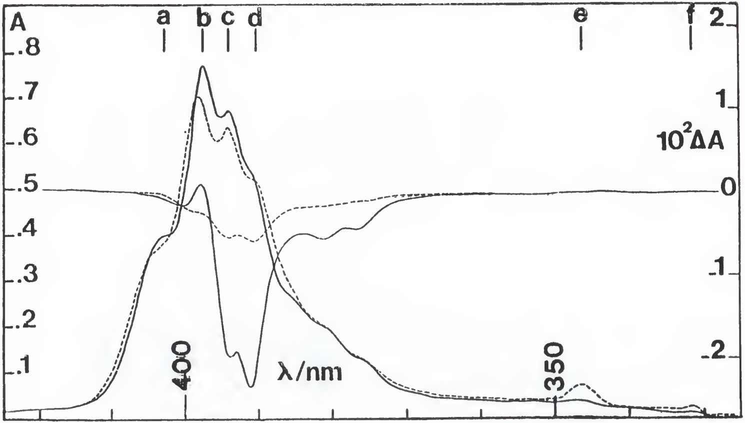
A
.8
.7
.6
.5
.4
.3
.2
.1
a
b
c
d
e
f
2
1
$10^2\Delta A$
0
-1
-2
400
λ/nm
350

The vibronic interaction as well as spin-orbit splitting causes the splitting of the atomic $^6P$ state. Thus, it is expected that temperature-dependent MCD terms will be associated with each component (J = 3/2, 5/2 and 7/2) of the $^6P \leftarrow {}^6S$ transition. Rivoal and Briat[91] found that the zeroth-order moment taken over the three components to be zero. For the case of Mn/Xe in this study, it is exactly what we observed.

In the argon matrix (see Figure 33) the b, c and d bands seem to be superimposed over a large negative signal giving rise at higher energy to the shoulders (376.5, 381, 385 nm). As mentioned before, since these b, c and d bands correlate well with the $z^6P \leftarrow {}^6S$ gas-phase transition,[66] they are attributed to atomic manganese. The shoulders raise a question. They are not observed either in the krypton matrix or in the xenon matrix. There are two possibilities to assign them. They can be attributed either to the $z^6P \leftarrow {}^6S$ transition with different lattice site (see Table 8) or to the $Mn_2$ transitions originating from S = 1 ground state (vide infra). We prefer the former interpretation since (1) all other atomic Mn transitions in Ar appear doubled and there is no reason not to expect this transition to behave similarly and (2) these bands mimic the lower energy $z^6P$ bands in their temperature dependence, i.e., they increase in intensity with decrease in temperature. Transitions from the S = 1 level of $Mn_2$ should behave in an opposite fashion.

In Figure 33 two weak transitions are marked at 347 nm (e) and 331.5 (f). The absorption intensity of these bands grows with increasing temperature (13-27 K range). Figure 34 shows the absorption spectra of these two bands at three selected temperatures. The band shape of the associated MCD signal is the same as the absorption, but increases more slowly with temperature. At its maximum (~19-20 K), it shows a signal-to-noise ratio of ~3, and it cannot be distinguished from the noise at the lowest temperature. From both absorption and MCD temperature variations it can be concluded that these transitions come from an "excited ground state," i.e., a level whose energy above the ground state is of the order of magnitude of kT. Since the temperature dependence of atomic manganese is quite different from this, these bands must arise from another species. It is postulated that it is $Mn_2$ molecule and it is shown below that the results are in good agreement with this postulation.

From symmetry considerations,[92] it is known that the ground state of $Mn_2$ molecule (composed of two $^6S$ Mn atoms) has zero angular momentum. With the total spin ranging from 0 to 5 and parity of the different states being positive, the possible terms for the ground state of the $Mn_2$ can be listed as:

$$^{11}\Sigma_u^+,\ ^9\Sigma_g^+,\ ^7\Sigma_u^+,\ \ ^5\Sigma_g^+,\ \ ^3\Sigma_u^+,\ \ ^1\Sigma_g^+.$$

In order to deduce the relative energies of these states, it is necessary to consider a Hamiltonian in which the exchange term plays the dominant role.[93] Considering only the isotropic term, $H = -JS_i \cdot S_j$, the energies of the various S states (0, 1, 2, 3, 4, 5) are given by the Landé interval rule:

FIGURE 34. Enlarged spectrum of transitions e and f of Figure 33 at three selected temperatures.

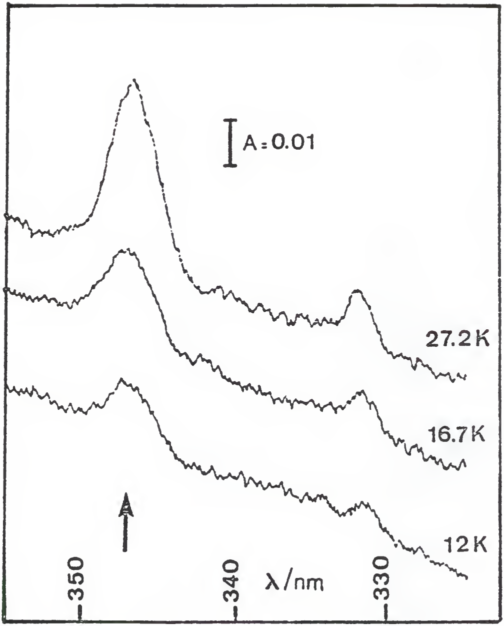
A = 0.01
27.2 K
16.7 K
12 K
350
340
330
λ/nm

$$W_S = -\tfrac{1}{2}\, J\, [S\,(S+1) - \frac{35}{2}] \qquad (51)$$

Figure 35 shows a typical scheme for the energy levels of the ground-state $Mn_2$ molecule.

The intensities of the transitions originating from the various S states can be related to their Boltzmann populations by the following equation:

$$P_S \,\alpha\, (2S + 1)\, \exp\,(-\, W_S/kT)/Z \qquad (52)$$

where Z is the partition function and in the case of $Mn_2$ molecule can be written as:

$$Z = \sum_{S=0}^{5} (\, 2S + 1)\, \exp\,(-\, W_S/kT) \qquad (53)$$

Assuming that the band located at 347 nm (bandwidth 150 $cm^{-1}$) originates from only one of the S states with a transition probability $I_S$, its total absorption intensity (area or zeroth-order moment) can be obtained by

$$A \,\alpha\, (2S + 1)\, I_S\, \exp\,(-W_S/kT)/Z \qquad (54)$$

Therefore, a plot of ln A versus reciprocal temperature should be linear if Z remains approximately constant in the investigated temperature range. If more than one S state participates, the linearity of this plot will be rather unlikely. In Figure 36 is shown the temperature variation of the zeroth-order moment of the "e" band (cf. Figure 33). The intensity of the "f" band (see Figure 33) is too low to give an accurate plot. The gradient of the semi-log plot of the zeroth-order moment of band e vs. $\frac{1}{T}$ is almost linear,

FIGURE 35. Typical level scheme of the ground-state $Mn_2$ molecule in the case of isotropic exchange with and without external applied field.

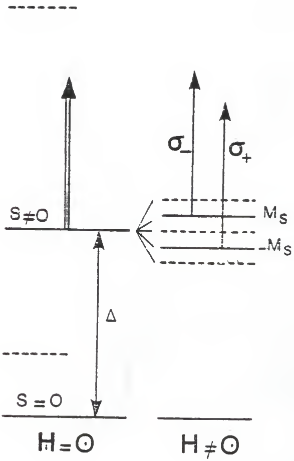
σ₋
σ₊
S≠O
$M_S$
$-M_S$
Δ
S = O
H = O
H ≠ O

FIGURE 36. Semi-log plot of the zeroth-order moment of band e versus reciprocal temperature. The squares represent the experimental points, their sizes corresponding to the estimated errors on T (horizontal bar) and A (vertical bar). The dots correspond to the fitted values with $W_S = 10.3 \pm 0.6$ $cm^{-1}$.

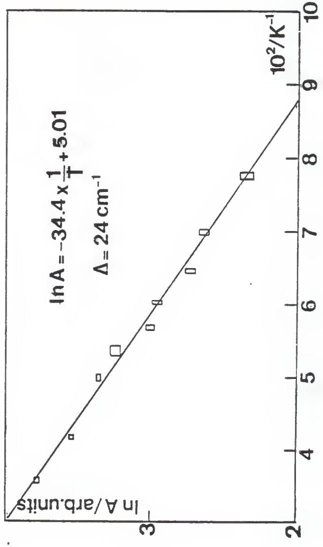
ln A = −34.4 x 1/T + 5.01
Λ = 24 cm⁻¹
ln A/arb.units
10²/K⁻¹
2
3
4
5
6
7
8
9
10

indicating that one state is mainly involved in the band. Assuming that the energy separation follows the Landé interval rule (see Figure 35), the experimental points have been fitted to different theoretical laws. The different fits including one, two or three states, clearly show that the contribution to the intensity arising from the S = 0 or 1 states are very close to zero for S = 0 or 1. Note that the best fit is reached when only two parameters, J (the exchange energy) and A (the absorption intensity) of the transition originating from the S = 2 state, are included in the theoretical expression. The value of exchange energy is determined to be = -10.3 ± 0.6 $\mathrm{cm}^{-1}$ which is in good agreement with the ESR result[92] of -8 ±4 $\mathrm{cm}^{-1}$.

If an external magnetic field is applied, an S level can be split into 2S + 1 levels, labelled $M_S$. If the transition from one particular $M_S$ to an excited level is $\sigma_+$ polarized, the one from the $-M_S$ level is $\sigma_-$ polarized. Let $I_{MS}$ represent the square of the dipole matrix element associated with these transitions, then a generalized expression for the MCD can be written as:

$$\Delta A \;\alpha\; A \sum_{M_S} [\exp(M_S x) - \exp(-M_S x)] I_{M_S} \tag{55}$$

where $x = g\mu_B B/kT$ is of the order of magnitude of $\frac{1}{T}$ with B = 0.55T. Since the temperature range of the experiments is limited to 13-27 K, the exponential terms can be expanded. Retaining only the first two terms gives rise to

$$\Delta A \;\alpha\; (2S + 1)(2g\frac{\mu_B B}{kT})(\frac{\exp(-W_S/kT)}{Z}) \sum_{M_S} M_S I_{M_S} \tag{56}$$

Only for the X = 2 level does this function increase smoothly above 13 K, reach its maximum around 21 K and then slowly decrease between 21 and 28 K, in good agreement with the experiment. However, making a more quantitative comparison is impossible since the S/N (signal to noise) ratio is poor.

Undoubtedly transitions from the S = 0 or S = 1 states are present in the spectra. We have discussed one at 287 nm in the previous section. The intensity variation of transitions originating from S = 1 state cannot clearly be seen because only the temperature range > 13 K was explored here. Future experiments at temperatures down to 1.5 K are planned in our laboratory to settle this point.

The main conclusions of this section are as follows: (1) the Mn/Ar matrix bands at 347 nm and 331.5 nm are due to $Mn_2$ molecule, (2) $Mn_2$ is an antiferromagnetic molecule with a $^1\Sigma_g^+$ ground state, (3) the $Mn_2$ ground-state exchange energy is $-10.3 \pm 0.6$ cm$^{-1}$, in good agreement with the ESR result[90] and Nesbet's[85] calculated value of $-4$ cm$^{-1}$. Furthermore the present work supports the contention of Goodgame and Goddard[89] that the present local density functional approaches do not yield reliable results for molecules composed of transition metals containing multiple unpaired d electrons.

# CHAPTER VII

# CHROMIUM IN THE RARE GAS MATRICES

In this chapter the experimental results obtained for the absorption and MCD of chromium atom and/or clusters isolated in argon, krypton and xenon matrices will be presented. The observed band assignments in each of these matrices as well as an analysis of the band moments for the Cr/Xe system will also be discussed.

The ground state of gaseous chromium atom is $^7S_3$ corresponding to the $3d^5$ 4s electronic configuration.[66] For matrix-isolated chromium atoms, it is expected that the two spin- and orbitally-allowed $z^7P \leftarrow {}^7S$ and $y^7P \leftarrow {}^7S$ transitions should be easily observed. In the gas phase, the first allowed band ($z^7P_{2,3,4} \leftarrow {}^7S$) is due to the $3d^5$ 4p ← $3d^5$ 4s transition and is seen in the visible region (23,300-23,500 $cm^{-1}$), while the second band ($y^7P_{2,3,4} \leftarrow {}^7S$) arises from the $3d^4$ 4s 4p ← $3d^5$ 4s transition and falls in the ultraviolet region (27,700-27,900 $cm^{-1}$).

In their studies of several transition metal atoms Mann and Broida[60] reported part of the absorption spectrum of chromium atoms in an argon matrix at 4.2 K. They observed three components clustered around the $y^7P$ excited state energy, but no bands corresponding to the lower energy one ($z^7P$). The half-widths of the three observed components in argon were about 500 $cm^{-1}$ and were blue-shifted (1,900-2,700 $cm^{-1}$)

compared to their respective gas phase values. The shift increased with the band energy of the component. As we will show later, probably only one (possibly two) of these peaks is (are) actually due to transitions of the chromium atom. In addition to the triplet, these authors observed two weaker bands located at 299.8 nm and 294.7 nm and assigned them to the spin forbidden transitions ($y^5P^\circ_{2,3} \leftarrow {}^7S$). Since the matrix shifts implied by the assignments of these two bands (~4000 $cm^{-1}$) were large, these authors held open the possibility that the bands were the result of some unknown impurities in their matrix.

The matrix work by Gruen[94] resulted in the observation of both the septets, $y^7P$ and $z^7P$, but his matrices apparently contained considerable amounts of small chromium clusters. It is of interest to note that the overall splitting of the $z^7P$ state band increased by a factor of three on going from the gas phase to the argon matrix.

Kündig, Moskovits and Ozin[95] reported the absorption spectrum of Cr which was quite different from that reported by Mann and Broida[60] and that by Gruen.[94] The latter two also differed from one another. These authors pointed out that the discrepancies were probably attributable to impurities and/or higher chromium clusters in the earlier studies. The authors observed a band located at 455 nm and assigned it to the $Cr_2$ molecule. Recent work by Michalopoulos et al.[96] on supersonic nozzle jet spectroscopy of $Cr_2$ identified this band as indeed due to $Cr_2$ and assigned it to the ${}^1\Sigma_u^+ \leftarrow {}^1\Sigma_g^+$ transition.

Recently, DiLella et al.[97] used Raman and resonance Raman spectroscopy to study both chromium dimers and trimers in argon matrices. Two resonance Raman progressions with vibrational constants $\omega''_e = 427.5\ \mathrm{cm}^{-1}$; $\omega''_e X''_e = 15.75\ \mathrm{cm}^{-1}$ and $\omega''_e = 313\ \mathrm{cm}^{-1}$; $\omega''_e X''_e = 2\ \mathrm{cm}^{-1}$ were assigned to $Cr_2$ and $Cr_3$, respectively. Using symmetry considerations, the authors deduced that the $Cr_3$ molecule has a $C_{2V}$ point group with an apical angle around 60°, suggesting that it is perhaps a Jahn-Teller distorted $D_{3h}$ molecule.

## Experimental Procedure

Following the standard procedure, the tantalum Knudsen cell (wall thickness = 0.015") was filled with chromium powder (Spex, containing 40-80 ppm iron) and degassed thoroughly at 1250° C. Resistive heating of the cell (to 1425° C for argon matrices, 1450° C for krypton matrices, and 1400° C for xenon matrices as determined by an optical pyrometer) produced a metal beam which was directed at a $CaF_2$ sample window (cooled by a closed cycle helium cryostat) and cocondensed with the isolant rare gas (Matheson, research grade) for a period of two hours. The sample window was held at 14 K for argon deposits, 16 K for krypton deposits and 20 K for xenon deposits.

Calibration for moment calculations was performed using the standard, (+) camphorsulfonic acid (molecular ellipticity = 0.201 at 290 nm[73]) and an aqueous solution of $[Co(en)_3]Cl$. (d-tartrate), whose $\varepsilon_{max}$ is 84 l $\mathrm{cm}^{-1}$ $\mathrm{mole}^{-1}$ at 469 nm.[52]

## Results and Discussion

### Cr/Kr

In Figure 37 is shown the absorption and MCD spectra of chromium species isolated in a krypton matrix. The MCD spectrum shows both positively- and negatively-signed bands which have been shown by their temperature dependence to be $C_0$ terms. Figure 38 shows the temperature dependence of the Cr species in a krypton matrix. The MCD band positions and assignments are given in Table 9.

The absorption bands located at 480 nm, 467.5 nm, and 458 nm exhibit no MCD signal and are assigned to the $Cr_2$ molecule. The ground state of $Cr_2$ is known to be $^1\Sigma_g^+$. Since no MCD signal was observed for these bands they must arise from a $^1\Sigma_u^+ \leftarrow {}^1\Sigma_g^+$ transition of the $Cr_2$ dimer. The three bands arise from $Cr_2$ in three different sites. Annealing the matrix to 50 K resulted in the disappearance of the lowest energy band, drastically decreased the intensity of the middle band and slightly decreased the intensity of the highest energy band (cf. Figure 39). Since the intensity of these bands changes differently and irreversibly with temperature and there are no other $^1\Sigma$ or $^1\Pi$ states in this range (unless under the atomic bands) it can be concluded that these three bands belong to $Cr_2$ molecules residing in three different sites.

The predicted MCD signs for the bands located at 380.5 nm, 372.5 nm, and 362 nm are positive, positive, and negative, respectively, which are in agreement with the observed signs. These bands are assigned to the components of the $z^7F \leftarrow {}^7S$

FIGURE 37. Absorption (top) and MCD (bottom) spectra of chromium species in a krypton matrix.

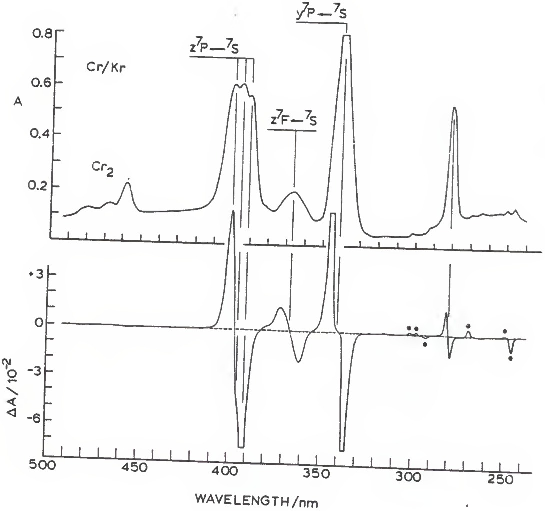
$y^7P \leftarrow {}^7S$
$z^7P \leftarrow {}^7S$
$z^7F \leftarrow {}^7S$
Cr/Kr
$Cr_2$
A
0.8
0.6
0.4
0.2
+3
0
-3
-6
$\Delta A/10^{-2}$
500
450
400
350
300
250
WAVELENGTH/nm

FIGURE 38. MCD temperature dependence of the chromium species in a krypton matrix. The intensity decreases with increasing temperature.

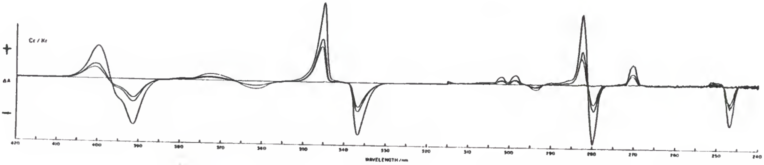
Cr / Kr
+
ΔA
−
420
410
400
390
380
370
360
350
340
330
320
310
300
290
280
270
260
250
240
WAVELENGTH / nm

TABLE 9. MCD Band Positions, Matrix Shifts and Assignments for Cr Species Isolated in a Krypton Matrix

| Transition | | Gaseous[a] | | Kr Matrix[b] | | | Shift | MCD signs | | Species[c] |
|---|---|---|---|---|---|---|---|---|---|---|
| | J | $\nu$/cm$^{-1}$ | $\Delta\nu$/cm$^{-1}$ | $\lambda$/nm | $\nu$/cm$^{-1}$ | $\Delta\nu$/cm$^{-1}$ | $\Delta\nu = \nu\text{Kr} - \nu\text{gas}$ | Predicted | Observed | |
| | | | | 480.0** | 20828 | 556 | -923 | N | N | |
| $^1\Sigma_u^+ \leftarrow {}^1\Sigma_g^+$ | | 21751±1* | | 467.5** | 21384 | 444 | -367 | N | N | $Cr_2$ (three sites) |
| | | | | 458.0** | 21828 | | +77 | N | N | |
| | 2 | 23305 | 81 | 400.0 | 24993 | 316 | 1688 | + | + | |
| $z^7P_J^o \leftarrow a^7S$ | 3 | 23386 | 113 | 395.0 | 25309 | 227 | 1923 | + | − | Cr |
| | 4 | 23499 | | 391.5 | 25536 | | 2037 | − | − | |
| | 2 | 25089 | 117 | 380.5 (weak) | 26274 | 564 | 1185 | + | + | |
| $z^7F_J^o \leftarrow a^7S$ | 3 | 25206 | 154 | 372.5 | 26838 | 778 | 1632 | + | + | Cr |
| | 4 | 25360 | | 362.0 | 27616 | | 2256 | − | − | |
| | 2 | 27729 | 91 | 345.5 | 28935 | | 1206 | + | + | |
| $y^7P_J^o \leftarrow a^7S$ | 3 | 27820 | 115 | -- | -- | 757 | -- | + | N | Cr |
| | 4 | 27935 | | 336.7 | 29692 | | 1757 | − | − | |
| $y^5D \leftarrow {}^5D$ | 4 | 33096 | 411 | 302.0 | 33103 | | 7 | + | + | *** Fe |
| $y^5D_J \leftarrow {}^5D$ | 3 | 33507 | | 298.3 | 33514 | | 7 | + | + | *** Fe |
| ? | | | | 282.5 | 35388 | 316 | | + (Pseudo A term) | + | $Cr_3$ |
| | | | | 280.0 | 35704 | | | − | − | |
| $y^5P_J \leftarrow {}^5D$ | 3 | 36767 | | 270.0 | 37026 | | 259 | + | + | *** Fe |
| $x^5D_J \leftarrow {}^5D$ | 4 | 39626 | | 250.0 (weak) | 39988 | | 362 | + | + | *** Fe |
| $x^5F_J \leftarrow {}^5D$ | 5 | 40257 | | 247.0 | 40474 | | 217 | − | − | *** Fe |

[a] wavenumber marked *, taken from reference 96.
[b] wavelengths marked **, taken from the absorption spectrum.
[c] species marked ***, are Fe atoms which appear in the matrix due to impurity of Cr sample (see text).
N = no MCD signal.

FIGURE 39. Absorption spectra of chromium in a krypton matrix. Full line before annealing the matrix; dotted line after annealing the matrix at 50 K. Both spectra run at 14 K.

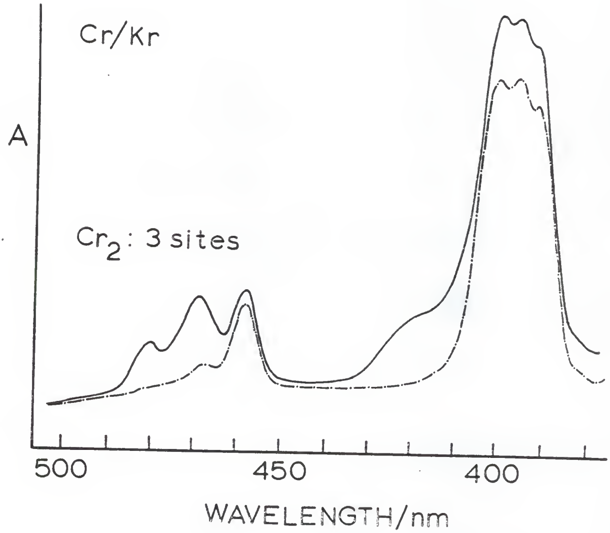
Cr/Kr
A
Cr$_2$: 3 sites
500
450
400
WAVELENGTH/nm

transition. The other possible assignments, involving excited states which fall between the two allowed $^7P$ states,[66] can be reasonably eliminated by the following arguments:

(1) For the $^5P \leftarrow ^7S$ transition only positive $C_0$ terms are predicted for transitions to the components with J = 2 and 3. (2) For the $^7D \leftarrow ^7S$ transition positive, positive, and negative $C_0$ terms are expected for the components with J = 2, 3, and 4, as observed. However, the $z^7D$ state is only about 300 $cm^{-1}$ to lower energy of $y^7P$ state. It is not expected that the matrix could induce a shift to about 1800 $cm^{-1}$ away. (3) The transitions from the $a^7S$ ground state to $a^3H$, $a^3G$, $a^3F$, $b^3P$, and $b^3G$ excited states are doubly spin forbidden (i.e., S = 2) and should therefore be extremely weak. (4) For the $^5D \leftarrow ^7S$ transition positive, positive, negative $C_0$ terms are predicted corresponding to components with J = 2, 3, and 4, respectively, but these transitions should be very weak since they require second order spin-orbit interaction to the $^7P$ excited state. (5) For the $z^7F \leftarrow ^7S$ transition positive, positive, and negative $C_0$ terms are expected as observed in the MCD spectrum. Although this transition is orbitally forbidden in the gas phase,[66] it becomes allowed in an octahedral site symmetry. This is because the gaseous F state correlates with $A_2 + T_1 + T_2$ in the octahedral site. The $T_1(F) \leftarrow A_1(S)$ transition will become allowed in the octahedral site symmetry. Mixing will probably occur with the nearlying $^7P$ states which in the octahedral site symmetry also become $T_1$. Thus, evaluating all of these choices, the $z^7F \leftarrow a^7S$ transitions is the most reasonable selection for this assignment.

The species marked *** are due to iron impurity bands. The iron impurity in the chromium sample (40-80 ppm) appears clearly (cf. Figure 13 for Fe/Kr spectra) in the MCD spectra of chromium isolated in argon, krypton, and xenon matrices. Initially a surprise, this observation can be rationalized as follows. The temperatures required to achieve about $10^{-3}$ torr metal vapor from iron powder and chromium powder are 1600 K and 1550 K, respectively. Since the melting point of iron (1536 °C) is less than the melting point of chromium (1875 °C) and since the amount of iron impurity is considerable in the chromium sample, we believe that the Fe impurity was preferentially emitted from the Knudsen cell and with its apparent higher extinction coefficient was observed in the clear u.v. region of the chromium spectra.

The triplet of bands at 400 nm, 395 nm, and 391.5 nm arise from the $z^7P \leftarrow {}^7S$ transition. Figure 40 shows the temperature dependence of the MCD of the Cr atom bands (~395 nm) in a krypton matrix. The band separation (543 $cm^{-1}$) is much larger than the known gas phase splitting (194 $cm^{-1}$) by a factor of about 3. This indicates the presence of an active Jahn-Teller effect in the $z^7P$ excited state of the chromium atom. The observed sign of MCD for the J=3 component is negative whereas the predicted one is positive. Both the increased band separation and the reversal in MCD C terms sign of the middle component appear to be characteristic of the Jahn-Teller effect in excited P states. The presence of the Jahn-Teller effect in Cr/rare gas matrices, to be proven in a latter section, has been established previously for Cu/ rare gas system.[19]

FIGURE 40. Temperature dependence of the chromium atom $C_o$ term in a krypton matrix.

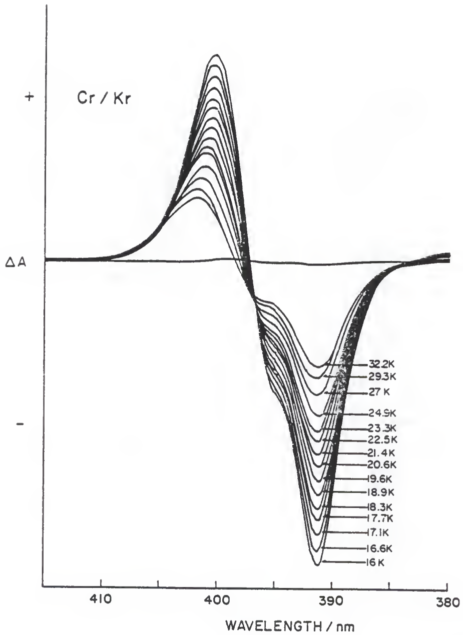
Cr / Kr
+
ΔA
-
32.2K
29.3K
27 K
24.9K
23.3K
22.5K
21.4K
20.6K
19.6K
18.9K
18.3K
17.7K
17.1K
16.6K
16 K
410
400
390
380
WAVELENGTH / nm

The two bands centered at 345.5 nm and 336.7 nm are assigned to the $z^7P_2 \leftarrow a^7S$ and $z^7P_4 \leftarrow a^7S$ transitions, respectively. The lower energy band corresponds to the component with J=2 (positive $C_0$ term) and the higher energy one corresponds to the J=4 component (negative $C_0$ term). Note that the J=3 component is not resolved (see Figure 37).

Two bands located at 282.5 nm and 280 nm with a band separation of 316 $cm^{-1}$ are assigned to the $Cr_3$ molecule. These bands are temperature dependent but the absorption maximum matches with the zero-crossing of the MCD bands (called Pseudo-A term). It is interesting to note that this band has a $C_0/D_0$ ratio much less than that of the atomic chromium bands corresponding to the $^7P \leftarrow {}^7S$ transition. Since the values of $D_0$ are about the same, this must mean that the $C_0$ term is quenched. Such quenching could arise from a deviation from linearity (i.e., from $D_{\infty h}$ symmetry) or from equilateral triangularity (i.e., from $D_{3h}$ symmetry).

## Cr/Xe

Figure 41 shows the absorption and MCD spectra of chromium species isolated in a xenon matrix. The MCD spectrum shows temperature dependent $C_0$ terms in which the intensity of the bands decreases with increased temperature. Band assignments and MCD band positions are given in Table 10.

The absorption band located at 473 nm exhibits no MCD signal and is assigned to a $Cr_2$ transition. The $Cr_2$ species resides in a single type of lattice site in the xenon matrices. Three MCD bands at 383.8 nm, 378 nm, and 372 nm

FIGURE 41. Absorption (top) and MCD (bottom) spectra of chromium species in a xenon matrix.

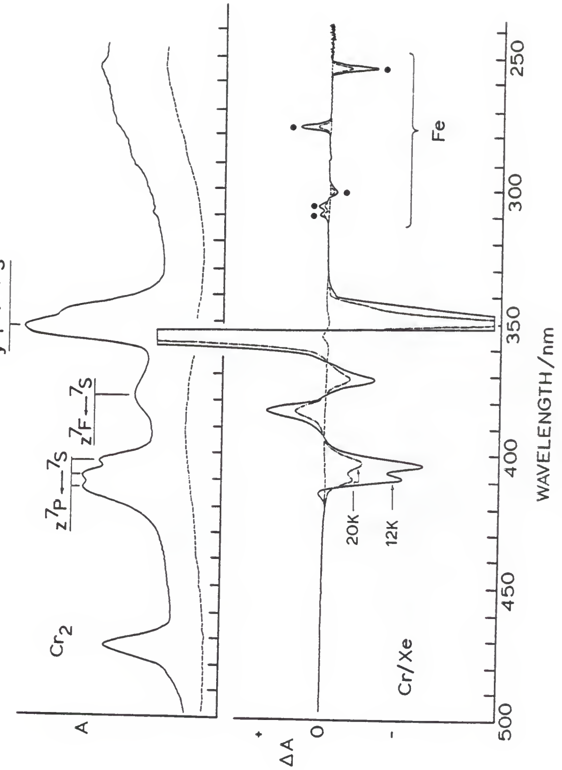
y⁷P ← ⁷S
z⁷F ← ⁷S
z⁷P ← ⁷S
Cr₂
A
ΔA
+
0
-
Cr/Xe
20K
12K
Fe
500
450
400
350
300
250
WAVELENGTH /nm

TABLE 10. MCD Band Positions, Matrix Shifts and Assignments for Cr Species Isolated in a Xenon Matrix

| Transition | J | Gaseous[a] $\nu$/cm$^{-1}$ | Gaseous[a] $\Delta\nu$/cm$^{-1}$ | Xe Matrix[b] $\lambda$/nm | Xe Matrix[b] $\nu$/cm$^{-1}$ | Xe Matrix[b] $\Delta\nu$/cm$^{-1}$ | Shift $\Delta\nu = \nu Xe - \nu gas$ | MCD signs Predicted | MCD signs Observed | Species[c] |
|---|---|---|---|---|---|---|---|---|---|---|
| $^1\Sigma_u^+ \leftarrow {}^1\Sigma_g^+$ | | 21751±1* | | 473.0** | 21136 | | -615 | N | N | $Cr_2$ |
| $z^7P_J^o \leftarrow a^7S$ | 2 | 23305 | 81 | 415.0 | 24090 | 353 | 785 | + | + | Cr |
| | 3 | 23386 | 113 | 409.0 | 24443 | 302 | 1057 | + | - | |
| | 4 | 23499 | | 404.0 | 24745 | | 1246 | - | - | |
| $z^7F_J^o \leftarrow a^7S$ | 2 | 25089 | 117 | 383.8 (weak) | 26048 | 400 | 959 | + | + | Cr |
| | 3 | 25206 | 154 | 378.0 | 26448 | 426 | 1242 | + | - | |
| | 4 | 25360 | | 372.0 | 26874 | | 1514 | - | + | |
| $y^7P_J^o \leftarrow a^7S$ | 2 | 27729 | 91 | 356.0 | 28082 | 279 | 353 | + | + | Cr |
| | 3 | 27820 | 115 | 352.5 | 28361 | 616 | 541 | + | - | |
| | 4 | 27935 | | 345.0 | 28977 | | 1042 | – | – | |
| $y^5D \leftarrow {}^5D$ | 4 | 33096 | 411 | 310.0 | 32249 | | -847 | + | + | *** Fe |
| $y^5D_J \leftarrow {}^5D$ | 3 | 33507 | | 306.5 | 31627 | | -890 | + | + | *** Fe |
| $y^5F_J \leftarrow {}^5D$ | 5 | 33514 | | 301.0 | 33213 | | -301 | - | - | *** Fe |
| $y^5P_3 \leftarrow {}^5D$ | 3 | 36767 | | 277.0 | 36090 | | -677 | + | + | *** Fe |
| $x^5F_J \leftarrow {}^5D$ | 5 | 40257 | | 255.0 | 39204 | | -1053 | - | - | *** Fe |

[a] wavenumber marked *, taken from reference 96.
[b] wavelengths marked **, taken from the absorption spectrum.
[c] species marked ***, are Fe atoms which appear in the matrix due to impurity of Cr sample (see text).
N = no MCD signal.

with a band separation of 826 $cm^{-1}$ are assigned to the three components of the $z^7F$ excited state of atomic chromium. Although initially this transition is orbitally forbidden in the gas phase, it becomes allowed in the octahedral site symmetry. The species marked *** are due to atomic iron transition for which the assignments are given in Table 10.

The bands located at 356 nm, 352.5 nm, and 345 nm originated from the $y^7P \leftarrow {}^7S$ transition of chromium atoms. The band separation (895 $cm^{-1}$) for this triplet is much larger than the gas phase splitting (206 $cm^{-1}$) indicating that the Jahn-Teller effect is active in the $y^7P$ excited state. Note that except for the J=3 component, the predicted and observed MCD signs are the same (see Table 10).

The $z^7P \leftarrow {}^7S$ transition exhibits a triplet with the bands centered at 415 nm, 409 nm, and 404 nm. This triplet has a much larger separation (655 $cm^{-1}$) than the known gas phase splitting (194 $cm^{-1}$). The predicted MCD signs for the J = 2, 3, and 4 components are positive, positive, and negative, respectively but the observed MCD signs are positive, negative, and negative. Again the sign reversal for the J=3 component together with a larger separation of bands compared to the gas phase splitting indicate that the $z^7P$ excited state is dynamically distorted by the matrix cage vibrations. In the following section a detailed analysis of the spectral moment for the Cr/Xe will verify this tentative conclusion.

## Spectral Moment Analysis

The ratio of the first moment of MCD to the zeroth moment of absorption for the ${}^7P \leftarrow {}^7S$ transition of chromium atom is given by

$$\frac{\langle\Delta A\rangle_1}{\langle A\rangle_0} = -\left(\frac{16\Delta}{kT} - 2g_{orb}\right)\beta H \qquad (57)$$

where the symbols $g_{orb}$, $\beta$, H, k, and T have been previously defined and the parameter $\Delta$ is connected to the spin-orbit splitting by

$$\Delta_{4,3} = 4\ \Delta \qquad (58)$$

and

$$\Delta_{3,2} = 3\ \Delta \qquad (59)$$

A plot of $\langle\Delta A\rangle_1/\langle A\rangle_0$ versus reciprocal temperature is given in Figure 42. From the slope and intercept of this plot, together with equations (58) and (59) the excited state spin-orbit splitting ($7\Delta$) and the orbital g factor ($g_{orb}$) are found to be 60.6 $cm^{-1}$ and 3.4, respectively. Cr atoms in the gas phase exhibit[66] a 194 $cm^{-1}$ splitting between the $^7P_4$ and $^7P_2$ states. Comparing this value with the 60.6 $cm^{-1}$ matrix value shows clearly that the spin-orbit splitting is reduced by a factor of 3.2 in the xenon matrix. The observed reduction is most probably the result of mixing with the matrix atomic orbitals, as noted previously for the Cu/Ar system.[19] The deviation of the experimental value of $g_{orb}$, 3.4 from the theoretical value, 1 is because the $g_{orb}$ is very sensitive to any random or systematic error in the plotted moment or the temperature values (i.e., $T^{-1} \to 0$ for a small range of temperature, 11-18 K). It is reasonable to conclude that this large increase in $g_{orb}$ is not real and merely reflects the large errors inherent in this measurement.

FIGURE 42. Experimental plot of $\langle \Delta A \rangle_1 / \langle A \rangle_0$ vs. $\frac{1}{T}$ for xenon matrix-isolated chromium atom band at 410 nm.

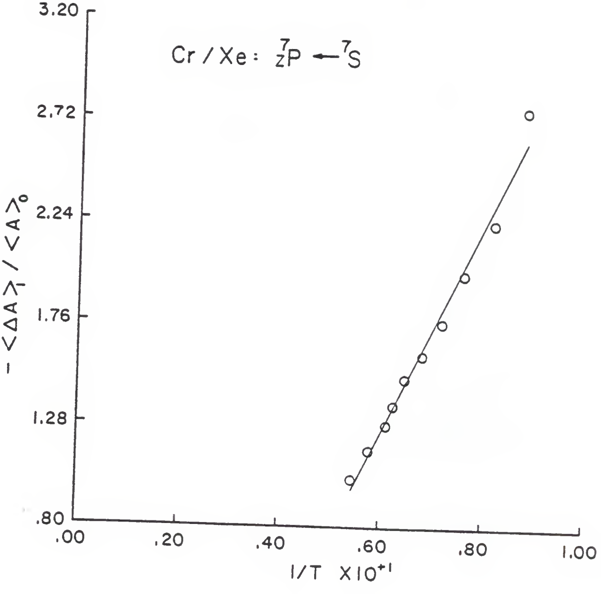
Cr / Xe : $_z^7P \leftarrow {}^7S$
3.20
2.72
2.24
1.76
1.28
.80
$-\langle \Delta A \rangle_1 / \langle A \rangle_0$
.00
.20
.40
.60
.80
1.00
1/T X10$^{+1}$

The ratio of the third moment of the MCD and the second moment of the absorption to the zeroth moment of the absorption are given, respectively, by

$$\frac{\langle \Delta A \rangle_3}{\langle A \rangle_o} = 3\, \frac{\langle \Delta A \rangle_1}{\langle A \rangle_0} \left( \langle E^2 \rangle_C + \tfrac{1}{2} \langle E^2 \rangle_{NC} + 4\Delta^2 \right) \tag{60}$$

and

$$\frac{\langle A \rangle_2}{\langle A \rangle_0} = \langle E^2 \rangle_C + \langle E^2 \rangle_{NC} + 8\Delta^2 \tag{61}$$

where $\langle E^2 \rangle_C$ and $\langle E^2 \rangle_{NC}$ stands for the contributions to the second moment of the absorption (or bandwidth) from the cubic and noncubic lattice modes, respectively.

In Figure 43 is shown the experimental plot of $\langle \Delta A \rangle_3/\langle A \rangle_0$ versus reciprocal temperature. The slope of this plot found to be -7.04 x $10^6$. Using the slope together with the equations (60) and (61). The value of $\langle E^2 \rangle_C$ and $\langle E^2 \rangle_{NC}$ can be obtained. The cubic and noncubic contributions from the lattice modes on the spectrum are determined to be 8.6 x $10^3$ $cm^{-2}$ and 7.7 x $10^4$ $cm^{-2}$, respectively. Thus, the noncubic contribution is dominant for the case of chromium in Xe matrices. This result also established, as in the Mn/Kr case, that the noncubic lattice modes responsible for the Jahn-Teller effect in the $^7P$ state are present and operative.

## Cr/Ar

In Figure 44 is shown the absorption and MCD spectra of the chromium species isolated in an argon matrix. The MCD band positions as well as band assignments are given in Table 11. The Cr/Ar MCD spectrum shows both postively- and negatively-signed bands which are given in Figure 44.

FIGURE 43. Experimental plot of $\langle \Delta A \rangle_3 / \langle A \rangle_o$ vs. $\frac{1}{T}$ for xenon matrix-isolated chromium atom band at 410 nm.

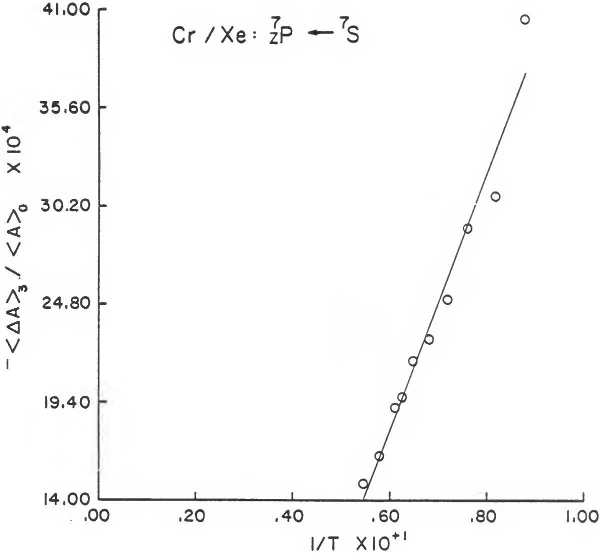
Cr / Xe: $^7_zP \leftarrow {}^7S$
41.00
35.60
30.20
24.80
19.40
14.00
$-\langle\Delta A\rangle_3 / \langle A\rangle_0 \times 10^4$
.00
.20
.40
.60
.80
1.00
$1/T \times 10^{+1}$

FIGURE 44. Absorption (top) and MCD (bottom) spectra of chromium species in an argon matrix.

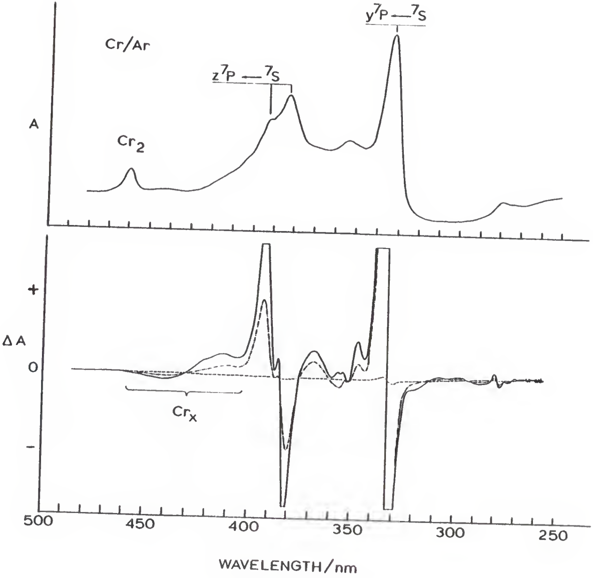
Cr/Ar
$y^7P \leftarrow {}^7S$
$z^7P \leftarrow {}^7S$
A
$Cr_2$
+
ΔA
0
–
$Cr_x$
500
450
400
350
300
250
WAVELENGTH/nm

## TABLE 11. MCD Band Positions, Matrix Shifts and Assignments for Cr Species Isolated in an Argon Matrix

| Transition | | Gaseous[a] | | Ar Matrix[b] | | | Shift | MCD signs | | Species[c] |
|---|---|---|---|---|---|---|---|---|---|---|
| | J | ν/cm$^{-1}$ | Δν/cm$^{-1}$ | λ/nm | ν/cm$^{-1}$ | Δν/cm$^{-1}$ | Δν = νAr − νgas | Predicted | Observed | |
| $^1\Sigma_u^+ \leftarrow {}^1\Sigma_g^+$ | | 21751±1* | | 460.0** | 21733 | | −18 | N | N | Cr$_2$<br>(one site) |
| ? | | | | 440.0<br>(broad)<br>423.0<br>(broad)<br>414.0<br>(broad) | 22721<br>23634<br>24148 | 913<br>514 | | | −<br>+<br>+ | Cr$_x$ |
| | 2 | 23305 | | 394.0 | 25374 | | 2069 | + | + | |
| | | | 81 | | | 392 | | | | |
| $z^7P_J^o \leftarrow a^7S$ | 3 | 23386 | | 388.0 | 25766 | | 2380 | + | − | Cr |
| | | | 113 | | | 405 | | | | |
| | 4 | 23499 | | 382.0 | 26171 | | 2872 | − | − | |
| ? | | | | 269.2<br>357.0<br>352.0<br>348.0 | 27079<br>28003<br>28401<br>28727 | | | | +<br>−<br>−<br>+ | Cr$_y$ |
| | 2 | 27729 | | 335.8 | 29771 | | 2042 | + | + | |
| | | | 91 | | | | | | | |
| $y^7P_J^o \leftarrow a^7S$ | 3 | 27820 | | -- | -- | 386<br>618 | -- | + | ? | Cr |
| | | | 115 | | | | | | | |
| | 4 | 27935 | | 331.5 | 30157 | | 2222 | − | − | |
| $y^5D \leftarrow {}^5D$ | 4 | 33096 | | 309.0 | 32353 | | −743 | + | + | *** Fe |
| $y^5D_J \leftarrow {}^5D$ | 3 | 33507 | | 297.0 | 33660 | | 153 | + | + | *** Fe |
| $y'^5F_J \leftarrow {}^5D$ | 5 | 33695 | | 289.0 | 34592 | | 897 | − | − | *** Fe |
| ? | | | | 281.5<br>279.0 | 35514<br>35832 | 316 | | +<br>(Pseudo A term)<br>− | +<br>− | Cr$_3$ |
| $y^5P_3 \leftarrow {}^5D$ | 3 | 36767 | | 271.5 | 36822 | | 55 | + | + | *** Fe |
| $y'^5P_3 \leftarrow 5$ | 3 | 36767 | | 268.5 | 37654 | | 887 | + | + | *** Fe |
| $x^5F_J \leftarrow {}^5D$ | 5 | 40257 | | 247.0 | 40474 | | 217 | − | − | *** Fe |
| $x'^5F_J \leftarrow {}^5D$ | 5 | 40257 | | 240.5 | 41587 | | 1310 | − | − | *** Fe |

[a] wavenumber marked *, taken from reference 96.
[b] wavelengths marked **, taken from the absorption spectrum.
[c] species marked ***, are Fe atoms which appear in the matrix due to impurity of Cr sample (see text).
N = no MCD signal.

One absorption band at 460 nm has no MCD signal and is assigned to $Cr_2$ band. The three MCD bands (broad) located at 440 nm, 423 nm, and 414 nm do not correlate with any atomic transition in the gas phase. These bands exhibit a temperature dependent $C_0$ term which must arise from a degenerate ground ground state of a $Cr_x$ molecule. At the present the value of x cannot be specified.

The bands located at 394 nm, 388 nm, and 382 nm are due to the $z^7P \leftarrow a^7S$ transition. The separation of these bands (797 $cm^{-1}$) is much larger than the spin-orbit splitting of 194 $cm^{-1}$ in the gas phase. The signs of the MCD bands follow the same trend as in Cr/Kr and Cr/Xe.

Four bands at 369.2 nm, 357 nm, 352 nm, and 348 nm have positive, negative, negative, and positive MCD signs. These bands seem to be temperature dependent, however, upon warming the matrix the band located at 357 nm is changed in sign. Since there is not any correlation with the gas phase and since these apparently are not the same species as $Cr_x$, they are assigned to a $Cr_y$ species with the value of y unspecified.

The bands at 335.8 nm and 331.5 nm arise from the $y^7P \leftarrow {}^7S$ transition. Although the middle component is not resolved in our matrix, the predicted and observed MCD signs are in good agreement (see Table 11). The separation of these bands (386 $cm^{-1}$) compared to the gas phase splitting (206 $cm^{-1}$) is larger by a factor of about 2.

The species are marked *** belong to iron transitions which originated from the iron impurity in the chromium sample. The two positively- and negatively-signed MCD bands located at

281.5 nm and 279 nm, respectively, with a separation of 318 $cm^{-1}$ are due to the $Cr_3$ transition. The maximum position of the absorption band matches with the zero crossing of the MCD bands indicating a pseudo-A term.

# CHAPTER VIII

# CONCLUDING REMARKS

The results of this study have demonstrated that the matrix isolation MCD technique can provide valuable information on the excited states of high temperature atoms and small clusters. The MCD of matrix-isolated Fe, Mn and Cr species (i.e., atoms, dimers, etc.) has confirmed or established the assignment of numerous electronic transitions. The application of band moment calculations to the MCD and absorption spectra has made possible the extraction of important information such as excited state spin-orbit splitting and lattice mode contributions to the bandwidths.

The initial effort in which the matrix isolation technique was combined with magnetic circular dichroism spectroscopy was undertaken ten years ago. Since the combined technique is relatively young and since only comparatively few species have been studied so far, the future of this technique should be very productive, informative and bright. This technique can be extended to other high temperature atoms and molecules to identify the symmetry of excited states and to determine their magnetic moments.

From the present work certain improvements and extensions to the current apparatus and systems under study appear desirable. A major uncertainty in the calculations of moments is due to the uncertainties in the baseline of the absorption spectra. In absorption experiments, the use of two mirrors in the reference beam causes a frequency dependent reflectivity loss which results in a drift of the spectral baseline in the ultraviolet region. To reduce this error, it is suggested that front-surface mirrors be employed in both sample and reference beams. This approach will balance the reflectivity losses in both beams and will keep the linearity of the baseline constant.

For a better characterization of the MCD of matrix-isolated species, several modifications can be performed on the present apparatus. The relatively low magnetic field (0.55 T) employed in the present research was sufficient to obtain excellent MCD data. However, due to the small diameter and long axial holes in the magnet poles, it was not possible to study magnetic circularly polarized emission. Very recently, our laboratory has acquired a compact-design split-coil, superconducting magnet (4.0 T) constructed by Oxford Instruments. Using the superconducting magnet, it would be very interesting to study other magneto-optical methods such as magnetic linear dichroism (MLD), magnetic circularly polarized emission, and magnetic linearly polarized emission. Their use has not yet become widespread. It would also be desirable to study matrix-isolated neon matrices at 4.2 K. Manganese spectra in neon matrices would help to better distinguish between matrix site effects and the existence of other cluster species in the matrix.

With the present apparatus, it is not possible to measure the deposition rate of the sample accurately. Since the sample thickness depends on the oscillator strength of the optical transition (i.e., the forbidden visible transitions require higher concentration of sample in the matrix) it would be very important to know the exact concentration of the matrix-isolated sample. This approach can be achieved by employing a quartz crystal microbalance. It would also by very interesting to modify the apparatus and insert a quadrupole mass spectrometer between the furnace assembly and the sample window to selectively deposit a particular species on the cold window and study its MCD spectroscopy.

It would be both theoretically and experimentally interesting to study the MCD of matrix-isolated transition metal hydrides. The theoretical interest of these hydrides arises because they are the simplest species that can be studied for a better understanding of the nature and energetics of sigma bonding in transition metal compounds.[98-100] The experimental interest in these species is their existence in the stellar atmosphere,[15,100] their importance as reactive intermediates in homogeneous and heterogeneous catalysis,[101,102] their use in hydrogen storage systems,[103] and their involvement in the interconversion of $H_2$, $O_2$ and $H_2O$.[104] It would also be interesting to investigate the MCD of the heteronuclear species of transition metals. A furnace assembly consisting of two Knudsen cells is currently under construction for this purpose.

## REFERENCES

1. J. R. Blackborow and D. Young, Metal Vapor Synthesis in Organometallic Chemistry, Springer-Verlag, Berlin, 1979.

2. W. J. Power and G. A. Ozin in Advanced Inorganic Chemistry and Radiochemistry, Vol. 23, H. J. Emeleus and A. G. Sharpe (eds), Academic Press, New York, 1980.

3. M. Moskovitz and G. A. Ozin, (eds.), Cryochemistry, Wiley-Interscience, New York, 1976.

4. K. Klabunde, Chemistry of Free Atoms and Radicals, Academic Press, New York, 1980.

5. E. Drauglis and R. I. Jaffee, (eds.), The Physical Basis of Heterogeneous Catalysis, Plenum Press, New York, 1975.

6. F. F. Abraham, Homogeneous Nucleation Theory, Academic Press, New York, 1975.

7. R. Ugo, Catal. Rev., 11, 225 (1975).

8. J. F. Hamilton and P. C. Logel, Photo. Sci. Eng.,

9. B. Wellegehausen, IEEE J. Quan. Elec., QEIS, 1108 (1979).

10. J. B. Joffend, R. W. Field, D. R. Guyer and S. Leone, in Laser Spectroscopy III, J. L. Hall and J. L. Carlsten, (eds.), Springer-Verlag, Berlin, 1977.

11. G. N. Lewis, D. Lipkin and T. T. Magel, J. Amer. Chem. Soc., 63, 3005 (1941).

12. I. Norman and G. Porter, Nature, London, 174, 508 (1954).

13. E. Whittle, D. A. Dows and G. C. Pimentel, J. Chem. Phys., 22, 1943 (1954).

14. M. J. Linevsky, J. Chem. Phys., 34, 587 (1961).

15. W. Weltner, Jr., Ber. Bunsenges. Phys. Chem., 82, 80 (1978).

16. B. Meyer, Low Temperature Spectroscopy, Elsevier, New York, 1971.

17. D. M. Gruen, in Cryochemistry, M. Moskovitz and G. A. Ozin, (eds.), Wiley-Interscience, New York, 1976, p. 441.

18. D. M. Kolb and F. Forstmann, in Matrix Isolation Spectroscopy, A. J. Barnes et al., (eds.), Reidel, Dordrecht, 1981, p. 347.

19. K. J. Zeringue, J. Shakhsemampour, J. C. Rivoal, and M. Vala, J. Chem. Phys., 78, 2231 (1982).

20. R. L. Mowery, J. C. Miller, P. N. Schatz, E. R. Krauss, S. M. Jacobs and L. Andrews, J. Chem. Phys., 70, 3920 (1979).

21. A. D. Buckingham and P. J. Stephens, Ann. Rev. Phys. Chem., 17, 399 (1966).

22. I. N. Douglas, R. Grinter, and A. J. Thomson, Dalton Division Symposium, Chemical Society, Autumn Meeting, University of East Anglia, 1973.

23. J. A. Spencer, J. Chem. Phys., 54, 5139 (1971).

24. G. Barth, R. Records, E. Bunnenberg, C. Djerassi and W. Voelter, J. Am. Chem. Soc., 25, 57 (1971).

25. G. Barth, W. Voelter, E. Bunnenberg and C. Djerassi, J. Am. Chem. Soc., 94, 1293 (1972).

26. J. LoMenzo, B. D. Bird, G. A. Osborne and P. J. Stephens, Chem. Phys. Lett., 9, 332 (1971).

27. M. J. Harding and B. Briat, Mol. Phys., 25, 745 (1973).

28. P. J. Stephens, Ann. Rev. Phys. Chem., 251, 201 (1974).

29. P. N. Schatz and A. J. McCaffery, Quart. Rev. Chem. Soc., 23, 552 (1969).

30. I. N. Douglas, R. Grinter and A. J. Thomson, Mol. Phys., 28, 1377 (1974).

31. M. Kreglewski and M. Vala, Chem. Phys., 56, 381 (1981).

32. K. Zeringue, J. Shakhsemampour, and M. Vala, in Metal Bonding and Interactions in High Temperature Systems with Emphasis on Alkali Metals, ACS Symposium Series No. 179, J. L. Gole and W. C. Stwalley (eds.), American Chem. Soc., Washington, D.C., 1982, Chap. 15.

33. K. J. Zeringue, Ph.D. Dissertation, University of Florida, 1983.

34. E. R. Krausz, R. L. Mowery and P. N. Schatz, Ber. Bunsenses Phys. Chem., 82, 134 (1978).

35. I. N. Douglas, R. Grinter and A. J. Thomson, Chem. Phys. Lett., 28, 192 (1974).

36. M. A. Goetschlackx, R. L. Mowery, E. R. Krausz, W. C. Yeakel, P. N. Schatz, B. S. Ault and L. Andrews, Chem. Phys. Lett., 47, 23 (1977).

37. D. H. Powell, Ph.D. Dissertation, University of Florida, 1979.

38. R. D. Brittain, Ph.D. Dissertation, University of Florida, 1979.

39. T. J. Barton, R. Grinter, and A. J. Thomson, Chem. Phys. Lett., 40, 399 (1976).

40. T. J. Barton, I. N. Douglas, R. Grinter, and A. J. Thomson, Mol. Phys., 30, 1677 (1975).

41. G. A. Osborne, J. Mol. Spec., 49, 48 (1974).

42. J. C. Rivoal, J. Shakhsemampour, K. J. Zeringue, and M. Vala, Chem. Phys. Lett., 92, 313 (1982).

43. J. Shakhsemampour, R. Pyzalski, M. Vala, and J. C. Riovoal, (to be published).

44. P. J. Stephens, Ph.D. Dissertation, Oxford University, 1964.

45. P. J. Stephens, J. Chem. Phys., 52, 3489 (1970).

46. P. J. Stephens, in Advances in Chemical Physics, Volume 35, I. Prigogine and S. A. Rice, (eds.), Wiley, New York, 1976, p. 197.

47. A. S. Davydov, Quantum Mechanics, Addison-Wesley, Reading, Massachusetts, 1961, p. 302.

48. C. H. Henry, S. E. Schnatterly, and C. P. Slichter, Phys. Rev., A137, 583 (1965).

49. G. A. Osborne and P. J. Stephens, J. Chem. Phys., 56, 609 (1972).

50. R. J. Tucon, Ph.D. Dissertation, Oxford University, 1977.

51. J. A. Broomhead, F. P. Dwyer and J. W. Hogarth, Inorg. Syn., 6, 186 (1960).

52. A. J. McCaffery and S. F. Mason, Mol. Phys., 6, 359 (1963).

53. S. A. Mitchell, J. Farrell, G. A. Kinney-Wallace and G. A. Ozin, J. Am. Chem. Soc., 102, 7702 (1980).

54. A. A. Belyaeva, Y. B. Predtechenskii and L. D. Shcherba, Opt. Spec. (Eng.), 34, 21 (1973).

55. J. H. Ammeter and D. C. Schlosnagle, J. Chem. Phys., 59, 4784 (1973).

56. W. E. Billups, J. L. Margrave and R. H. Hange, J. Am. Chem. Soc., 12, 7393 (1980).

57. P. H. Barrett, M. Pasternak and R. G. Pearson, J. Am. Chem. Soc., 101, 222 (1979).

58. G. A. Ozin and J. G. McCaffery, J. Am. Chem. Soc., 14, 7352 (1982).

59. W. Keune and E. Lüescher, Solid State Comm., 8, 811 (1970).

60. D. M. Mann and H. P. Broida, J. Chem. Phys., 55, 84 (1971).

61. H. Micklitz and P. H. Barrett, Phys. Rev., B4, 3845 (1971).

62. J. S. Shirk and A. M. Barr, J. Chem. Phys., 49, 5156 (1968).

63. D. H. W. Carstens, J. F. Kozlowski and D. M. Gruen, Hi. Temp. Sci., 4, 301 (1972).

64. M. T. McKenzie, M. A. Epting and E. R. Nixon, J. Chem. Phys., 77, 735 (1982).

65. M. Poliakoff and J. J. Turner, J. Chem. Soc., Faraday Trans. 2, 70, 93 (1974).

66. C. E. Moore, Atomic Energy Levels, Natl. Bur. Stand. Circular, 467, Vol. 2 (1952).

67. D. H. Carstens, W. Brashear, D. R. Eslinger and D. M. Gruen, Appl. Spectrosc., 26, 184 (1972).

68. T. K. McNab, H. Micklitz and P. H. Barrett, Phys. Rev., B4, 3787 (1971).

69. P. H. Barrett and T. K. McNab, Phys. Rev. Lett., 25, 1601 (1970).

70. M. T. McKenzie and E. R. Nixon, Chem. Phys., 75, 115 (1983).

71. J. H. Van Vleck, Dis. Faraday Soc., 26, 96 (1958).

72. E. V. Condon and G. H. Shortley, The Theory of Atomic Spectra, Cambridge University Press, Cambridge, 1957, Table 19, pp. 241-243.

73. K. Tuzimura, T. Konno, H. Meguro, M. Hatano, T. Murakami, K. Kachiwara, K. Saito, Y. Kondo and T. Suzuki, Anal. Biochem., 81, 167 (1977).

74. T. C. Devore, A. Eqing, H. F. Franzen and V. Calder, Chem. Phys. Letters, 35, 78 (1975).

75. M. Moskovitz and D. P. DiLella, J. Chem. Phys., 73, 4917 (1980).

76. M. Moskovits, Accounts Chem. Res., 12, 229 (1979).

77. O. Schnepp, J. Phys. Chem. Solids, 17, 188 (1961).

78. E. L. Lee and R. G. Gutmacher, Phys. Chem. Solids, 23, 1823 (1962).

79. W. E. Klotzbücher and G. A. Ozin, Inorg. Chem., 19, 3376 (1980).

80. A. Kant, S. S. Lin and B. Strauss, J. Chem. Phys., 49, 2765 (1965).

81. M. Brith and O. Schnepp, J. Chem. Phys., 39, 2714 (1963).

82. D. M. Gruen, S. L. Gandioso, R. L. McBeth, and J. L. Lerner, J. Chem. Phys., 60, 89 (1974).

83. D. W. Breen and D. M. Gruen, J. Chem. Phys., 60, 1797 (1974).

84. C. A. Baumann, R. J. Van Zee, S. V. Bhat and W. Weltner Jr., J. Chem. Phys., 78, 190 (1983).

85. R. K. Nesbet, Phys. Rev., A135, 460 (1964).

86. A. Kant, S. S. Lin and B. Strauss, J. Chem. Phys., 49, 1983 (1968).

87. W. F. Cooper, G. A. Clarke and C. R. Hare, J. Phys. Chem., 76, 2268 (1972).

88. J. Harris and R. O. Jones, J. Chem. Phys., 70, 830 (1979).

89. M. M. Goodgame and W. A. Goddard III, Phys. Rev. Letters, 48, 135 (1982).

90. R. J. Van Zee, C. A. Baumann and W. Weltner Jr., J. Chem. Phys., 74, 6977 (1981).

91. J. C. Rivoal and B. Briat, Mol. Phys., 27, 1081 (1974).

92. L. Landan and E. Lifshitz, Quantum Mechanics, 2nd Ed., Pergamon, Oxford, Ch. 11 (1967).

93. P. W. Anderson, Solid State Phys., 14, 99 (1963).

94. D. M. Gruen in Cryochemistry, (eds.) M. Moskovits and G. A. Ozin, Wiley-Interscience, New York (1976).

95. E. P. Kündig, M. Moskovits, G. A. Ozin, Nature, 254, 503 (1975).

96. D. L. Michalopoulos, M. E. Gensic, S. G. Hansen, D. E. Powers and R. E. Smalley, J. Phys. Chem., 86, 3914 (1982).

97. D. P. DiLella, W. Limm, R. H. Kipson, M. Moskovits, and K. V. Taylor, J. Chem. Phys., 77, 5263 (1982).

98. P. S. Bagus and H. F. Schaefer III, J. Chem. Phys., 58, 1844 (1973).

99. J. Demuynck and H. F. Schaefer III, J. Chem. Phys., 72, 311 (1980).

100. P. H. Scott and W. G. Richard, Mol. Spec., 4, 70 (1976).

101. B. R. James, Homogeneous Hydrogenation, Wiley-Interscience, New York, 1973.

102. H. F. Schaefer III, Accounts Chem. Res., 10, 287 (1977).

103. F. R. Kalhammer and T. R. Schneider, Ann. Rev. Energy, 1, 311 (1976).

104. T. Yoshida, T. Okana and S. Otsuka, J. Am. Chem. Soc., 102 5966 (1980).

## BIOGRAPHICAL SKETCH

Jalal Shakhsemampour was born in Torbate Haydarieh, Iran, on April 22, 1949. He graduated from Alavi High School, Mashhad, Iran, in 1968, and attended Mashhad University, Mashhad, Iran, until 1972, when he was awarded the degree of Bachelor of Science in chemistry. In 1973, he entered the graduate school at the University of Tehran, Tehran, Iran, and received the degree of Master of Science in chemistry in 1975. He taught chemistry at Abourayhan University, Tehran, Iran, from 1975 to 1977. In 1977, he was awarded a scholarship by Abourayhan University to pursue his Ph.D. studies. Since September, 1978, he has pursued a course of study leading to the Doctor of Philosophy degree in chemistry at the University of Florida, Gainesville, Florida. He has two daughters, Rahelah, 7, and Rabeah, 6.

I certify that I have read this study and that in my opinion it conforms to acceptable standards of scholarly presentation and is fully adequate, in scope and quality, as a dissertation for the degree of Doctor of Philosophy.

Martin Vala

Martin T. Vala, Chairman
Professor of Chemistry

I certify that I have read this study and that in my opinion it conforms to acceptable standards of scholarly presentation and is fully adequate, in scope and quality, as a dissertation for the degree of Doctor of Philosophy.

Robert J. Hanrahan

Robert J. Hanrahan
Professor of Chemistry

I certify that I have read this study and that in my opinion it conforms to acceptable standards of scholarly presentation and is fully adequate, in scope and quality, as a dissertation for the degree of Doctor of Philosophy.

Willis B. Person

Willis B. Person
Professor of Chemistry

I certify that I have read this study and that in my opinion it conforms to acceptable standards of scholarly presentation and is fully adequate, in scope and quality, as a dissertation for the degree of Doctor of Philosophy.

Cemal Kemal

Cemal Kemal
Assistant Professor of Chemistry

I certify that I have read this study and that in my opinion it conforms to acceptable standards of scholarly presentation and is fully adequate, in scope and quality, as a dissertation for the degree of Doctor of Philosophy.

Gary G Ihas

Gary G. Ihas
Associate Professor of Physics

This dissertation was submitted to the Graduate Faculty of the Department of Chemistry in the College of Liberal Arts and Sciences and to the Graduate Council, and was accepted as partial fulfillment of the requirements for the degree of Doctor of Philosophy.

December, 1983

Dean for Graduate Studies
and Research